Reproducing Kernel Particle Method for Solving Partial Differential Equations

Jiun-Shyan Chen[1], Wing Kam Liu[2], Michael C. Hillman[3], Sheng-Wei Chi[4], Yanping Lian[2] and Miguel A. Bessa[2]

[1]*Department of Structural Engineering, University of California, San Diego, CA, USA*
[2]*Department of Mechanical Engineering, Northwestern University, Evanston, IL, USA*
[3]*Department of Civil and Environmental Engineering, Pennsylvania State University, State College, PA, USA*
[4]*Department of Civil and Materials Engineering, University of Illinois, Chicago, IL, USA*

1 INTRODUCTION

This chapter gives a state-of-the-art review of the reproducing kernel particle method (RKPM), one of the popularly used meshfree methods for solving partial differential equations (PDEs), and examples of its applications to mechanics problems are also presented. The earliest and simplest approximation method introduced in a meshfree framework is the kernel estimate (KE) employed in Lucy (1977) and Gingold and Monaghan (1977) in smoothed particle hydrodynamics (SPH); see Randles and Libersky (2000) for an overview. In the KE, if the kernel function is normalized, it assures zeroth-order completeness. The use of the symmetric kernel function further meets first-order consistency. However, the discretization of the KE assures neither zeroth- nor first-order consistency in a finite domain, unless the lumped mass (or lumped volume) is carefully selected, which is difficult to accomplish with irregular boundary shapes and in arbitrary particle distributions.

The reproducing kernel (RK) approximation was first proposed by Liu *et al.* (1995a,b) to improve the accuracy of the SPH method for finite domain problems. The employment of the RK approximation for the numerical solution of PDEs using the Galerkin method is called the RKPM (Liu *et al.,* 1995a,b). In this method, the kernel function is modified by introducing a correction function to meet polynomial reproducing conditions. The resulting modified kernel function exactly reproduces polynomials to a specific order and thereby fulfills completeness. The shape functions constructed from this method can be made equivalent to the moving least-squares kernel interpolants if polynomial basis functions are employed. In general, the RK approximation can be constructed using scattered points without mesh connectivity. For comparison, as shown in Figure 1, the approximation function for point I in the finite element method (FEM) is constructed at the element-level

Encyclopedia of Computational Mechanics Second Edition,
Edited by Erwin Stein, René de Borst and Thomas J.R. Hughes.

DOI: 10.1002/9781119176817.ecm2104

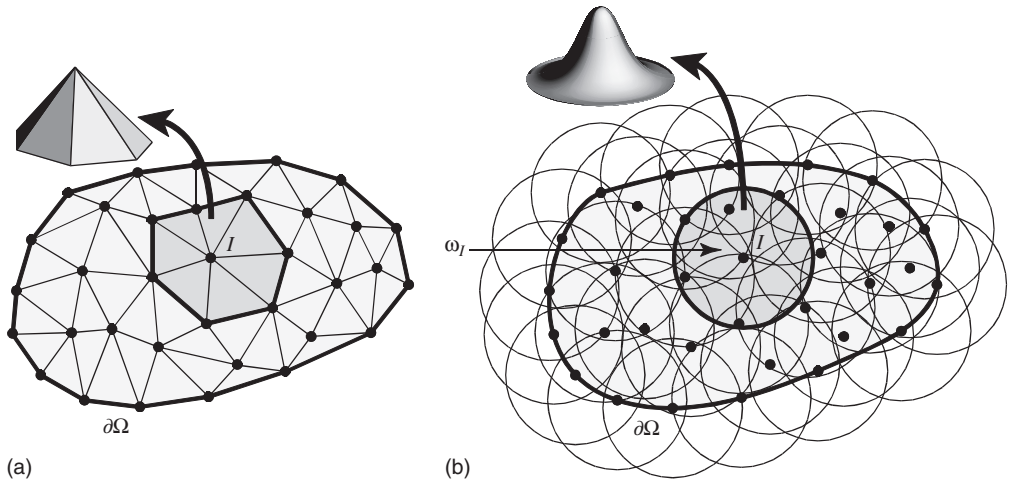

Figure 1. (a) The patching of finite element shape functions from local element domains and (b) meshfree approximation function constructed directly at the nodes in the global coordinates. (Reproduced with permission from Chen and Belytschko (2015). © Springer, 2015.)

natural coordinates and then transformed to global Cartesian coordinates, whereas the RK approximation functions are constructed using only nodal coordinate data in the global Cartesian coordinates directly. These compactly supported RK approximation functions form a partition of unity subordinate to the open covering of the domain, with controllable orders of continuity and completeness. Under this construction, it becomes possible to relax the strong tie between the quality of the discretization and the quality of approximation in the FEM, and it significantly simplifies the procedures in *h*-adaptivity. Special basis functions can be embedded in the RK approximation to capture essential characteristics of the physical problems to be solved, for example, crack-tip asymptotic functions for fracture problems. RKPM has also been shown to be particularly effective for solving large deformation problems without the burden of dealing with mesh distortion or entanglement in the conventional FEM. An overview of the RK approximation and its mathematical properties for solving PDEs is given in Section 2.

Section 3 unifies Peridynamics with other meshfree methods by demonstrating that the former is a particular case of the RK approximation. Additional considerations and implications are given in that section. Section 4 discusses the application of meshfree methods to solving fractional PDEs. A one-dimensional fractional advection–diffusion equation (FADE) using the RK approximation in the Petrov–Galerkin form is studied to show its performance as well as the effectiveness of the selection of appropriate viscosity coefficient.

One of the unique properties of the RK approximation is its similarity to wavelets, which leads to the ability to employ multiresolution analysis by wavelet-RK methods and multiple-scale RKPM (Liu and Oberste-Brandenburg, 1993; Liu and Chen, 1995; Liu *et al.,* 1997b). As is well known, the interpolation functions serve as low-pass filters. A sequence of low-pass filters can be obtained by changing the value of the dilation parameter, usually by a factor of two. Through the projection of the sequence of low-pass filters, a hierarchical representation of a given response can be derived. A high-pass filter can be designed as the complementary projector to fill the resolution gap between two consecutive low-pass filters. This new set of high-pass filters is the backbone of the multiresolution analysis in the convolution formulation, and provides a non-redundant representation of the given function (Liu *et al.*, 1996b). After Liu and Oberste-Brandenburg (1993) first proposed the concept of the multiple-scale RKPM, Liu and coworkers (Liu and Chen, 1995; Liu *et al.*, 1996a,b, 1997a,b) have extensively studied multiresolution analysis by wavelet and RK methods, including edge detection, aliasing control, adaptive refinement, frequency and wave number shifting techniques – which can be utilized to perform multiple-scale analysis of various problems with large deformation, high gradients, and high modal density, such as structural acoustics (Liu *et al.,* 1996a,b, 1997a), structural dynamics (Liu *et al.,* 1996a,b; Lu *et al.,* 2005), elastic–plastic deformation (Liu *et al.*, 1996a, 1997a), computational fluid dynamics (Liu *et al.*, 1996a,b, 2007b), hyperelasticity (Liu *et al.*, 1996a,b), and shock waves (Roth *et al.*, 2016). Section 5 provides the basic equations of multiresolution analysis, the multiple-scale wavelet particle method, and the multiple-scale RK approximation, as well as a discussion of

the application of *hp*-like adaptivity in RKPM. It should be noted that the *hp*-like adaptive refinement can be performed trivially without prior knowledge of the exact solution since it is easy to construct a local error indicator similar to local aliasing estimations, which is a detrimental consequence of undersampling on particle distribution.

RKPM is a meshfree method for solving PDEs based on the Galerkin framework. A crucial consideration for Galerkin-based meshfree methods using RK or moving least-squares (MLS) approximations is the choice of the quadrature employed for domain integration. Although RK and MLS approximation functions are capable of reproducing monomials of arbitrary order in arbitrary discretizations, *this completeness property does not guarantee optimal rates of convergence in the Galerkin solution of PDEs if the domain integration is not sufficiently accurate*. Unfortunately, RK and MLS approximation functions are rational, and the compact supports form overlapping support structures that are difficult to integrate accurately (Dolbow and Belytschko, 1999). The result of these two difficulties is that the accuracy and convergence of numerical solutions are sensitive to the choice of domain integration. Gaussian quadrature was commonly used in the early development of meshfree methods (cf. Liu *et al.*, 1995a; Belytschko *et al.*, 1994, 1996; Chen *et al.*, 1996). However, if Gaussian integration (GI) is employed, high-order quadrature is necessary to obtain optimal convergence (Dolbow and Belytschko, 1999; Chen *et al.*, 2001; Babuška *et al.*, 2008; Chen *et al.*, 2013). A general framework that offers a paradigm for formulating quadrature rules and test functions to achieve optimal convergence for a given PDE at hand has been established (Chen *et al.*, 2001, 2013; Krongauz and Belytschko, 1997; Bonet and Kulasegaram, 2000). These conditions have been referred to as the *integration constraints* (Chen *et al.,* 2001) for first-order Galerkin exactness, and the *variational consistency conditions* (Chen *et al.*, 2013) in their recent generalization to higher order Galerkin exactness. Satisfaction of these conditions has also been shown to restore Galerkin orthogonality for solutions of order n (Rüter *et al*., 2013), and methods that satisfy these conditions are grounded in variational principles (Sze *et al*., 2004). These variational consistency conditions can also be utilized to restore convergence rates associated with the completeness of the approximation space while using low-order quadrature (Chen *et al.,* 2001, 2013; Hillman and Chen, 2016). Mathematical analysis of meshfree methods with quadrature has been carried out (Babuška *et al.,* 2008, 2009), and a related condition that the rows of the system matrix sum up to zero was shown to be necessary for well-behaved solutions with quadrature, called the *zero row-sum condition*, and this can be achieved by modifying the diagonal entries of the system matrix.

Nodal integration methods are often employed in Galerkin meshfree methods as an alternative to GI for various reasons – preservation of the mesh-free characteristics of the method on the quadrature level, simplicity, and efficiency. These methods however, generally exhibit poor solution accuracy and convergence rates (Chen *et al.*, 2001, 2013; Beissel and Belytschko, 1996), and further, instability arises in this method owing to the possibility of sampling zero gradients at nodal points for modes with wavelength of two times the nodal spacing (Chen *et al.*, 2001; Beissel and Belytschko, 1996; Belytschko *et al.*, 2000). Many methods are available that circumvent this issue by avoiding this undersampling of the strain energy density. This can be accomplished by employing residual-based methods (Bonet and Kulasegaram, 2000; Beissel and Belytschko, 1996; Fries and Belytschko, 2008), stress points (Randles and Libersky, 2000; Dyka *et al.*, 1997; Rabczuk *et al.*, 2004), Taylor expansions (Hillman and Chen, 2016; Liu *et al.*, 1985, 2007; Nagashima, 1999), or strain smoothing in conjunction with the divergence operation of the averaged integral (Chen *et al.*, 2001, 2002; Wang and Chen, 2004, 2008; Chen and Wang, 2006). Two key issues with these methods are the associated cost involved, and the presence of any "tunable" parameters. It is worth mentioning that the strain smoothing method avoids both, but needs additional stabilization to ensure reliable solutions in all situations (Puso *et al.*, 2008). Section 6 includes an overview of the recent developments in addressing domain integration in meshfree methods.

Alternatively, strong form collocation methods have been proposed for solving PDEs (Hardy, 1990), such as the radial basis collocation method (RBCM) (Kansa, 1990a,b; Hu and Li, 2006; Hu *et al.*, 2007), the finite point method (Oñate *et al.*, 1996), and the reproducing kernel collocation method (RKCM) (Aluru, 2000; Chen *et al.*, 2008; Hu *et al.,* 2009, 2011). From a convergence standpoint, the compactly supported RK approximations with monomial reproducibility render an algebraic convergence in RKCM, while the nonlocal RBFs with certain regularity offer exponential convergence in RBCM. Nevertheless, the linear system of RBCM is typically more ill-conditioned compared to those based on compactly supported approximations. The work in (Chen *et al.*, 2008) shows that one can construct a localized RBF using a partition of unity function, such as the RK enhanced radial basis function, to yield a local approximation while achieving the exponential convergence in RBCM. This localized RBF, combined with the subdomain collocation method, has been applied to problems with local features, such as problems with heterogeneity or cracks that are difficult to solve using RBCM (Chen *et al.*, 2009; Wang *et al.*, 2010). Strong form collocation methods such as RKCM, however, come with

increased computational complexity owing to taking of higher order derivatives of the approximation functions and the need for using a large number of collocation points for optimal convergence. A gradient reproducing kernel collocation method (G-RKCM) (Chi *et al.*, 2013) has been proposed to address the computational complexity in RKCM while achieving optimal convergence by introducing a gradient RK approximation. G-RKCM reduces the order of differentiation to first order for solving second-order PDEs with strong form collocation. Section 7 gives an overview of the above-mentioned strong form collocation methods.

Since RK approximation functions are constructed entirely based on a set of discrete points, RKPM has been successfully applied to model extremely large deformation problems without mesh distortion or mesh entanglement difficulties. The Lagrangian RKPM formulation (Chen *et al.*, 1996), in which the kernel functions maintain the same coverage of neighboring particles, has been introduced to model elastomeric materials and metal forming (Chen *et al.*, 1997, 1998; Wu *et al.*, 2001), among other application problems. For large deformation problems involving severe material damage and separation, the deformation gradient is no longer positive definite at all material points and neither the total Lagrangian nor the updated Lagrangian formulation is applicable. For such cases, a semi-Lagrangian RKPM formulation (Guan *et al.*, 2009, 2011) has been proposed, in which the discrete points are attached to the material points (and thus Lagrangian) while the supports of kernel functions do not necessarily deform with the materials (and thus semi-Lagrangian). In semi-Lagrangian RKPM (discussed in Section 8), the neighbor points are redefined during the deformation process to account for large flow of material motion and formation of free surfaces, and the approximation is constructed at the current configuration. The stability conditions of this approach for explicit time integration have also been studied (Guan *et al.*, 2011). A kernel contact (KC) algorithm (Chi *et al.*, 2015) has been developed under a semi-Lagrangian RKPM framework for multibody contact, and the approach has been applied to modeling fragment-impact and penetration processes (Chi *et al.*, 2015; Sherburn *et al.*, 2015) as presented in Section 8.

2 REPRODUCING KERNEL APPROXIMATION

The foundation of RKPM is the RK approximation. The RK approximation functions are constructed so that they can represent polynomial functions exactly. In this section, we first introduce the continuous form of the RK approximation to illustrate how polynomial functions can be reproduced under a convolution integral. The concept is then extended to the construction of the discrete RK approximation and finally the Galerkin approximation for solving PDEs using the RK approximation.

2.1 The continuous reproducing kernel approximation

The RK approximation can be viewed as an enhancement of the KE in SPH (Lucy, 1977; Gingold and Monaghan, 1977; Monaghan, 1982). In one-dimension, the KE of a function $u(x)$, denoted as $u^k(x)$, is expressed as the convolution between the function $u(x)$ and a kernel function in domain Ω as:

$$u^k(x) = \int_\Omega \phi_a(x-s)u(s)\mathrm{d}s \tag{1}$$

where $\phi_a(x-s)$ is called the kernel function with support size a, which plays a similar role as the weight function in the moving least-squares approximation. For example, a cubic B-spline kernel function as shown in Figure 2 is

$$\begin{aligned}\phi_a(x-s) &=: \phi_a(z)\\ &= \begin{cases} \dfrac{2}{3} - 4z^2 + 4z^3 & \text{for } 0 \le z \le \dfrac{1}{2}\\ \dfrac{4}{3} - 4z + 4z^2 - \dfrac{4}{3}z^3 & \text{for } \dfrac{1}{2} \le z \le 1\\ 0 & \text{for } z > 1 \end{cases}, \quad z = \frac{|x-s|}{a}\end{aligned} \tag{2}$$

Note that $u^k(x)$ approaches $u(x)$ if $\phi_a(x-s)$ approaches $\delta(x-s)$ and the domain is infinite. The error in (2) is due to the finite domain Ω and a kernel $\phi_a(x-s) \neq \delta(x-s)$. Consider the Taylor expansion of $u(s)$ in (1)

$$u(s) = \sum_{i=0}^{\infty} \frac{(s-x)^i}{i!} u^{(i)}(x) \tag{3}$$

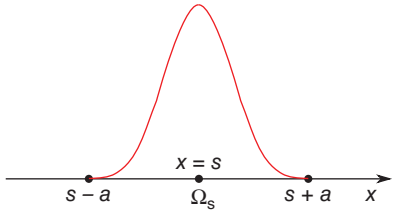

Figure 2. Kernel function $\phi_a(x-s)$. (Reproduced from Chen (2015). © Chen, 2015.)

where $u^{(i)}(x) = \mathrm{d}^i u(x)/\mathrm{d}x^i$. Here we have assumed that u is infinitely differentiable. Substituting (3) into (2), we have

$$u^k(x) = m_0(x)u(x) + \sum_{i=1}^{\infty} \frac{(-1)^i}{i!} m_i(x) u^{(i)}(x) \tag{4}$$

where $m_i(x)$ is the i-th moment of ϕ_a defined by

$$m_i(x) = \int_\Omega (x-s)^i \phi_a(x-s)\mathrm{d}s \tag{5}$$

For $u^k(x) = u(x)$, one needs $m_0(x) = 1$ and $m_i(x) = 0$ for $1 \le i$, and the only kernel function that meets these requirements is $\phi_a(x-s) = \delta(x-s)$. For nth-pleteness in $u^k(x)$, the kernel function has to satisfy the following conditions:

$$\begin{aligned} &m_0(x) = 1, \\ &m_i(x) = 0, \quad \text{for} \;\; 1 \le i \le n \end{aligned} \tag{6}$$

The equations in (6) are called the reproducing conditions. Not all kernel functions satisfy the above reproducing conditions, but a kernel function can be modified to meet them. The RK approximation, denoted as $u^R(x)$, introduces correction to the KE as follows (Liu *et al.,* 1995a,b):

$$u^R(x) = \int_\Omega \overline{\phi}_a(x; x-s) u(s)\mathrm{d}s, \tag{7}$$

where $\overline{\phi}_a(x; x-s)$ is a modified kernel function (or the RK function) given by

$$\overline{\phi}_a(x; x-s) = C(x; x-s)\phi_a(x-s), \tag{8}$$

where $C(x; x-s)$ is called the correction function, expressed as

$$C(x; x-s) = \sum_{i=0}^{n} (x-s)^i b_i(x) =: \mathbf{H}^{\mathrm{T}}(x-s)\mathbf{b}(x) \tag{9}$$

and $\mathbf{H}(x-s)$ is the vector of basis functions,

$$\mathbf{H}^{\mathrm{T}}(x-s) = [1, x-s, (x-s)^2, \ldots, (x-s)^n] \tag{10}$$

and $\mathbf{b}^{\mathrm{T}}(x) = [b_0(x), b_1(x), b_2(x), \ldots, b_n(x)]$ is the coefficient vector. By introducing a Taylor expansion on $u(s)$ in (7), we have

$$u^R(x) = \overline{m}_0(x)u(x) + \sum_{i=1}^{\infty} \frac{(-1)^i}{i!} \overline{m}_i(x) u^{(i)}(x) \tag{11}$$

where $\overline{m}_i(x)$ is the i-th moment of $\overline{\phi}_a$ and is defined as

$$\begin{aligned} \overline{m}_i(x) &= \int_\Omega (x-s)^i \overline{\phi}_a(x; x-s)\mathrm{d}s \\ &= \int_\Omega (x-s)^i \left(\sum_{k=0}^{n} b_k(x)(x-s)^k \right) \phi_a(x-s)\mathrm{d}s \\ &= \sum_{k=0}^{n} b_k(x)\, m_{i+k}(x) \end{aligned} \tag{12}$$

where $m_i(x)$ is defined as in (5). The reproducing conditions for nth-pleteness in the RK approximation in (11) are now

$$\begin{aligned} &\overline{m}_0 = 1, \\ &\overline{m}_i = 0, \quad \text{for} \;\; 1 \le i \le n \end{aligned} \tag{13}$$

The equations in (13) can be expressed as the following set of equations:

$$\mathbf{M}(x)\mathbf{b}(x) = \mathbf{H}(0) \tag{14}$$

where $\mathbf{M}(x)$ is called the moment matrix with respect to the kernel $\phi_a(x)$, and is expressed as

$$\mathbf{M}(x) = \begin{bmatrix} m_0(x) & m_1(x) & \cdots & m_n(x) \\ m_1(x) & m_2(x) & \cdots & m_{n+1}(x) \\ \vdots & \vdots & \ddots & \vdots \\ m_n(x) & m_{n+1}(x) & \cdots & m_{2n}(x) \end{bmatrix} \tag{15}$$

It can be easily shown that $\mathbf{M}(x)$ can be expressed by the vector of basis functions $\mathbf{H}$ as

$$\mathbf{M}(x) = \int_\Omega \mathbf{H}(x-s)\mathbf{H}^{\mathrm{T}}(x-s)\phi_a(x-s)\mathrm{d}s \tag{16}$$

By obtaining the coefficient vector $\mathbf{b}(x)$ from (14), and substituting it back into (7), the RK approximation in one dimension can now be expressed as

$$u^R(x) = \mathbf{H}^{\mathrm{T}}(0)\mathbf{M}^{-1}(x) \int_\Omega \mathbf{H}(x-s)\phi_a(x-s)u(s)\mathrm{d}s \tag{17}$$

The derivation above demonstrates the basic construction of the RK approximation. This construction, however, becomes tedious in multidimensions. An alternative approach can be used to obtain the RK approximation (Chen *et al.*, 2000) as follows. Consider the imposition of the n-th omial reproducing conditions to the RK approximation in (7) as

$$\int_\Omega C(x; x-s)\phi_a(x-s)s^i \mathrm{d}s = x^i, \quad i = 0, \ldots, n \tag{18}$$

or equivalently,

$$\int_\Omega C(x;x-s)\phi_a(x-s)(x-s)^i \mathrm{d}s = \delta_{i0}, \quad i = 0, \ldots, n \tag{19}$$

The above equation can be further written as

$$\int_\Omega C(x;x-s)\phi_a(x-s)\mathbf{H}(x-s)\mathrm{d}s = \mathbf{H}(0) \tag{20}$$

Substituting the correction function $C(x;x-s)$ in (9) into (20) yields the same linear system as that in (14) for solving coefficient vector $\mathbf{b}(x)$, and consequently the same final form of the RK approximation in (17).

With this approach, the multidimensional RK approximation can be written as

$$u^R(\mathbf{x}) = \int_\Omega C(\mathbf{x};\mathbf{x}-\mathbf{s})\phi_a(\mathbf{x}-\mathbf{s})u(\mathbf{s})\mathrm{d}\mathbf{s} \tag{21}$$

The correction function $C(\mathbf{x};\mathbf{x}-\mathbf{s})$ in multidimensions is expressed as the linear combination of monomial bases:

$$\begin{aligned} &C(\mathbf{x};\mathbf{x}-\mathbf{s}) \\ &= \sum_{i+j+k=0}^{n} b_{ijk}(\mathbf{x})(x_1-s_1)^i(x_2-s_2)^j(x_3-s_3)^k, \quad n \geq 0 \\ &= \mathbf{H}^T(\mathbf{x}-\mathbf{s})\mathbf{b}(\mathbf{x}) \end{aligned} \tag{22}$$

and $\mathbf{H}(\mathbf{x}-\mathbf{s})$ is the vector of basis functions:

$$\mathbf{H}^{\mathrm{T}}(\mathbf{x}-\mathbf{s}) = [1, x_1-s_1, x_2-s_2, \ldots, (x_3-s_3)^n] \tag{23}$$

The coefficient vector $\mathbf{b}^{\mathrm{T}}(\mathbf{x}) = [b_{000}(\mathbf{x}), b_{100}(\mathbf{x}), b_{010}(\mathbf{x}), \ldots, b_{003}(\mathbf{x})]$ is solved by enforcing n monomials reproducibility:

$$\begin{aligned} &\int_\Omega C(\mathbf{x};\mathbf{x}-\mathbf{s})\phi_a(\mathbf{x}-\mathbf{s}){s_1}^i{s_2}^j{s_3}^k \,\mathrm{d}\mathbf{s} \\ &\qquad = {x_1}^i{x_2}^j{x_3}^k, \quad 0 \leq i+j+k \leq n \end{aligned} \tag{24}$$

Equation (24) can be rewritten as:

$$\begin{aligned} &\int_\Omega C(\mathbf{x};\mathbf{x}-\mathbf{s})\phi_a(\mathbf{x}-\mathbf{s})(x_1-s_1)^i(x_2-s_2)^j(x_3-s_3)^k\mathrm{d}\mathbf{s} \\ &\qquad = \delta_{i0}\delta_{j0}\delta_{k0}, \quad 0 \leq i+j+k \end{aligned} \tag{25}$$

or,

$$\int_\Omega C(\mathbf{x};\mathbf{x}-\mathbf{s})\phi_a(\mathbf{x}-\mathbf{s})\mathbf{H}(\mathbf{x}-\mathbf{s})\mathrm{d}\mathbf{s} = \mathbf{H}(\mathbf{0}) \tag{26}$$

Introducing the correction function in (22) into (26) yields the following equation:

$$\left(\int_\Omega \mathbf{H}(\mathbf{x}-\mathbf{s})\mathbf{H}^T(\mathbf{x}-\mathbf{s})\phi_a(\mathbf{x}-\mathbf{s})\mathrm{d}s\right)\mathbf{b}(\mathbf{x}) = \mathbf{H}(\mathbf{0}) \tag{27}$$

By solving $\mathbf{b}(\mathbf{x})$ from (27), the multidimensional RK approximation is obtained:

$$u^R(\mathbf{x}) = \mathbf{H}^T(\mathbf{0})\mathbf{M}^{-1}(\mathbf{x})\int_\Omega \mathbf{H}(\mathbf{x}-\mathbf{s})\phi_a(\mathbf{x}-\mathbf{s})u(\mathbf{s})\mathrm{d}\mathbf{s} \tag{28}$$

where

$$\mathbf{M}(\mathbf{x}) = \int_\Omega \mathbf{H}(\mathbf{x}-s)\mathbf{H}^T(\mathbf{x}-s)\phi_a(\mathbf{x}-s)\mathrm{d}\mathbf{s} \tag{29}$$

Here, $\mathbf{M}(\mathbf{x})$ is the multidimensional moment matrix, and $\phi_a(\mathbf{x}-\mathbf{s})$ is the multidimensional kernel function that can be constructed by using the kernel function in one dimension by either of the two following ways:

$$\begin{aligned} (1) \quad \phi_a(\mathbf{x}-\mathbf{s}) &= \prod_{i=1}^{3}\phi_{a_i}(x_i-s_i) \\ &= \phi_{a_1}(x_1-s_1)\phi_{a_2}(x_2-s_2)\phi_{a_3}(x_3-s_3) \end{aligned} \tag{30}$$

$$(2) \quad \phi_a(\mathbf{x}-s) = \phi_a(z), \quad z = \frac{\|\mathbf{x}-\mathbf{s}\|}{a} \tag{31}$$

The kernel function defined in (30) has rectangular cuboid support while the one defined in (31) has spherical support, such as those shown in Figure 3 for the supports of two-dimensional kernel functions.

Note that $\mathbf{M}(\mathbf{x})$ is the Gram matrix of the basis functions in $\mathbf{H}(\mathbf{x}-\mathbf{s})$ with respect to $\phi_a(\mathbf{x}-s)$, and $\mathbf{M}(\mathbf{x})$ is positive definite if the basis functions in $\mathbf{H}(\mathbf{x}-\mathbf{s})$ are linearly independent

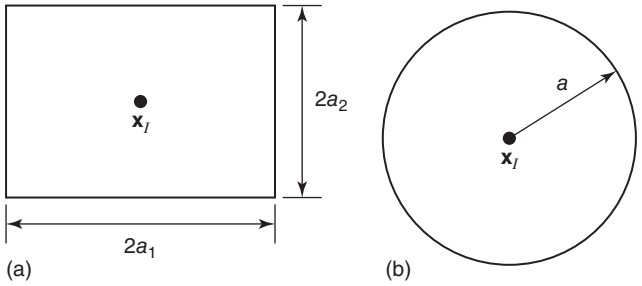

Figure 3. (a) Rectangular and (b) circular supports of two-dimensional kernel function $\phi_a(\mathbf{x}-\mathbf{s})$ corresponding to (30) and (31), respectively. (Reproduced from Chen (2015). © Chen, 2015.)

and $\phi_a(\mathbf{x}-\boldsymbol{s})>0$ for $\|\mathbf{x}-\boldsymbol{s}\|<a$. For the discrete RK approximation, on the other hand, a sufficient number of nodal supports have to cover the point $\mathbf{x}$ for $\mathbf{M}(\mathbf{x})$ to be positive definite, which will be discussed in the next section.

To construct the approximation functions for the finite dimensional solution of PDEs based on the RK approximation, discretization of the continuous RK function in (28) is needed. However, discretization of the continuous RK approximation yields violation of the reproducing conditions and consequently monomials are not exactly reproduced (Chen *et al.*, 1996). In the following, a discrete RK approximation is formulated directly from a discrete form (Chen *et al.*, 1998).

2.2 Discrete reproducing kernel approximation

Consider the domain of interest $\overline{\Omega}=\Omega\cup\partial\Omega$ discretized by a set of points $S=\{\mathbf{x}_1,\mathbf{x}_2,\ \dots\ ,\mathbf{x}_{Np}|\mathbf{x}_I\in\overline{\Omega}\}$, and let the approximation of a function u, denoted by u^h, be constructed using information at discrete points in the set S as follows:

$$u^h(\mathbf{x})=\sum_{I=1}^{Np}\Psi_I(\mathbf{x})d_I \tag{32}$$

where $\Psi_I(\mathbf{x})$ is the shape function of node I positioned at $\mathbf{x}_I$, and d_I is the coefficient to be sought. In the RK approximation, the construction of shape functions is based entirely on point data. The RK shape functions are constructed as follows (Liu *et al.*, 1995a; Chen *et al.*, 1996) with consideration of discrete reproducing conditions (Chen *et al.*, 1998):

$$\Psi_I(\mathbf{x})=C(\mathbf{x};\mathbf{x}-\mathbf{x}_I)\phi_a(\mathbf{x}-\mathbf{x}_I) \tag{33}$$

where $\phi_a(\mathbf{x}-\mathbf{x}_I)$ is the kernel function with compact support measured by the support dimension a, and $C(\mathbf{x};\mathbf{x}-\mathbf{x}_I)$ is the correction function composed of monomial bases:

$$C(\mathbf{x};\mathbf{x}-\mathbf{x}_I)=\sum_{i+j+k=0}^{n}b_{ijk}(\mathbf{x})(x_1-x_{1I})^i(x_2-x_{2I})^j(x_3-x_{3I})^k,\quad n\geq 0 \tag{34}$$

where n represents the degree of monomial bases, and $b_{ijk}(\mathbf{x})$ are coefficients obtained by the following discrete reproducing conditions (Chen *et al.*, 1998):

$$\sum_{I=1}^{Np}\Psi_I(\mathbf{x})x_{1I}^i x_{2I}^j x_{3I}^k=x_1^i x_2^j x_3^k,\quad i+j+k=0,1,\ \dots\ ,n \tag{35}$$

Obtaining $b_{ijk}(\mathbf{x})$ from (35) yields the following RK shape function:

$$\Psi_I(\mathbf{x})=\mathbf{H}^{\mathrm{T}}(\mathbf{0})\mathbf{M}^{-1}(\mathbf{x})\mathbf{H}(\mathbf{x}-\mathbf{x}_I)\phi_a(\mathbf{x}-\mathbf{x}_I) \tag{36}$$

$$\mathbf{M}(\mathbf{x})=\sum_{I=1}^{Np}\mathbf{H}(\mathbf{x}-\mathbf{x}_I)\mathbf{H}^{\mathrm{T}}(\mathbf{x}-\mathbf{x}_I)\phi_a(\mathbf{x}-\mathbf{x}_I) \tag{37}$$

$$\mathbf{H}^{\mathrm{T}}(\mathbf{x}-\mathbf{x}_I)=[1,x_1-x_{1I},x_2-x_{2I},\ \dots\ ,(x_3-x_{3I})^n] \tag{38}$$

In the RK approximation, the kernel function ϕ_a has a compact support a and it determines the continuity of the approximation; for example, the cubic B-spline function is C^2 continuous. The degree of monomial basis functions n in the correction function $C(\mathbf{x};\mathbf{x}-\mathbf{x}_I)$ controls the order of completeness in the approximation, which is related to the order of consistency when introducing the RK approximation to solve PDEs. For the moment matrix $\mathbf{M}(\mathbf{x})$ to be nonsingular, the compact support of the kernel function has to be sufficiently large to keep the reproducing conditions in (35) linearly independent (Chen *et al.*, 1996). A typical RK discretization using circular supports is shown in Figure 1(b), where the support of node I is shaded in grey. The corresponding shape function over the node's compact support is also shown in Figure 1(b).

It should be noted that the RK approximation discussed above in general does not possess the Kronecker delta property and hence the approximation is not kinematically admissible on the essential boundary unless techniques such as transformation (Chen *et al.*, 1996; Zhu and Atluri, 1998; Günther and Liu, 1998; Atluri *et al.*, 1999; Wagner and Liu, 2000; Chen and Wang, 2000), coupling with finite elements near the essential boundary (Krongauz and Belytschko, 1996; Fernández-Méndez and Huerta, 2004), or modifications to the RK approximation near the essential boundary (Chen and Wang, 2000; Gosz and Liu, 1996; Kaljevic and Saigal, 1997; Chen *et al.*, 2003) are introduced. With standard RK approximations that are not kinematically admissible, the essential boundary conditions have to be imposed by methods such as the penalty method (Zhu and Atluri, 1998; Atluri and Zhu, 1998), Nitsche's method (Nitsche, 1971; Griebel and Schweitzer, 2003; Babuška *et al.*, 2003), the modified variational principle (Lu *et al.*, 1994), or the Lagrange multiplier method (Belytschko *et al.*, 1994).

The RKPM (Liu *et al.*, 1995a; Chen *et al.*, 1996) introduces the RK approximation for solving PDEs under the Galerkin framework. For demonstration, consider here Poisson's equation with Dirichlet boundary conditions:

$$\begin{aligned}\nabla^2 u+Q&=0\quad\text{in }\Omega\\ u&=g\quad\text{on }\partial\Omega\end{aligned} \tag{39}$$

For easy demonstration, here we consider RK approximation to be kinematically admissible, which can be achieved using the methods mentioned previously. The Galerkin approximation that corresponds to (39) is to find $u^h \in H_0^1$, $\forall v^h \in H_g^1$,

$$\int_\Omega \nabla v^h \cdot \nabla u^h d\Omega = \int_\Omega v^h Q \mathrm{d}\Omega \tag{40}$$

where u^h and v^h are approximations of u and v, respectively. A more comprehensive discussion on imposition of essential boundary conditions for RK approximations that are not kinematically admissible is given in Section 6.

The convergence of RKPM with the RK approximation of degree n has been shown (Liu *et al.*, 1997b; Chen *et al.,* 2003; Han and Meng, 2001) to be

$$\left\| u - u^h \right\|_{\ell,\Omega} \leq C a^{n+1-\ell} |u|_{n+1,\Omega}, \quad \ell \geq 0 \tag{41}$$

where a is the maximal support dimension of RK shape functions and C is independent of a and n. This algebraic convergence behavior is very similar to that of the finite element approximation considering the proportionality of the support dimension a and the nodal distance h.

2.3 Implicit gradients

The implicit gradient was introduced as a regularization in strain localization problems without taking direct derivatives (Chen *et al.,* 2004), where the idea came directly from the synchronized RK approximation (Li and Liu, 1998, 1999a,b) as a way to approximate derivatives:

$$D_{ijk} u(\mathbf{x}) \simeq \sum_{I=1}^{Np} \overline{\Psi}_I^{ijk}(\mathbf{x}) u_I \tag{42}$$

where $D_{ijk}(\cdot) = \partial^{i+j+k} / \partial x_1^i \partial x_2^j \partial x_3^k$. Derivative approximations are constructed directly by employing the same form as the RK shape function (33):

$$\overline{\Psi}_I^{ijk}((\mathbf{x})) = \overline{C}^{ijk}(\mathbf{x}; \mathbf{x} - \mathbf{x}_I) \phi_a(\mathbf{x} - \mathbf{x}_I) \tag{43}$$

The correction function $\overline{C}^{ijk}(\mathbf{x}; \mathbf{x} - \mathbf{x}_I)$ is expressed as a linear combination of monomials as in (34), the coefficients of which are obtained from the following *gradient reproducing conditions*, analogous to (35) (see (Chen *et al.*, 2004) for details):

$$\sum_{I=1}^{Np} \overline{\Psi}_I^{ijk}(\mathbf{x}) x_{1I}^p x_{2I}^q x_{3I}^r = D_{ijk}(x_1^p x_2^q x_3^r), \quad 0 \leq p+q+r \leq n \tag{44}$$

The equation in (44) is equivalent to (Chen *et al.*, 2004):

$$\sum_{I=1}^{Np} \overline{\Psi}_I^{ijk}(\mathbf{x})(x_1 - x_{1I})^p (x_2 - x_{2I})^q (x_3 - x_{3I})^r = \delta_{ip}\delta_{jq}\delta_{kr}(-1)^{p+q+r} p!q!r!, \quad 0 \leq p+q+r \leq n \tag{45}$$

Following the procedures in the discrete RK approximation, one obtains the implicit gradient RK approximation:

$$\overline{\Psi}_I^{ijk}(\mathbf{x}) = (\overline{\mathbf{H}}^{ijk})^{\mathrm{T}} \mathbf{M}(\mathbf{x})^{-1} \mathbf{H}(\mathbf{x} - \mathbf{x}_I) \phi_a(\mathbf{x} - \mathbf{x}_I) \tag{46}$$

$$\mathbf{M}(\mathbf{x}) = \sum_{I=1}^{Np} \mathbf{H}(\mathbf{x} - \mathbf{x}_I) \mathbf{H}^{\mathrm{T}}(\mathbf{x} - \mathbf{x}_I) \phi_a(\mathbf{x} - \mathbf{x}_I) \tag{47}$$

where $\overline{\mathbf{H}}^{ijk}$ is the column vector of $\{\delta_{ip}\delta_{jq}\delta_{kr}(-1)^{p+q+r} p\,!\, q\,!\, r\,!\}_{0 \leq p+q+r \leq n}$. Implicit gradients have been employed for regularization in strain localization problems (Chen *et al.*, 2004) to avoid the need for ambiguous boundary conditions associated with the standard gradient-type regularization methods, and they have also been used to ease the computational cost of meshfree collocation methods (Chi *et al.*, 2013) and stabilization of nodal integration (Hillman and Chen, 2016; Chen *et al.*, 2007).

The implicit gradients in (46) have the same expression as the synchronized derivatives proposed in (Li and Liu, 1998,1999a,b), scaled by $p\,!\, q\,!\, r\,!$, with the difference in sign emanating from the convention in shifting the bases. In this form, the reproduction of derivative terms can be seen by employing vanishing moment conditions alternative to (13). Using this idea, in (Li and Liu, 1998) it was shown that employing certain linear combinations of synchronized derivatives and the RK approximation, synchronized convergence can be obtained in the L^2 norm and H^s norms up to the some order s with the proper selection of coefficients β^{ijk} in the following:

$$\widehat{\Psi}_I(\mathbf{x}) = \Psi_I(\mathbf{x}) + \sum_{i+j+k=0}^{n} \beta^{ijk} \overline{\Psi}_I^{ijk}(\mathbf{x}) \tag{48}$$

Since the additional terms in the above satisfy partition of nullity, the resulting approximation (48) is termed the hierarchical partition of unity (Li and Liu, 1999a). Synchronized derivatives have been developed for improving accuracy in the Helmholtz equation, obtaining high resolution in localization problems and avoiding the need to evaluate expensive derivatives in the stabilized meshfree approach for computational fluid dynamics (Li and Liu, 1999b).

3 A UNIFICATION WITH THE PERIDYNAMIC THEORY

Silling *et al.* (2007) developed the current peridynamic theory (state-based peridynamics) after overcoming the limitations introduced by the original (bond-based) peridynamic theory (Silling, 2000), which restricted the types of material responses that could be modeled, the most evident being the restriction to the value of the Poisson ratio. Peridynamics is presented as an alternative formulation to classical continuum mechanics because it is based on the concept that material stresses are not the result of forces acting on infinitesimal areas; rather they are the result of a nonlocal interaction between material points lying within a finite region surrounding each point; see Figure 4.

This nonlocality argument is a central concept for building the peridynamic theory where the deformation in each point is described with tensors associated with finite regions, instead of infinitesimal ones. A point $\mathbf{X}_I$ in the reference configuration is considered to be influenced by its neighboring points $\mathbf{X}_J$ within a distance called the horizon or the smoothing length, which forms a local domain $\mathcal{H}_{\mathbf{X}_I}$ around each point, called the compact support of that point in the remaining meshfree literature. For convenience, the relative position vector from material point $\mathbf{X}_I$ to the material point $\mathbf{X}_J$ in the reference configuration is written as $\mathbf{X}_{I:J} = \mathbf{X}_J - \mathbf{X}_I$, and is referred as reference bond $\mathbf{X}_{I:J}$. Once the body deforms the position vectors in the deformed configuration are denoted as usual by lowercase bold letters, for example, the deformed bond is then $\mathbf{x}_{I:J} = \mathbf{x}_J - \mathbf{x}_I$.

Starting from the undeformed configuration, it is assumed that the moment tensor of the reference bonds describes the compact support region $\mathcal{H}_{\mathbf{X}_I}$ fully:

$$\begin{aligned}\mathbf{K}_I &= \int_{\mathcal{H}_{\mathbf{X}_I}} \phi_a(\mathbf{X}_J - \mathbf{X}_I)(\mathbf{X}_J - \mathbf{X}_I) \otimes (\mathbf{X}_J - \mathbf{X}_I) \mathrm{d}\mathbf{V}_{\mathbf{X}_I} \\ &= \int_{\mathcal{H}_{\mathbf{X}_I}} \phi^a_{I:J} \mathbf{X}_{I:J} \otimes \mathbf{X}_{I:J} \mathrm{d}\mathbf{V}_{\mathbf{X}_I} \end{aligned} \tag{49}$$

where $\mathbf{K}_I$ is called the reference shape tensor and where $\phi^a_{I:J} = \phi_a(\mathbf{X}_J - \mathbf{X}_I)$ is the influence function, common to other meshfree methods as introduced in Section 2. We note the use of the compact notation avoiding the need to write all the subtraction terms for convenience. The deformed shape tensor describing the deformed compact support region $\mathcal{H}_{\mathbf{x}_I}$ is then given by

$$\mathbf{\Lambda}_I = \int_{\mathcal{H}_{X_I}} \phi^a{}_{I:J} \underline{\mathbf{F}}\langle \mathbf{X}_{I:J} \rangle \otimes \mathbf{X}_{I:J} \mathrm{d}\mathbf{V}_{\mathbf{X}_I} \tag{50}$$

with $\underline{\mathbf{F}}\langle \mathbf{X}_{I:J} \rangle = \mathbf{x}_{I:J} = \mathbf{x}_J - \mathbf{x}_I$ being the general map that transforms the reference bond $\mathbf{X}_{I:J}$ in the current bond $\mathbf{x}_{I:J}$. This general map is commonly referred as vector state; all vector states are denoted by underlined bold capital letters henceforth.

The peridynamic theory then postulates that the deformation at each point is associated to a relationship between the undeformed and deformed shape tensors, forming a nonlocal deformation gradient:

$$\begin{aligned}\boldsymbol{\mathcal{F}}_I = \mathbf{\Lambda}_I \cdot \mathbf{K}_I^{-1} &= \left(\int_{\mathcal{H}_{\mathbf{X}_I}} \phi^a_{I:J} \mathbf{x}_{I:J} \otimes \mathbf{X}_{I:J} \mathrm{d}\mathbf{V}_{\mathbf{X}_I} \right) \\ &\cdot \left(\int_{\mathcal{H}_{\mathbf{X}_I}} \phi^a_{I:J} \mathbf{X}_{I:J} \otimes \mathbf{X}_{I:J} \mathrm{d}\mathbf{V}_{\mathbf{X}_I} \right)^{-1} \end{aligned} \tag{51}$$

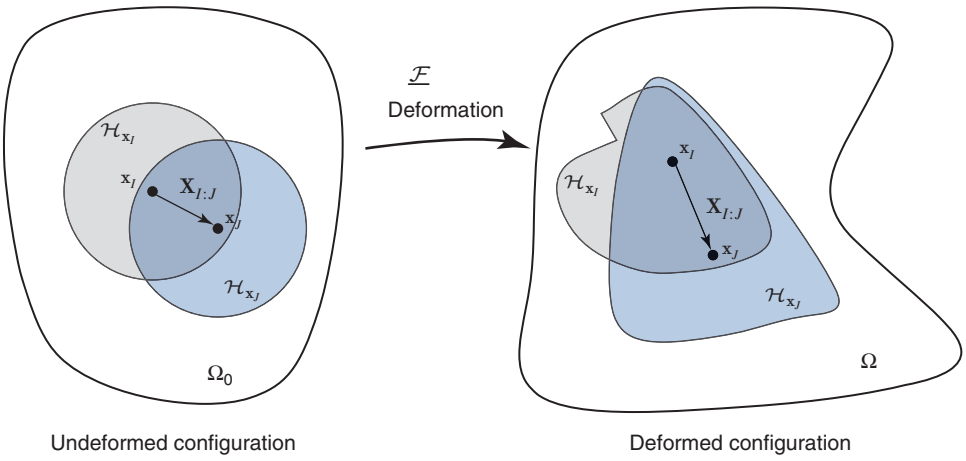

Figure 4. Peridynamics continuum before and after deformation.

which has its local counterpart in the local deformation gradient defined in classical continuum mechanics as a tensor that acts on infinitesimal line segments:

$$d\mathbf{x} = \mathbf{F} \cdot d\mathbf{X} \rightarrow \mathbf{F} = \frac{d\mathbf{x}}{d\mathbf{X}} \tag{52}$$

Before continuing to evaluate the description of the stresses in the peridynamic theory, let us first focus on the nonlocal deformation gradient given by (51) and in comparing its discretized value for a uniform grid with the discretized calculation of the local deformation gradient via the RKPM using synchronized derivatives for the same grid.

3.1 Comparing the deformation gradient in peridynamics and RKPM with synchronized derivatives

Discretizing (51) we obtain the peridynamics approximation for the deformation gradient:

$$\boldsymbol{\mathcal{F}}_I = \left(\sum_{J=1}^{Np} \phi_a(\mathbf{X}_J - \mathbf{X}_I)(\mathbf{x}_J - \mathbf{x}_I) \otimes (\mathbf{X}_J - \mathbf{X}_I) W_I \right) \cdot \mathbf{K}_I^{-1} \tag{53}$$

where $W_I = \int_{\mathcal{H}_{\mathbf{x}_I}} d\Omega$ and the shape tensor discretized as

$$\mathbf{K}_I = \sum_{J=1}^{N_p} \phi_a(\mathbf{X}_J - \mathbf{X}_I)(\mathbf{X}_J - \mathbf{X}_I) \otimes (\mathbf{X}_J - \mathbf{X}_I) W_I \tag{54}$$

Now, if we consider the simplest case of having a one-dimensional uniform grid of points separated by the same distance ΔX (see Figure 5) we can compute the deformation gradient given by peridynamics very easily. Considering a number of points within the compact support of Np, labeled from zero (central point) to $M+$ points to the right of point zero and $M-$ points to the left, the shape tensor reduces to the simple expression:

$$K_0 = \sum_{J=1}^{M} (2J^2 \phi_J^a) \Delta X^2 W, \quad M = \frac{Np-1}{2} \tag{55}$$

where $W = W_0$, $\phi_J^a = \phi_a(X_J - X_0) = \phi_a(X_0 - X_J)$. Similarly, the deformation gradient then becomes

$$\boldsymbol{\mathcal{F}}_0 = \frac{dx_0}{dX} = \left(\sum_{J=1}^{M} \phi_J^a [(x_0 - x_{J+})(X_0 - X_{J+}) + (x_0 - x_{J-})(X_0 - X_{J-})] W \right) K_0^{-1}, \quad M = \frac{Np-1}{2} \tag{56}$$

which can be simplified noting that $X_0 - X_{J-} = J\Delta X$, $X_0 - X_{J+} = -J\Delta X$, and using (54),

$$\boldsymbol{\mathcal{F}}_0 = \frac{dx_0}{dX} = \left(\sum_{J=1}^{M} J \phi_J^a (x_{J+} - x_{J-}) \Delta X W \right) K_0^{-1} = \frac{\sum_{J=1}^{M} J \phi_J^a (x_{J+} - x_{J-})}{\sum_{J=1}^{M} (2J^2 \phi_J^a) \Delta X}, \quad M = \frac{Np-1}{2} \tag{57}$$

We are now in a position to compare this result for the approximation to the deformation gradient using peridynamics with the approximation obtained via RKPM using synchronized derivatives. As referred to in Section 2, the RK framework represents a general approach for approximating any function by a convolution integral. In a general form, the corresponding discrete form may be given by

$$u^h(\mathbf{X}, \mathbf{S}) = \mathbf{H}^T(\mathbf{X} - \mathbf{S}) \bar{\mathbf{b}}(\mathbf{X}) \tag{58}$$

where $\mathbf{H}(\mathbf{X})$ is a complete polynomial of degree n with $n+1$ monomials, and $\bar{\mathbf{b}}(\mathbf{X})$ is the vector composed by non-constant coefficients that depend on the position where they are being calculated:

$$\bar{\mathbf{b}}(\mathbf{X}) = \mathbf{M}(\mathbf{X})^{-1} \sum_{I=1}^{Np} \phi_a(\mathbf{X} - \mathbf{X}_I) \mathbf{H}(\mathbf{X} - \mathbf{X}_I) \boldsymbol{u}_I W_I \tag{59}$$

with the moment matrix given by

$$\mathbf{M}(\mathbf{X}) = \sum_{I=1}^{Np} \phi_a(\mathbf{X} - \mathbf{X}_I) \mathbf{H}(\mathbf{X} - \mathbf{X}_I) \mathbf{H}^T(\mathbf{X} - \mathbf{X}_I) W_I \tag{60}$$

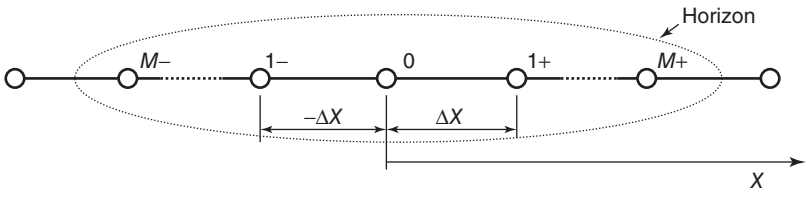

Figure 5. One-dimensional bar discretized by uniformly spaced points.

The discretized RK approximation is then given by

$$u^h(\mathbf{X},\mathbf{S}) = \mathbf{H}^T(\mathbf{X}-\mathbf{S})\mathbf{M}(\mathbf{X})^{-1}\sum_{I=1}^{Np}\phi_a(\mathbf{X}-\mathbf{X}_I)\mathbf{H}(\mathbf{X}-\mathbf{X}_I)\boldsymbol{u}_I W_I \tag{61}$$

This approximation has the unusual characteristic of depending on two independent variables giving the positions of a cloud of points within the compact support: **x** and **s**. This allows the approximation of the function u^h by different ways. We can consider that $\mathbf{S}=\mathbf{X}$, which means that we are evaluating the polynomial approximation by having non-constant coefficients $\overline{\mathbf{b}}(\mathbf{X})$ varying within the compact support region:

$$u^h(\mathbf{X}) = \mathbf{H}^T(\mathbf{0})\overline{\mathbf{b}}(\mathbf{X}) \tag{62}$$

Or, we can consider that we want to approximate the value of the function u^h at any point **s** in the compact support domain relative to a fixed point $\boldsymbol{X}=\boldsymbol{X}_J$:

$$u^h(\mathbf{S}) = \mathbf{H}^T(\mathbf{X}_J-\mathbf{S})\overline{\mathbf{b}}(\mathbf{X}_J) \tag{63}$$

The choice of approximating any function using (62) or using (63) has evident implications on the approximation for the *derivatives* of that function of interest. In particular, if the choice is to use (63) then computing the derivatives at any point is given by

$$\frac{\partial u^h(\mathbf{S})}{\partial \mathbf{S}} = \frac{\partial \mathbf{H}^T(\boldsymbol{X}_J-\mathbf{S})}{\partial \boldsymbol{S}}\overline{\mathbf{b}}(\boldsymbol{X}_J) \tag{64}$$

This approximation to the derivative is called the *synchronized derivative*, or diffuse derivative as referred to in Section 2.3.

Using (64) for the one-dimensional bar problem enables obtaining the deformation gradient from RKPM with synchronized derivatives that can then be compared with the result for the deformation gradient obtained with peridynamics given by (57). Consider a general polynomial basis of degree n with $n+1$ monomials in one dimension that approximates any function around the point $X=X_J$ of the one-dimensional bar in Figure 5:

$$\mathbf{H}^T(X_J-S) = \left[1\ \ (X_J-S)\ \ (X_J-S)^2\ \ \cdots\ \ (X_J-S)^n\right] \tag{65}$$

$$\overline{\mathbf{b}}^T(X_J) = \left[\overline{b}_0(X_J)\ \ \overline{b}_1(X_J)\ \ \overline{b}_2(X_J)\ \ \cdots\ \ \overline{b}_n(X_J)\right] \tag{66}$$

For this general polynomial basis and its respective coefficients it is trivial to obtain the RK approximation for any function; in particular, we can approximate the current position of the deformed one-dimensional bar x, considering $u^h(s)=x(s)=x$ in equation (213):

$$x(S) = \overline{b}_0(X_J) + (X_J-S)\overline{b}_1(X_J) + (X_J-S)^2\overline{b}_2(X_J) + \cdots + (X_J-S)^k\overline{b}_n(X_J) \tag{67}$$

from which we can obtain the approximation for the derivative with respect to the undeformed position (deformation gradient) as:

$$F = \frac{\mathrm{d}x}{\mathrm{d}S} = -\overline{b}_1(X_J) - (X_J-S)\overline{b}_2(X_J) - \cdots - (X_J-S)^{n-1}\overline{b}_n(X_J) \tag{68}$$

And in particular, if we are interested in obtaining the derivative at the point $S=X_J$ we get the following simple result:

$$F_J = \frac{\mathrm{d}x_J}{\mathrm{d}S} = -\overline{b}_1(X_J) \tag{69}$$

With this result and using (59), it is then possible to obtain the approximation for the deformation gradient of the one-dimensional bar at any point. We set $x_J=x_0$ and compute the coefficient $\overline{\boldsymbol{b}}_1(\boldsymbol{X}_0)$ to get to the same result we obtained when using the peridynamics approximation in (57):

$$F_0 = \frac{\mathrm{d}x_0}{\mathrm{d}X} = \frac{\sum_{J=1}^{M} J\phi_J^a(x_{J^+}-x_{J^-})}{\sum_{J=1}^{M}(2J^2\phi_J^a)\Delta X}, \quad M=\frac{Np-1}{2} \tag{70}$$

This was first discovered in Bessa *et al.* (2014) where it was also shown that the result can be obtained for two-dimensional and three-dimensional uniform grids. This result can be in part regarded as intuitive since

- observing (60) for the discretized moment matrix $\mathbf{M}(\mathbf{X})$ of RKPM and (54) for the discretized shape tensor $\mathbf{K}$ in peridynamics we see that the latter is contained as a submatrix of the former.

In other words, the peridynamic theory obtains directly the deformation gradient by considering a polynomial basis formed uniquely by the first-order terms ($n=1$) and disregarding all the other terms ($n=0$ and $n>1$) for the shape tensor and without explicitly calculating any derivatives.

3.2 Peridynamic description of divergence of stress and another link to RKPM

The nonlocal aspect of the peridynamic theory has a direct influence on the description of the balance of linear momentum equation,

$$\rho\ddot{\mathbf{u}}[\mathbf{X}_I,t] = \boldsymbol{\nabla}\cdot\boldsymbol{\sigma}[\mathbf{X}_I,t] + \mathbf{b}[\mathbf{X}_I,t] \leftrightarrow \rho\ddot{\mathbf{u}}_I = \boldsymbol{\nabla}\cdot\boldsymbol{\sigma}_I + \mathbf{b}_I \tag{71}$$

Since it replaces the divergence of stress $\nabla\cdot\sigma_I$ by the following integral expression

$$\boldsymbol{\nabla}\cdot\boldsymbol{\sigma}[\mathbf{X}_I,t] \rightarrow \int_{\mathcal{H}_{\mathbf{X}_I}} (\underline{\mathbf{T}}[\mathbf{X}_I t]\langle\mathbf{X}_{I:J}\rangle - \underline{\mathbf{T}}[\mathbf{X}_J,t]\langle\mathbf{X}_{J:I}\rangle)\mathrm{d}\Omega \tag{72}$$

where $\underline{\mathbf{T}}[\mathbf{X}_A,t]\langle\boldsymbol{X}_{I:J}\rangle$ is the general map (vector state) that acts on the reference bond $\mathbf{X}_{I:J}$ to produce a force per unit volume that is reciprocal to the force per unit volume generated by the reference bond $\mathbf{X}_{J:I}$. In particular, Silling *et al.* (2007) proposed a particular map where it is possible to establish a direct connection to the classical notion of stress:

$$\underline{\mathbf{T}}[\mathbf{X}_A,t]\mathbf{X}_{A:B} = \phi_a(\mathbf{X}_B-\mathbf{X}_A)\boldsymbol{\sigma}[\mathbf{X}_A,\mathbf{t}]\cdot\mathbf{K}[\mathbf{X}_A]^{-1}\cdot(\mathbf{X}_B-\mathbf{X}_A) \tag{73}$$

which can be replaced in (72) to give

$$\nabla\cdot\boldsymbol{\sigma}[\mathbf{X}_I,t] \rightarrow \int_{\mathcal{H}_{\mathbf{X}_I}} (\phi_a(\mathbf{X}_J-\mathbf{X}_I)(\boldsymbol{\sigma}[\mathbf{X}_J t] \cdot\mathbf{K}[\mathbf{X}_J]^{-1} + \boldsymbol{\sigma}[\mathbf{X}_I,t]\cdot\mathbf{K}[\mathbf{X}_I]^{-1})\cdot(\mathbf{X}_J-\mathbf{X}_I)\mathrm{d}\Omega \tag{74}$$

This result can be discretized as before by replacing the integral expression by a summation over the cloud of points within the compact support family $\mathcal{H}_{\mathbf{X}_I}$:

$$\boldsymbol{\nabla}\cdot\boldsymbol{\sigma}[\mathbf{X}_I,t] \rightarrow \sum_{J=1}^{Np}(\phi_a(\mathbf{X}_J-\mathbf{X}_I)(\boldsymbol{\sigma}[\mathbf{X}_J t]\cdot\mathbf{K}[\mathbf{X}_J]^{-1} + \boldsymbol{\sigma}[\mathbf{X}_I,t]\cdot\mathbf{K}[\mathbf{X}_I]^{-1})\cdot(\mathbf{X}_J-\mathbf{X}_I)W_I \tag{75}$$

At this point, it may be useful to note that there are appreciable differences in the calculation of the divergence of stress using peridynamics via (75) and the calculation of deformation gradient via (53). The most obvious difference is the fact that the divergence of stress is approximated by a summation over two added stress values at two different points multiplied by the inverse of the shape tensor at those points.

At first glance, it may seem unlikely that (75) would lead to the same approximation for the divergence of stress as the one obtained by RKPM with synchronized derivatives, but this is in fact what happens. Returning to the one-dimensional bar with uniformly spaced points and determining the divergence of stress at point 0,

$$\frac{\mathrm{d}\sigma_0}{\mathrm{d}X} = \sum_{J=1}^{M}\phi^a_{J^+}\left[(\sigma_{J^+})K^{-1}_{J^+} + (\sigma_0)K_0^{-1}\right](X_{J^+}-X_0)W + \sum_{J=1}^{M}\phi^a_{J^-}\left[(\sigma_{J^-})K^{-1}_{J^-} + (\sigma_0)K_0^{-1}\right](X_{J^-}-X_0)W \tag{76}$$

with $M=(Np-1)/2$, and $\phi^a{}_{J^+} = \phi^a{}_{J^-} = \phi_a(X_J-X_0)$.

This equation can be simplified similarly to what was done for the deformation gradient, since $X_{J^-}-X_0 = -J\Delta X$, $X_{J^+}-X_0 = J\Delta X$, and noting that the shape tensor has the same value at any point (uniform grid) as can be seen in (69), $K_{J^+} = K_{J^-} = K_0 = \sum_{J=1}^{M}(2J^2\phi^a_J)W\Delta X^2$:

$$\frac{\mathrm{d}\sigma_0}{\mathrm{d}X} = \sum_{J=1}^{M}\phi^a_J\left[(\sigma_{J^+}+\sigma_0)K_0^{-1} - (\sigma_{J^-}+\sigma_0)K_0^{-1}\right]JW\Delta X = \sum_{J=1}^{M}\left[J\phi^a_J(\sigma_{J^+}-\sigma_{J^-})W\Delta X\right]K_0^{-1} \tag{77}$$

And using (69) we can finally obtain

$$\frac{\mathrm{d}\sigma_0}{\mathrm{d}X} = \frac{\sum_{J=1}^{M}J\phi^a_J(\sigma_{J^+}-\sigma_{J^-})}{\sum_{J=1}^{M}(2J^2\phi^a_J)\Delta X}, \quad M=\frac{Np-1}{2} \tag{78}$$

which surprisingly is the same expression obtained for the deformation gradient in (57), replacing stress by current position, and therefore the same approximation is obtained via RKPM with synchronized derivatives. This result is surprising because the starting expression for the calculation of the divergence of stress using peridynamics uses two terms and includes the stress value at the point where the divergence is being calculated, in our example σ_0. However, this stress value ends up being canceled through the algebraic procedure and the resulting expression is only a function of the stress values in the remaining points. Once again, this result can be easily generalized to multiple dimensions, using uniform grids, as done in Bessa *et al.* (2014). The one-dimensional example is sufficiently illustrative of what happens with the peridynamic discretization and why there is an argument for including this method in the large family of meshfree methods using polynomial basis functions.

The equivalence between peridynamics and RKPM with synchronized derivatives for uniform grids clarifies that peridynamics can be seen as a subset of the RKPM approximation where several algebraic operations are reduced since the shape tensor is a submatrix of the moment tensor and there are no derivatives involved in the peridynamic procedure. Particularly relevant is the understanding of the consequences of finding this equivalence between these two meshfree methods: peridynamics can leverage upon

the significant progress achieved in the remaining meshfree methods, namely, in imposing boundary conditions and using nonuniform grids.

3.3 Additional considerations

There is not a complete equivalence between the discretizations of peridynamics and RKPM with synchronized derivatives for general cases. In fact, this equivalence breaks down for nonuniform grids and at the boundaries of the domain. In these situations, the RKPM approximation leads to more than one nonzero coefficient in the polynomial approximation (see, e.g., (67)), and the peridynamic approximation does not include those corrections.

In addition, since peridynamics can arguably be viewed as a subset of RKPM, it is evident that it also lacks the Kronecker Delta property, that is, the approximation to the function does not lead to the exact values of that function in the discretization points. This has well-known implications in the imposition of essential boundary conditions, as discussed in Section 6.

Important questions arise for nonuniform grids and the approximation obtained for the divergence of stress using peridynamics: it is evident that the equivalence does not hold for this case; so what is the meaning of the obtained approximation? More importantly, what are the different properties of these approximations? In particular, how fast is convergence and how does it compare with the other meshfree methods? There are also issues with stability of peridynamics, particularly in the strong form (as it is mostly used to date) that are shared with the remaining meshfree methods.

4 SOLVING THE FRACTIONAL ADVECTION–DIFFUSION EQUATION (FADE) BY THE REPRODUCING KERNEL PARTICLE METHOD

The idea of fractional derivative, a non-local operator, was conceived of in the discussion between L'Hôspital and Leibnitz in 1695 regarding the meaning of the half derivative of the function $f(x) = x$ (Loverro, 2004). After more than three centuries of development by mathematicians, fractional calculus gradually became an excellent instrument for the description of memory- and space-correlation properties of various materials and processes (Podlubny, 1998), such as polymers and anomalous diffusion. Consequently, PDEs including one or several fractional derivative-based terms are emerging as a powerful tool to model phenomena that are neglected by classical integer derivative-based PDEs since integer derivatives are local operators in the mathematical sense.

In the last few decades, a variety of temporal and/or spatial fractional PDEs (West, 2014; Rossikhin and Shitikova, 2010; Craiem and Magin, 2010) have been employed for modeling non-local processes, which are common to problems involving strong heterogeneity, fracticality, or statistical correlations, for example, turbulent flow and contaminant/solute transport in highly heterogeneous aquifers or porous media. Among this class of problems, the FADE is employed to describe the anomalous diffusion process, which is studied here using RKPM.

4.1 One-dimensional spatial fractional advection–diffusion equation (FADE)

Here, we focus on the following one-dimensional spatial FADE:

$$\frac{\partial\theta(x,t)}{\partial t} + \chi\frac{\partial\theta(x,t)}{\partial x} - \kappa\frac{\partial}{\partial x}\theta^{(\alpha)}(x,t) = f(x,t) \tag{79}$$

where θ represents the solute concentration, t stands for time, $f(x,t)$ is a source term, χ is the advective velocity, κ is a coefficient of the fractional diffusion term, and $\alpha \in (0,1]$ stands for the fractional derivative order associated with a left-sided Caputo fractional derivative. The left-sided Caputo fractional derivative is defined for a general function $u(x)$ as

$$u^{(\alpha)}(x) = \frac{1}{\Gamma(1-\alpha)}\int_0^x (x-y)^{-\alpha}\frac{\mathrm{d}}{\mathrm{d}y}u(y)\mathrm{d}y \tag{80}$$

where $\Gamma(1-\alpha) = \int_0^\infty z^{-\alpha}e^{-z}\mathrm{d}z$ is the Gamma function.

4.2 Fractional derivative of shape function of RKPM

For simplicity and demonstration purposes, let us assume a uniformly spaced grid where N_p nodes are evenly spaced by Δx. The position of node I is then $x_I = I\Delta x$ for $I = 0, \ldots, n-1$. By choosing a first-omial basis, support size $a = 2\Delta x$, and quartic spline kernel functions, the global internal node I has an RK shape function given by

$$\Psi_I(x) = \frac{5}{8}\begin{cases} 1 - 6r^2 + 8r^2 - 3r^4 & 0 < r < 1 \\ 0 & r \geq 1 \end{cases} \tag{81}$$

where $r = |x - x_I|/a$. From (80), the fractional derivative for the above shape function becomes:

$$\Psi_I^{(\alpha)}(x) = \frac{1}{\Gamma(1-\alpha)}\int_0^x (x-y)^{-\alpha}\frac{\mathrm{d}}{\mathrm{d}y}\Psi_I(y)\mathrm{d}y \tag{82}$$

Substituting (81) into (82) yields

$$\Psi_I^{(\alpha)}(x) = E(\alpha)\begin{cases} 0 & x \in [x_0 x_{I-2}] \\ H(x - x_{I-2}; x - x_I) & x \in [x_{I-2}, x_I] \\ H_m(x) + G(x - x_I; x - x_I) & x \in [x_I, x_{I+2}] \\ \quad -G(0; x - x_I) & \\ H_m(x) - G_m(x) & x \in [x_{I+2}, x_{Np-1}] \end{cases} \tag{83}$$

where

$$E(\alpha) = \frac{15}{2a^2\Gamma(2-\alpha)} \tag{84}$$

$$H_m(x) = H(x - x_{I-2}; x - x_I) - H(x - x_I; x - x_I) \tag{85}$$

$$G_m(x) = G(x - x_{I-2}; x - x_I) - G(x - x_I; x - x_I) \tag{86}$$

with

$$\begin{aligned} H(\eta;\xi) &= \xi\eta^{1-\alpha} + \frac{1-\alpha}{2-\alpha}\eta^{2-\alpha} \\ &\quad - \frac{1}{a^2}\left[\xi^2\eta^{1-\alpha} + \frac{2\xi(1-\alpha)}{2-\alpha}\eta^{2-\alpha} + \frac{1-\alpha}{3-\alpha}\eta^{3-\alpha}\right] \\ &\quad + \frac{1}{a^2}\left[\xi^3\eta^{1-\alpha} + \frac{3\xi^2(1-\alpha)}{2-\alpha}\eta^{2-\alpha} + \frac{3\xi(1-\alpha)}{3-\alpha}\eta^{3-\alpha}\right. \\ &\quad \left. + \frac{1-\alpha}{4-\alpha}\eta^{4-\alpha}\right] \end{aligned} \tag{87}$$

and

$$\begin{aligned} G(\eta;\xi) &= \xi\eta^{1-\alpha} + \frac{1-\alpha}{2-\alpha}\eta^{2-\alpha} \\ &\quad + \frac{1}{a^2}\left[\xi^2\eta^{1-\alpha} + \frac{2\xi(1-\alpha)}{2-\alpha}\eta^{2-\alpha} + \frac{1-\alpha}{3-\alpha}\eta^{3-\alpha}\right] \\ &\quad + \frac{1}{a^2}\left[\xi^3\eta^{1-\alpha} + \frac{3\xi^2(1-\alpha)}{2-\alpha}\eta^{2-\alpha} + \frac{3\xi(1-\alpha)}{3-\alpha}\eta^{3-\alpha}\right. \\ &\quad \left. + \frac{1-\alpha}{4-\alpha}\eta^{4-\alpha}\right] \end{aligned} \tag{88}$$

Figure 6 depicts the fractional derivative of the RK shape function $\Psi_I^{(\alpha)}(x)$ for selected values of $\alpha \in (0, 1]$ within a material domain $x \in [0, 1]$ with node spacing $\Delta x = 1$.

The approximation of (82) requires numerical integration. However, the presence of the kernel $(x-y)^{-\alpha}$ inside the integration of (82) can lead to numerical issues when using Gauss quadrature as $\alpha \to 1$. In order to avoid this, we recommend using an alternative formula of the Caputo definition, which can be derived by applying integration by parts to increase the order of the kernel by 1 as follows.

$$u^{(\alpha)}(x) = \frac{1}{\Gamma(2-\alpha)}\left[\frac{\mathrm{d}}{\mathrm{d}x}u(x)\bigg|_{x=0} x^{\alpha} - \int_0^x (x-y)^{1-\alpha}\frac{\mathrm{d}^2}{\mathrm{d}y^2}u(y)\mathrm{d}y\right] \tag{89}$$

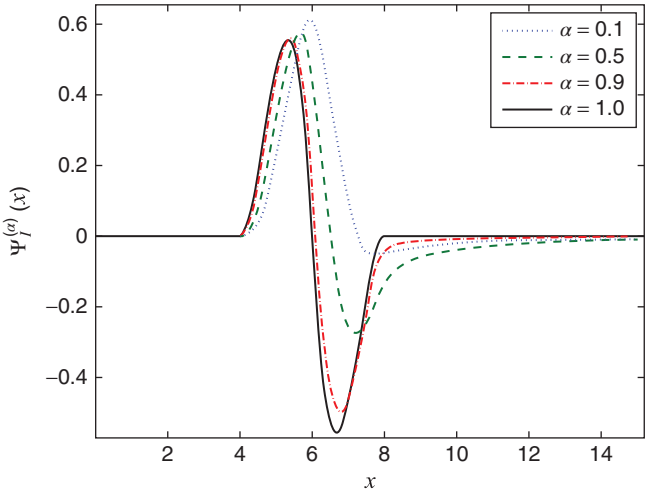

Figure 6. Non-locality of $\Psi_I^{(\alpha)}(x)$ with $\alpha = 0.1$, 0.5, and 0.9, where the support domain is extended to the right side of the domain, and can shrink back to compact domain for $\alpha = 1$, that is, the support domain is equal to that of the shape function.

4.3 Petrov–Galerkin-based RKPM for FADE

With the given essential boundary conditions, following standard procedures, a weak form of the spatial FADE reads

$$\begin{aligned} &\int_\Omega \tilde{v}\theta_{,t}(x,t)\mathrm{d}x + \int_\Omega \chi\tilde{v}\theta_{,x}(x,t)\mathrm{d}x + \int_\Omega \kappa v_{,x}\theta^{(\alpha)}(x,t)\mathrm{d}x \\ &\quad - \int_\Omega \omega\kappa v_{,x}\theta^{(1+\alpha)}(x,t)\mathrm{d}\Omega = \int_\Omega \tilde{v}f(x,t)\mathrm{d}x \end{aligned} \tag{90}$$

where $\tilde{v} = v + \omega v_{,x}$ is the test function, comma denotes an integer derivative, and ω is the viscosity coefficient. If ω is set as zero, then the Petrov–Galerkin-based RKPM reduces to the Galerkin-based RKPM. For notational simplicity, let $\theta^{(1+\alpha)}(x,t) = \partial\theta^{(\alpha)}(x)/\partial x$, and while the Lagrange multiplier method is used to impose essential boundary conditions, the associated terms are not included in the above equation. The corresponding discretization equation to (90) yields

$$\mathbf{M}\dot{\mathbf{\Theta}} + \left[\chi(\omega\mathbf{K}^*(1) - \mathbf{K}^*(0)) + \kappa\mathbf{K}^*(\alpha) - \omega\kappa\mathbf{K}^*(1+\alpha)\right]\mathbf{\Theta} = \mathbf{F} \tag{91}$$

where $M_{IJ} = \int_\Omega(\Psi_I + \omega\Psi_{I,x})\Psi_J\mathrm{d}x$, $\mathbf{\Theta} = \left[\theta_0 \cdots \theta_J \cdots\right]^T$ is the nodal value vector, $F_I = \int_\Omega[\Psi_I + \omega\Psi_{I,x}]f(x,t)\mathrm{d}x$, and

$$K_{IJ}^*(\alpha) = \int_\Omega \left[\Psi_{I,x}\Psi_J^{(\alpha)}\right] f(x,t)\mathrm{d}x \tag{92}$$

From the above, one should note that there are two basic issues associated with the fractional diffusion term. One is that the induced stiffness matrix is no longer compact, but

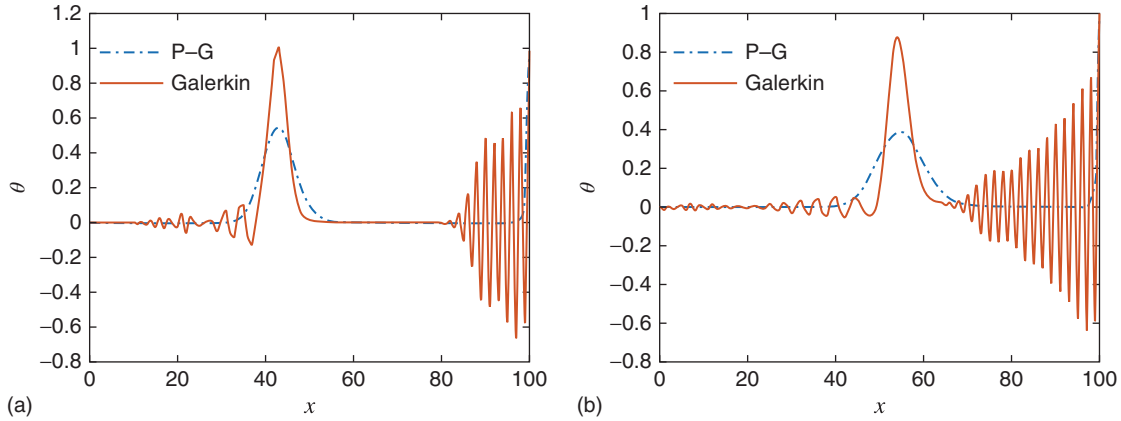

Figure 7. Numerical results for time-dependent advection–diffusion equation at time of (a) $t=1$, and (b) $t=2$.

dense, owing to the non-local fractional differential operator, which causes efficiency issues.

The other issue is how to determine the viscosity coefficient, since the formula based on FEM for integer derivative advection–diffusion equations is not the optimal one here as $0<\alpha<1$. As is well known (Hughes *et al.,* 1982), for an integer derivative order case, the viscosity parameter ω is determined by element size and Peclet number, $Pe=2\chi\Delta x/\kappa$. However, for the fractional derivative order case, Pe is no longer a dimensionless number because the dimension of κ takes the form $\Upsilon^{1+\alpha}/T$, where Υ and T are the length and time dimensions, respectively (Lian *et al.*, 2016.). Furthermore, the fractional diffusion term from FADE possesses not only a diffusion effect but also an advection effect, which is not taken into account by the traditional viscosity parameter formula (Lian *et al.*, 2016.). A suitable stabilization parameter formula, which can take into account both advection and fractional diffusion terms for Petrov–Galerkin-based FEM, is proposed in Lian *et al.* (2016.) as follows and is applied herein to Petrov–Galerkin-based RKPM:

$$\omega=\frac{(2^{3-\alpha}-8)\Theta+2-2\widehat{Pe}}{\left[(2-\alpha)(2^{1-\alpha}-4)+4\widehat{Pe}\right]\Theta+2-\alpha-2\widehat{Pe}}\frac{\Delta x}{2}$$

where $\widehat{Pe}=\Gamma(3-\alpha)\chi(\Delta x)^{\alpha}/2\kappa$ is fractional element Peclet number, $\Gamma(z)$ is Gamma function, $\Theta=(E_{\alpha,1}(2\widehat{Pe}/\Gamma(3-\alpha))-1)/(E_{\alpha,1}(2^{1+\alpha}\widehat{Pe}/\Gamma(3-\alpha))-1)$, and $E_{\alpha,1}(z)$ is two-index Mittag–Leffler function.

4.4 An illustrative example

Within a domain of $x\in[0,100]$, (79) is solved by the Petrov–Galerkin-based RKPM with essential boundary conditions

$$\theta(0,t)=0,\qquad \theta(100,t)=1 \tag{93}$$

the initial conditions

$$\theta(x,0)=\begin{cases}e^{-0.05(x-32.5)^2} & x\in[30,35]\\ 0 & \text{otherwise}\end{cases} \tag{94}$$

and source term $f(x,t)=0$.

The case of $\alpha=0.5$, $\chi=12$, $\kappa=1$, $\Delta x=1$, and $a=3\Delta x$ is studied, which results in $\widehat{Pe}=7.976$. Since $\widehat{Pe}$ is much larger than 1, we expect the Galerkin-based RKPM solution to contain spurious oscillations. A forward time integration method and lumped mass matrix scheme are employed. Numerical solutions from Petrov–Galerkin and Galerkin RKPM are shown in Figure 7(a) and (b) for times of $t=1$ and $t=2$, respectively. From the figure, it can be seen that the oscillations are not present in the results from the Petrov–Galerkin based RKPM.

5 MULTIPLE-SCALE REPRODUCING KERNEL APPROXIMATION

Multiple-scale RK approximation permits the response of a system to be separated into different scales (Liu and Chen, 1995; Liu *et al.,* 1996a,b, 1997a,b). These scales can be either the frequencies corresponding to temporal variables or the wave numbers corresponding to spatial variables, and each scale response can be examined separately. This complete characterization of the unknown response is performed through the integral window transform, and a space-scale and time-frequency localization process is obtained by dilating the flexible multiple-scale window function. This flexible space-scale window function can be constructed to resemble the *hp*-adaptive FEMs.

5.1 Brief review of multiresolution analysis

The multiple-scale RK approximation followed the concept of multiple scale wavelet particle method, which is based on multiresolution analysis (Liu and Chen, 1995). The framework of multiresolution analysis consists of a sequence of nested closed subspaces:

$$\{0\} = V_\infty \subset \cdots \subset V_1 \subset V_0 \subset V_{-1} \subset \cdots \subset V_{-\infty} = L^2(R) \tag{95}$$

These subspaces are generated by a series of scaling functions denoted by $\phi_{kl}(x)$, where k is the dilation parameter similar to the support dimension a, and l is the translation parameter. The scaling functions are generated from a single function $\phi(x)$, which is referred to as the mother function. Then these scaling functions are given by

$$\phi_{kl}(x) = 2^{-k/2}\phi\left(\frac{x}{2^k} - l\right) \quad k, l \in \Im = [\ \ldots\ , -1, 0, 1,\ \ldots\ ] \tag{96}$$

or in normalized form by

$$\phi_{kl}\left(\frac{x}{\Delta x}\right) = 2^{-k/2}\phi\left(\frac{x}{2^k \Delta x} - l\right) \tag{97}$$

An illustration of the translation and dilation parameters for a given mother function, in this case, the window function, is presented in Figure 8. The two parameters in the scaling function based on the mother function provide the ability to translate and dilate the window function. Translation is required to move the window function around the domain, since the window functions themselves have a compact support. The ability to translate replaces the need to define element. The dilation parameter is used to provide refinement. Therefore, the dilation parameter also controls the convergence rate of the multiple-scale RKPM. As shown in numerical examples in Liu *et al.* (1995b), the convergence rate of the L^2-norm (and H^1-norm) of a smooth Laplacian solution can vary from 2 to 16 (and from 1 to 15) for a Gaussian window function by simply changing the dilation parameter of the window function. This combination of translation and dilation produces a meshfree p-like adaptive variable node multiple-scale RKPM. Note that, the larger the dilation parameter, the smaller the frequency band in the solution and the larger the critical time step becomes in dynamic problems if an explicit time integration is adopted.

This idea can also be applied to the FEM. The shape function of the parent element acts as a kind of mother function, and then these scaling functions are given by the different element sizes, namely k, and the different nodes, l. Different resolution of solutions can be obtained by using different element sizes and correspondingly different total node numbers, which means the larger the dilation parameter, the coarser the mesh used in the simulation and hence smaller the frequency band in the solution and the larger the critical time step.

In order to show the decomposition of level k resolution clearly, we introduce the concept of complementary subspace, indicated by W_k. The complementary subspace is defined as the difference between V_k and its adjacent resolution, namely,

$$W_k = V_{k-1} - V_k \tag{98}$$

The complementary subspace W_k can be seen as an error measure between two adjacent resolutions from the corresponding subspaces.

Generally, a wavelet ψ is used to generate W_k in the same manner of the mother function $\phi(x)$ to the subspace V_k. Then

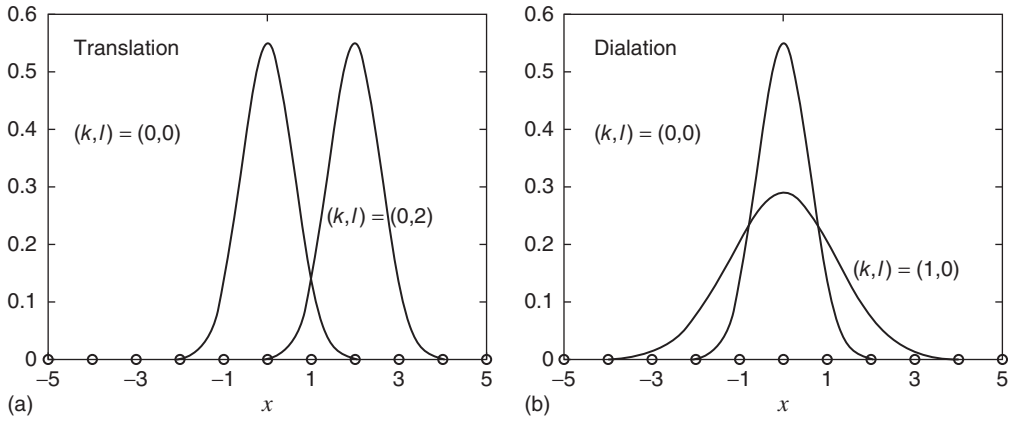

Figure 8. Examples of (a) translation and (b) dilation. (Reproduced with permission from Liu and Chen (1995). © John Wiley & Sons, 1995.)

the complementary subspace is given by

$$W_k = \{\psi_{kl}, l \in \mathfrak{I}\} \tag{99}$$

where this family of functions, denoted by $\psi_{kl}(x)$, is defined by

$$\psi_{kl}(x) = 2^{-k/2}\psi\left(\frac{x}{2^k\Delta x} - l\right) \quad k, l \in \mathfrak{I} \tag{100}$$

or in normalized form by

$$\psi_{kl}\left(\frac{x}{\Delta x}\right) = 2^{-k/2}\psi\left(\frac{x}{2^k\Delta x} - l\right) \quad k, l \in \mathfrak{I} \tag{101}$$

From (95) and (98), this family of subspaces of $L^2(R)$ gives a direct sum decomposition of $L^2(R)$, namely,

$$\begin{aligned} L^2(R) &= \cdots + (V_{-2} - V_{-1}) + (V_{-1} - V_0) + (V_0 - V_1) + \cdots \\ &= \cdots + W_{-1} + W_0 + W_1 + \cdots \end{aligned} \tag{102}$$

A wavelet ψ in $L^2(R)$ is called an orthogonal wavelet if $\{\psi_{kl}\}$ satisfies

$$\{\psi_{kl}, \psi_{ij}\} = \delta_{ki}\delta_{lj} \tag{103}$$

Based on the orthogonal scaling wavelet functions, (102) can become an orthogonal sum:

$$L^2(R) = \cdots \oplus W_{-1} \oplus W_0 \oplus W_1 + \cdots \tag{104}$$

Therefore, for any given function $u \in L^2(R)$, there exists a unique decomposition

$$u = \cdots + w_{-1} + w_0 + w_1 + \cdots \tag{105}$$

Then, the level k resolution can be given by

$$u \approx u_k = w_{k+1} + (w_{k+2} + w_{k+3} + \cdots) = w_{k+1} + u_{k+1} \tag{106}$$

where $u_{k+1} \in V_{k+1}$ and $w_{k+1} \in W_{k+1}$. By repeating this process, we get the decomposition algorithm from the finest scale to the arbitrary coarser scale as shown in Figure 9.

Based on the orthogonal scaling functions and wavelets, the reconstruction formula is given by Liu and Chen (1995)

$$u = \sum_{k,l \in \mathfrak{I}} \langle u, \psi_{kl}\rangle \psi_{kl}(x) \tag{107}$$

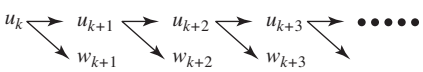

Figure 9. Multiresolution decomposition algorithm. (Reproduced with permission from Liu and Chen (1995). © John Wiley & Sons, 1995.)

For the level k^* resolution of the given function $u \in L^2(R)$, the reconstruction formula is

$$u_{k^*} = \sum_{l \in \mathfrak{I}} \langle u, \phi_{k^*l}\rangle \phi_{k^*l}(x) = \sum_{k=k^*}^{\infty} \sum_{l \in \mathfrak{I}} \langle u, \psi_{kl}\rangle \psi_{kl}(x) \tag{108}$$

5.2 Multiple scale wavelet particle method

Multiple-scale wavelet particle method is developed by taking the particle forms of wavelet analysis, namely, by breaking down the inner product terms of (107) into subinterval integration, say $B^k(l)$, and assuming that the response of $u(x)$ is constant in each of the subinterval, that is,

$$\langle u, \phi_{kl}\rangle = \sum_{I}^{x_i \in B^k(l)} \left(\int_{B^k(l)} \phi_{kl}(x)\mathrm{d}x\right) u_I \tag{109}$$

$$\langle u, \psi_{kl}\rangle = \sum_{I}^{x_i \in B^k(l)} \left(\int_{B^k(l)} \psi_{kl}(x)\mathrm{d}x\right) u_I \tag{110}$$

Furthermore, using a numerical quadrature integration scheme, one can obtain

$$\langle u, \phi_{kl}\rangle = \sum_{I}^{x_i \in B^k(l)} \phi_{kl}(x_I)\widehat{W}_I u_I \tag{111}$$

$$\langle u, \psi_{kl}\rangle = \sum_{I}^{x_i \in B^k(l)} \psi_{kl}(x_I)\widehat{W}_I u_I \tag{112}$$

where $B^k(l)$ is the support of the k-th scale window function at translation position l, and $\widehat{W}_I$ is the I-th nodal weight evaluated at x_I.

Substituting (109) and (110) into (107) and (108), and applying the decomposition algorithm given in Section 5.1, we have the following discrete multiresolution of $u(x)$ as

$$u \approx u_k = w_{k+1} + w_{k+2} + w_{k+3} + \cdots \tag{113}$$

where

$$u_k(x) = \sum_{I=1}^{Np} N_I^k(x) u_I \tag{114}$$

$$w_k(x) = \sum_{I=1}^{Np} \overline{N}_I^k(x) u_I \tag{115}$$

with

$$N_I^k(x) = \sum_{l=l_1}^{l_2} [\phi_{kl}(x_I)\widehat{W}_I]\phi_{kl}(x) \tag{116}$$

$$\overline{N}_I^k(x) = \sum_{l=l_1}^{l_2} [\psi_{kl}(x_I)\widehat{W}_I]\psi_{kl}(x) \tag{117}$$

Np is the total number of points used in the particle method, and l_1 and l_2 are the left and right limits of wavelet translation numbers, respectively.

For most cases, choosing $k=0$ in (97) and (101) can offer the best results (Liu and Chen, 1995). All the other coarser results can be derived automatically by the decomposition algorithm after getting the finest scale solutions.

5.3 Multiple-scale reproducing kernel approximation

It is straightforward to develop multiple-scale RK approximation following Section 5.2. The discrete form of RK approximation is given by

$$u^h(x) = \sum_{I=1}^{Np} \left[C(x; x - x_I; a)\phi\left(\frac{x - x_I}{a}\right)\widehat{W}_I \right] u(x_I) \tag{118}$$

Based on the study of Fourier transform (Liu *et al.*, 1996b), the kernel function can be viewed as a low-pass filter in the reconstruction procedure. Based on the analysis of the above section, the multiple-scale RK approximation can be defined by a family of kernel function $\phi_k(x)$, which is given by

$$\phi_k(x) = \phi\left(\frac{x}{2^k a}\right) \tag{119}$$

Their Fourier transform relationship with $\phi_0(x) = \phi(x/a)$ is obtained as

$$\widehat{\phi}_k(\xi) = \widehat{\phi}_0(2^k\xi) \tag{120}$$

The wavelets and its Fourier transform relationship corresponding to these kernel functions are given by

$$\psi_{k+1}(x) = \phi_k(x) - \phi_{k+1}(x) \tag{121}$$

$$\widehat{\psi}_{k+1}(\xi) = \widehat{\phi}_k(\xi) - \widehat{\phi}_{k+1}(\xi) \tag{122}$$

An example using a Gaussian function as the kernel function is shown in Figure 10.

Considering the multiple-scale wavelet particle method, the multiple-scale RKPM follows a similar method to get a series of different scale solutions from the finest scale to the arbitrary level of response by the decomposition algorithm:

$$\begin{aligned} u^h(x) &= u_0(x) && \text{(finest scale)} \\ &= u_1(x) + w_1(x) && \text{(two-level decompositon)} \\ &= u_2(x) + w_2(x) + w_1(x) && \text{(three-level decompositon)} \\ &= \cdots && \text{(up to arbitrary levels)} \end{aligned} \tag{123}$$

where

$$u_k(x) = \int_\Omega C(x; x - y; 2^k a)\phi_k(x - y)u(y)\mathrm{d}y \tag{124}$$

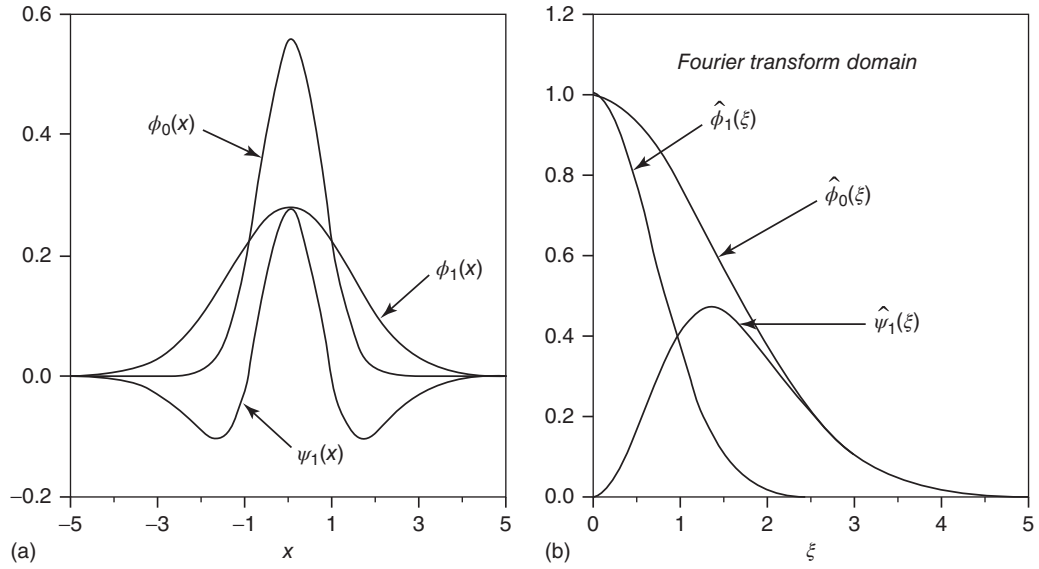

Figure 10. Kernel function and the corresponding wavelet function. (Reproduced with permission from Liu and Chen (1995). © John Wiley & Sons, 1995.)

$$w_k(x) = \int_\Omega \psi_k(x-y)u(y)\mathrm{d}y \tag{125}$$

$$\psi_k(x-y) = C(x;x-y;2^{k-1}a)\phi_{k-1}(x-y) - C(x;y;2^k a)\phi_k(x-y) \tag{126}$$

5.4 *hp*-like adaptivity

5.4.1 The optimal dilation parameter

A large window (large a) will filter out the finest scale and get an oscillation in the solution, caused by sampling aliasing. In contrast, a small window (small a) will cover wider scales but introduce aliasing. Then an energy error ratio parameter is introduced to determine the optimal dilation parameters. For more detailed information, readers may consult reference (Liu and Chen, 1995). For a given window function, the number of nodes covered under the support can be determined with the choice of optimal dilation parameters to yield the optimal rate of convergence as well as absolute accuracy.

5.4.2 hp-like adaptivity

Since the choice of an optimal dilation parameter of a given window function is analogous to choosing the optimal order of the polynomial (Liu *et al.*, 1995b), the multiple-scale RKPM has similar features of the adaptive p-finite element methods. Note that the advantage of multiple-scale RKPM is that there is no need to consider the compatibility issue as shown in the *hp*-finite element mesh. As for the h-like adaptivity, multiple-scale RKPM can achieve this by inserting nodes in the high gradient region and at the same time narrowing the size of the window function to pick up the fine-scale structure of the response.

Based on the multiple-scale decomposition, a convergence parameter or an error estimation indicator, say ε, can be defined as

$$\varepsilon = \int_\Omega \frac{\left|u_{\text{highscale}}\right|^2}{\left|u_{\text{totalscale}}\right|^2}\mathrm{d}\Omega \tag{127}$$

where $u_{\text{highscale}}$ is the highest band solution from the multiple-scale decomposition algorithm and $u_{\text{totalscale}}$ is the total solution. This indicator can be employed to locate the adaptivity regions.

It is further emphasized that the *hp*-finite element method requires the creation of an *hp*-mesh, and fabrication of low and higher order element shape functions so that the different order elements along element boundaries are compatible, whereas in the multiple-scale RKPM the *hp*-equivalent adaptive refinement is a built-in condition. The adaptive refinement is accomplished by a single p-order flexible space-scale window function that translates and dilates covering all the nodes in the computational domain. Furthermore, using the local error indicator, local refinement or *hp*-like adaptive refinement based on RKPM can be carried out without the exact solution.

6 SOLVING PDEs BY THE GALERKIN METHOD

6.1 Issues in domain integration: convergence and stability

An array of considerations come with the employment the Galerkin-based RK method, and in particular, domain integration needs careful attention. Meshfree shape functions are in general rational, and their overlapping supports may form complicated structures; the choice of quadrature affects the stability and convergence of the numerical solution because of these two issues (Chen *et al.*, 2001,2013; Beissel and Belytschko, 1996; Belytschko *et al.,* 2000). High-order quadrature can offer stability and optimal convergence, but it is prohibitively expensive for practical use. On the other hand, low-order quadrature consumes less CPU, but can yield non-convergent solutions, which can also be unstable in the case when integration is performed directly at the nodes (Chen *et al.*, 2001; Beissel and Belytschko, 1996; Belytschko *et al.*, 2000). Thus, alternative approaches must be taken in order to avoid these two issues.

Consider Poisson's equation as a model problem for the RKPM:

$$\begin{aligned} \nabla^2 u + Q &= 0 \quad \text{in } \Omega \\ \boldsymbol{\nabla} u \cdot \mathbf{n} &= h \quad \text{on } \partial\Omega_h \\ u &= g \quad \text{on } \partial\Omega_g \end{aligned} \tag{128}$$

where Q is a source term, g is the prescribed value of u on the essential boundary $\partial\Omega_g$, and h is the prescribed value on the natural boundary $\partial\Omega_h$.

Before moving on to the weak form, one must consider the fact that RK shape functions do not enjoy the Kronecker delta property, that is, $d_I \neq u^h(\mathbf{x}_I)$, and special techniques need to be introduced to enforce essential boundary conditions. These include methods that recover the Kronecker delta property such as the transformation methods (Chen *et al.*, 1996; Zhu and Atluri, 1998; Günther and Liu, 1998; Atluri *et al.*, 1999; Wagner and Liu, 2000; Chen and Wang, 2000), coupling with finite elements near the essential boundary (Krongauz and Belytschko, 1996; Fernández-Méndez and Huerta, 2004), and introducing modifications to the RK approximation near the essential boundary (Chen and Wang, 2000; Gosz and

Liu, 1996; Kaljevic and Saigal, 1997; Chen *et al.*, 2003). With the introduction of these methods, boundary conditions can be enforced in a manner analogous to FEMs. Alternatively, the penalty method (Zhu and Atluri, 1998; Atluri and Zhu, 1998), Nitsche's method (Nitsche, 1971; Griebel and Schweitzer, 2003; Babuška *et al.*, 2003), the modified variational principle (Lu *et al.*, 1994), or the Lagrange multiplier method (Belytschko *et al.*, 1994), can also be employed to enforce boundary conditions. Lagrange multipliers will be considered here for purposes of presentation.

The weak form of (128) requires finding $(u,\lambda)\in U\times\Lambda$ such that for all $(v,\gamma)\in V\times\Gamma$, with $U=V=[H^1(\Omega)]^d$ and $\Lambda=\Gamma=[L^2(\partial\Omega_g)]^d$, the following equation holds:

$$a(v,u)_\Omega=(v,Q)_\Omega+(v,h)_{\partial\Omega_h}+(v,\lambda)_{\partial\Omega_g}+(\gamma,u-g)_{\partial\Omega_g} \tag{129}$$

where $a(v,u)_\Omega=\int_\Omega\nabla v\cdot\nabla u\mathrm{d}\Omega$, $(\cdot,\cdot)_\Omega$ denotes the L^2 inner product of its two arguments in Ω, and $(\cdot,\cdot)_{\partial\Omega_g}$ and $(\cdot,\cdot)_{\partial\Omega_h}$ denote L^2 inner products of the two arguments on the essential and natural boundaries of Ω, respectively.

For finite-dimensional subspaces $U^h\subset U$, $V^h\subset V$, $\Lambda^h\subset\Lambda$, and $\Gamma^h\subset\Gamma$, the Galerkin statement of the problem (129) requires finding $(u^h,\lambda^h)\in U^h\times\Lambda^h$ such that for all $(v^h,\gamma^h)\in V^h\times\Gamma^h$ the following holds:

$$\begin{aligned}a(v^h,u^h)_\Omega=&\,(v^h,Q)_\Omega+(v^h,h)_{\partial\Omega_h}+(v^h,\lambda^h)_{\partial\Omega_g}\\&+(\gamma^h,u^h-g)_{\partial\Omega_g}\end{aligned} \tag{130}$$

where the test and trial functions are defined as

$$\begin{aligned}u^h=\sum_{I=1}^{Np}\widehat{\Psi}_I u_I,\quad v^h=\sum_{I=1}^{Np}\Psi_I v_I,\\ \lambda^h=\sum_{I=1}^{Nc}\widehat{\phi}_I\lambda_I,\quad \gamma^h=\sum_{I=1}^{Nc}\phi_I\gamma_I\end{aligned} \tag{131}$$

Here, Ψ_I is the RK shape function (36), $\widehat{\Psi}_I$ is a suitable test function approximation, ϕ_I and $\widehat{\phi}_I$ are suitable shape functions for the approximation of the Lagrange multiplier and its test function counterpart, respectively, and Nc is the number of functions employed for the enforcement of essential boundary conditions.

In practice, quadrature must be employed for the domain integration necessary to solve (130). The Galerkin equation (130) using numerical integration is

$$\begin{aligned}a\left\langle v^h,u^h\right\rangle_\Omega=&\left\langle v^h,Q\right\rangle_\Omega+\left\langle v^h,h\right\rangle_{\partial\Omega_h}+\left\langle v^h,\lambda^h\right\rangle_{\partial\Omega_g}\\&+\left\langle\gamma^h,u^h-g\right\rangle_{\partial\Omega_g}\end{aligned} \tag{132}$$

where $a\langle\cdot,\cdot\rangle_\Omega$ is the quadrature version of $a(\cdot,\cdot)_\Omega$, and $\langle\cdot,\cdot\rangle_\Omega$, $\langle\cdot,\cdot\rangle_{\partial\Omega_h}$, and $\langle\cdot,\cdot\rangle_{\partial\Omega_g}$ are the quadrature versions of $(\cdot,\cdot)_\Omega$, $(\cdot,\cdot)_{\partial\Omega_h}$, and $(\cdot,\cdot)_{\partial\Omega_g}$, respectively.

The approach taken to perform domain integration during the early development of Galerkin meshfree methods was to use GI using a background mesh (Liu *et al.*, 1995a; Belytschko *et al.,* 1994; Belytschko *et al.,* 1996; Chen *et al.,* 1996), as shown in Figure 11(a). There are a few disadvantages to this technique. First, since RK shape functions are rational, no matter how high the quadrature order, GI can only approximately satisfy the patch test (Dolbow and Belytschko, 1999). The order of quadrature required to guarantee optimal convergence is also high (Dolbow and Belytschko, 1999; Chen *et al.,* 2001, 2013), and it is prohibitively expensive in practical problems. Second, although RK approximations can be constructed by using a set of points without a mesh, domain integration using Gaussian quadrature still requires a mesh to construct the cells. It is, however, important to note that such a mesh can be generated independently of the nodal distribution.

The primary drawback of GI is the prohibitively expensive high-order quadrature required for solution accuracy. For example, for non-uniform node distributions, it has been shown that up to 5th-order GI in each cell is necessary to obtain optimal convergence rates (Chen *et al.*, 2013).

To illustrate, consider the following Poisson's equation on $\Omega:(-1,1)\times(-1,1)$:

$$\begin{aligned}\nabla^2u=-\sin(\pi x)\sin(\pi y)\ \text{ in }\ \Omega,\\ u=0\qquad\qquad\qquad\text{on }\ \partial\Omega\end{aligned} \tag{133}$$

The solution to this problem is $u=\sin(\pi x)\sin(\pi y)/2\pi^2$. The problem is solved using RKPM with linear basis and cubic B-spline kernel functions with normalized supports of 1.75. Here, the domain is first discretized with uniform nodal spacing h with integration cells of the same spacing, and then nodes are perturbed away from their original position, similar to the discretization in Figure 11(a). Refinement is then performed uniformly as shown in Figure 11(b), with integration cells also refined at the same rate. The convergence of the RKPM solution with GI and varying orders of quadrature q in each background cell is shown in Figure 11(c), where it is seen that convergence rates in the H^1 semi-norm are lower than the optimal rate of one, and even diverging solutions are observed for the case of 1×1 Gaussian quadrature. It can also be seen that 5×5 GI is necessary to obtain reasonable convergence rates with GI. It is possible, however, to achieve accuracy and optimal convergence with lower order quadrature under the framework of variational consistency (Chen *et al.,* 2013) as discussed in the following subsections.

Using the nodes themselves as integration points, as shown in Figure 12(a), is an attractive way to perform numerical

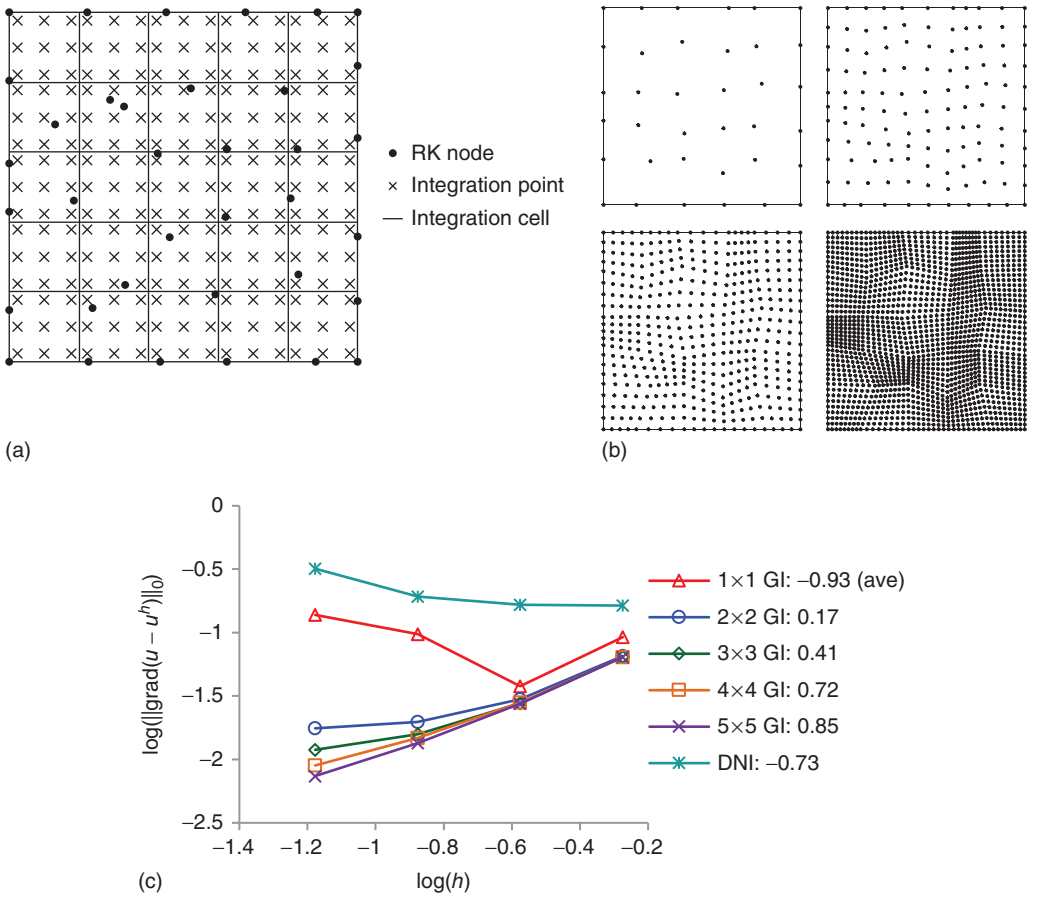

Figure 11. (a) Domain integration for RKPM using Gaussian integration; (b) refinements used in convergence study; (c) convergence of RKPM using q-order Gaussian integration "$q \times q$ GI", and direct nodal integration "DNI". (Reproduced with permission from Chen *et al.*, 2013. © John Wiley & Sons, 2013.)

integration due to its simplicity and efficiency, and it also avoids altogether using a background mesh and thus provides a truly meshfree method at the discrete level with quadrature. This method has been termed *direct nodal integration* (DNI) in the literature. This method, however, also fails to satisfy the patch test owing to the rational nature of the RK shape functions. In addition, this method constitutes low-order quadrature and does not attain optimal convergence rates in most situations (Chen *et al.,* 2001, 2013; Beissel and Belytschko, 1996). As seen in Figure 11(b), direct nodal integration can yield solutions that do not converge with refinement of the discretization. Again, the framework of variational consistency can be applied to nodal integration to rectify this situation, as discussed in the following subsections.

Apart from convergence, direct nodal integration also suffers from stability issues. Oscillating modes with wavelength twice the nodal spacing are admitted in the solution with little or no energy owing to the fact that the bilinear form is only sampled at the nodes, where this mode has zero gradient in the interior of the domain (Chen *et al.*, 2001; Beissel and Belytschko, 1996; Belytschko *et al.*, 2000). The node-to-node oscillations are clearly seen in Figure 12(b) for the solution of the problem (133) using direct nodal integration. Several techniques are available to alleviate the instability as discussed in Section 6.4.

To summarize, the following are the major issues associated with Gaussian and nodal integration:

1. Gaussian integration
   - Requires a background mesh
   - Does not pass the linear patch test even with linear completeness in the approximation
   - Higher order quadrature rules are needed for optimal convergence
2. Direct nodal integration

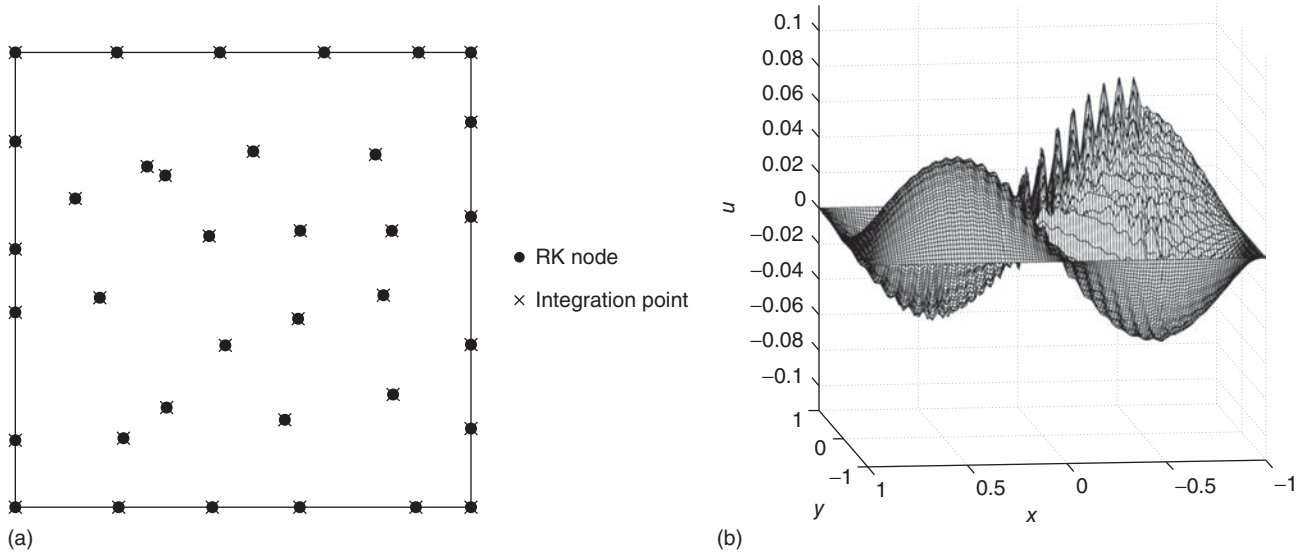

Figure 12. (a) Domain integration for RKPM using direct nodal integration; (b) instability in a solution obtained by direct nodal integration.

- Does not pass the linear patch test even with linear completeness in the approximation
- Derivatives of certain modes can vanish at nodes, which results in severe oscillations in the numerical solution
- Does not converge optimally

Over the past two decades, several techniques have been proposed to alleviate these problems. A summary of techniques is given in Table 1, which shows the order of approximation that can yield optimal convergence by using a given method, and the costs and considerations involved in achieving stability and convergence. Thus, one can observe in Table 1 why the stabilized conforming nodal integration (SCNI) method (Chen *et al.*, 2001) has been successful, as it yields optimal convergence without additional cost (over DNI), and yields stable solutions in most situations. The VCI method in conjunction with stabilized nodal integration (Hillman and Chen, 2016; Puso *et al.*, 2008; Hillman *et al.*, 2014) is a recent development, which also offers a promising technique where stable and convergent solutions are obtained using nodal integration, offering effectiveness and computational efficiency. The SCNI and stabilized nodal VCI methods are discussed in the following subsections.

6.2 Stabilized conforming nodal integration: first-order Galerkin exactness

It is possible to achieve optimal convergence with much lower order quadrature by achieving Galerkin exactness for a certain order solution. One particularly robust type of numerical integration that satisfies Galerkin exactness for linear solutions is the SCNI technique introduced in Chen *et al.* (2001), which does so by introducing a smoothed gradient framework with a built-in divergence operator.

Consider the problem (128) with a linear solution $u = \bar{u} \equiv a_0 + a_1 x + a_2 y$. The associated source term and boundary conditions for a problem with this solution are $Q = \overline{Q} \equiv \nabla^2 \overline{u} = 0$, $h = \overline{h} \equiv \nabla \overline{u} \cdot \mathbf{n} = a_1 n_1 + a_2 n_2$, and $g = \bar{u}$. The corresponding Galerkin equation with quadrature (132) for this problem is

$$a\left\langle v^h, u^h \right\rangle_\Omega = \left\langle v^h, \overline{h} \right\rangle_{\partial\Omega_h} + \left\langle v^h, \lambda^h \right\rangle_{\partial\Omega_g} + \left\langle \gamma^h, u^h - \overline{u} \right\rangle_{\partial\Omega_g} \tag{134}$$

Linear exactness requires that the above equation be satisfied with $u^h = \bar{u}$, and $\lambda^h = \overline{\lambda} \equiv \nabla \overline{u} \cdot \mathbf{n}$. In the context of solid mechanics, this requirement translates to equilibrium being satisfied with linear solutions on the discrete level with quadrature and that exact displacements are obtained, as well as exact tractions on the essential boundary.

In order for the approximation space to be able to represent the exact solution and the exact flux on the essential boundary, partition of nullity in the approximation of the Lagrange multiplier and linear completeness in the approximation of and their gradients must first be satisfied.

Taking $u_I = \bar{u}(\mathbf{x}_I)$ and $\lambda_I = \nabla \bar{u}(\mathbf{x}_I) \cdot \mathbf{n}(\mathbf{x}_I)$, and employing completeness of λ^h and u^h, one obtains $u^h = \bar{u}$, and $\lambda^h = \overline{\lambda} \equiv \nabla \overline{u} \cdot \mathbf{n}$. Using these values in (134), the condition for Galerkin linear exactness can be reduced to the following

Table 1. Comparison of integration techniques.

Method	Quadrature rule	Order of approximation with optimally convergent solutions	Stability	Associated cost
Low-order Gaussian quadrature	Gaussian quadrature	–	Possibly unstable	Negligible
High-order Gaussian quadrature	Gaussian quadrature	$n \geq 1$	Stable	Many evaluation points
Direct nodal integration	Nodal	–	Unstable	Negligible
Stress point (Dyka and Ingel, 1995)	Stress points	–	Stable in uniform node distributions	Additional evaluation points
Residual-based (Beissel and Belytschko, 1996)	Stabilized nodal	–	Stable in uniform node distributions	Higher order derivatives
Bounding-box (Dolbow and Belytschko, 1999)	Gauss	$n = 1$	Stable	Bounding box algorithm
Taylor expansion-based (Nagashima, 1999)	Stabilized nodal	–	Stable	Higher order derivatives
First-order exact with residual stabilization (Bonet and Kulasegaram, 2000)	Stabilized nodal	$n = 1$	Stable	Global-size iteration, high order derivatives
SCNI (Chen *et al.,* 2001)	Stabilized nodal	$n = 1$	Stable with low to moderate volume/surface ratio	Negligible
Particle PU method (Griebel and Schweitzer, 2002)	Sparse grid quadrature	$n \geq 1$	Stable	Cell-generating algorithm
M-SCNI (Puso *et al.,* 2008)	Stabilized nodal	$n = 1$	Stable	Additional evaluation points
Corrected quadrature (Babuška *et al.,* 2009)	Corrected weights	$n = 1$	Inherited from method corrected	Boundary integration
QC3 (Duan *et al.,* 2012)	Triangle mesh	$n = 2$	Stable	Additional evaluation points
VCI (Chen *et al.,* 2013)	Arbitrary	$n \geq 1$	Inherited from method corrected	Boundary integration
VC-MSCNI/VC-MSNNI (Hillman *et al.,* 2014)	Stabilized nodal	$n = 1$	Stable	Boundary integration, additional evaluation points
VC-NSNI (Hillman and Chen, 2016)	Stabilized nodal	$n = 1$	Stable	Boundary integration
Displacement smoothing (Wu *et al.,* 2015)	Stabilized nodal	$n = 1$	Stable	High order derivatives

divergence equality with quadrature (Chen *et al.,* 2001):

$$\int_{\Omega}^{\hat{}} \boldsymbol{\nabla} \widehat{\Psi}_I \mathrm{d}\Omega = \int_{\partial\Omega}^{\hat{}} \widehat{\Psi}_I \mathbf{n} \mathrm{d}\Gamma \tag{135}$$

where "^" over the integral sign denotes numerical integration. The above equation has been termed the *integration constraint* in the literature (Chen *et al.,* 2001). When the chosen numerical integration and approximation functions employed satisfy the integration constraint (135) and the completeness requirement, the exact linear solution is obtained using the Galerkin method for second-order PDEs.

In order to satisfy (135), stabilized conforming nodal integration with smoothed gradients of $\widehat{\Psi}_I$ (with $\widehat{\Psi}_I = \Psi_I$) over conforming nodal representative domains Ω_L (as shown in Figure 13(a)) is introduced as follows:

$$\begin{aligned} \tilde{\boldsymbol{\nabla}} \Psi_I(\mathbf{x}_L) &= \frac{1}{W_L} \int_{\Omega_L} \boldsymbol{\nabla} \Psi_I \mathrm{d}\Omega = \frac{1}{W_L} \int_{\partial\Omega_L} \Psi_I \mathbf{n} \mathrm{d}\Gamma \\ &\simeq \frac{1}{W_L} \int_{\partial\Omega_L}^{\hat{}} \Psi_I \mathbf{n} \mathrm{d}\Gamma \end{aligned} \tag{136}$$

where $W_L = \int_{\Omega_L} \mathrm{d}\Omega$. When the boundary integration for smoothing (136) and boundary integrals in (132) use the same quadrature rule, nodal integration with smoothed gradients $\tilde{\boldsymbol{\nabla}}$ meets the condition (135) if the smoothing domains $\{\Omega_L\}_{L=1}^{NP}$ are conforming (Chen *et al.,* 2001). It is sufficient to take one-point GI for the boundary faces in the

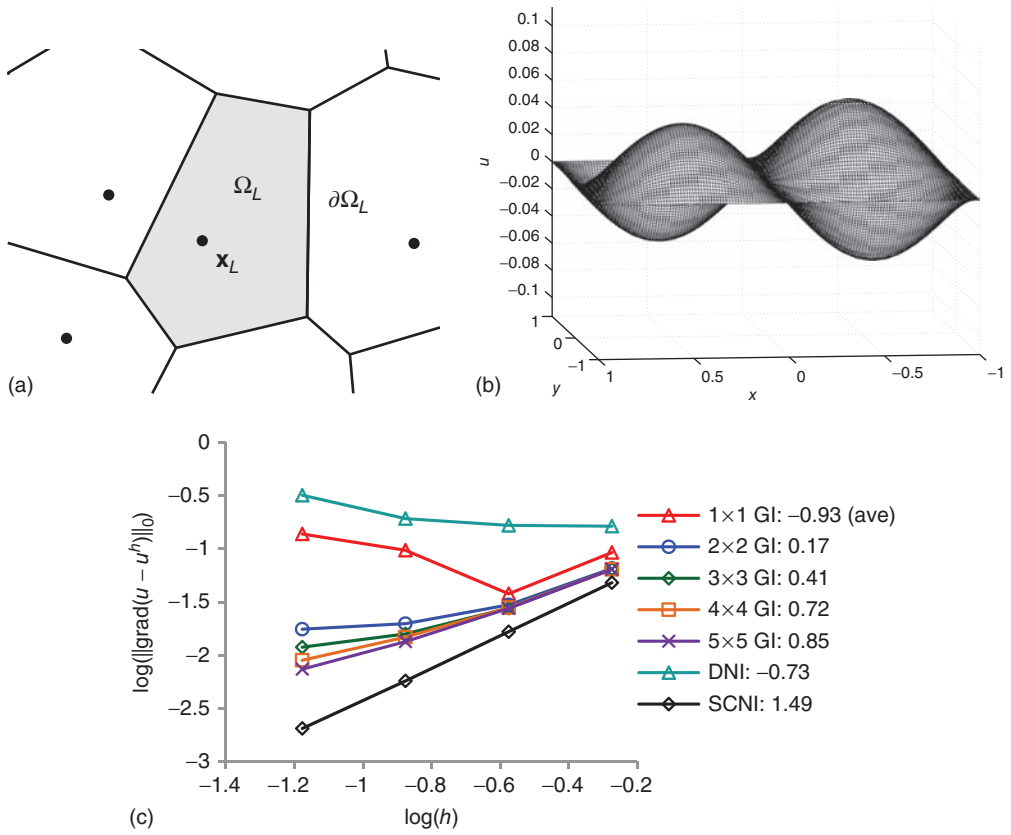

Figure 13. (a) Smoothing cells in stabilized conforming nodal integration; (b) solution to Poisson's equation with SCNI; (c) convergence of RKPM using q-order Gaussian integration "$q \times q$ GI", direct nodal integration "DNI", and stabilized conforming nodal integration "SCNI". ((c) Reproduced with permission from Chen *et al.*, 2013. © John Wiley & Sons, 2013.)

smoothing operation (136) to satisfy first-order consistency of the smoothed gradient (Chen *et al.,* 2013).

Because of the fact that first-order derivatives are not directly evaluated at the nodes, the instability due to zero energy modes in direct nodal integration is also precluded. Another key aspect of this method is that it results in an efficient quadrature scheme since nodal integration is employed and derivative computation of the RK shape functions is avoided. Hence, accuracy, stability, and efficiency are attained simultaneously using this method.

Consider again the problem (133) with linear RKPM and SCNI employed. As seen in Figure 13(b), the severe oscillations in solutions by direct nodal integration are also absent in the solution. Figure 13(c) shows the convergence of SCNI in (133), demonstrating that the optimal convergence rate of one in the H^1 semi-norm is achieved under the SCNI framework, performing far better than direct nodal integration, also using far fewer integration points than would be required with GI.

6.3 Variationally consistent integration: a generalization of SCNI for higher order Galerkin exactness

It is possible to generalize the integration constraint for linear exactness in second-order PDEs (135) to arbitrary order solutions and for general PDEs (Chen *et al.,* 2013). When these requirements are met, it is possible to achieve arbitrary order exactness and proper convergence rates associated with the approximations space using much lower order quadrature than would otherwise be required.

Consider the following boundary value problem:

$$\begin{aligned} Lu + Q &= 0 \quad \text{in } \Omega, \\ u &= g \quad \text{on } \partial\Omega_g, \\ Bu &= h \quad \text{on } \partial\Omega_h \end{aligned} \tag{137}$$

In the above, L is a differential operator acting in the domain, Q is a source term, g is the prescribed values of u

on the essential boundary $\partial\Omega_g$, and B is a boundary operator acting on the natural boundary $\partial\Omega_h$.

Consider the boundary value problem (137) where the solution is complete monomials with degree n: $u = \sum_{0\le i+j+k\le n} c_{ijk} x_1^i x_2^j x_3^k \equiv u^n$. When the boundary conditions and source term are prescribed as $Q = -Lu^n$ in Ω, $g = u^n$ on $\partial\Omega_g$, and $h = Bu^n$ on $\partial\Omega_h$, the solution to the problem (137) is u^n. With quadrature, the Galerkin approximation of this problem seeks $(u^h, \lambda^h) \in U^h \times \Lambda^h$ such that for all $(v^h, \gamma^h) \in V^h \times \Gamma^h$ the following equation holds:

$$a\left\langle v^h, u^h\right\rangle_\Omega = -\left\langle v^h, Lu^n\right\rangle_\Omega + \left\langle v^h, Bu^n\right\rangle_{\partial\Omega_h} + \left\langle v^h, \lambda^h\right\rangle_{\partial\Omega_g} + \left\langle \gamma^h, u^h - u^n\right\rangle_{\partial\Omega_g} \tag{138}$$

In order to obtain the exact solution u^n to this problem, it has been shown in Chen *et al.* (2013) that the trial functions Ψ_I and ϕ_I for u and λ, respectively, must satisfy the following completeness conditions:

$$\sum_{I=1}^{Np} \Psi_I u_I^n = u^n$$
$$\sum_{I=1}^{Nc} \phi_I \lambda_I^n = \lambda^n \tag{139}$$

where $u_I^n = \sum_{0\le i+j+k\le n} c_{ijk} x_{1I}^i x_{2I}^j x_{3I}^k$, $\lambda_I^n = \sum_{0\le i+j+k\le n} c_{ijk} (B x_1^i x_2^j x_3^k)_I$, and $\lambda^n = \sum_{0\le i+j+k\le n} c_{ijk} B x_1^i x_2^j x_3^k$. Setting $u_I = u_I^n$ and $\lambda_I = \lambda_I^n$ in (138) and employing completeness, it can be shown that the test functions must satisfy the following conditions:

$$a\left\langle \widehat{\Psi}_I, x_1^i x_2^j x_3^k\right\rangle_\Omega = -\left\langle \widehat{\Psi}_I, Lx_1^i x_2^j x_3^k\right\rangle_\Omega + \left\langle \widehat{\Psi}_I, Bx_1^i x_2^j x_3^k\right\rangle_{\partial\Omega} \quad \forall I, \quad 0 \le i+j+k \le n \tag{140}$$

where $\langle\cdot,\cdot\rangle_{\partial\Omega}$ is the quadrature version of the L^2 inner product on the boundary $(\cdot,\cdot)_{\partial\Omega}$.The equations in (140) are a generalization of the linear integration constraints (135) to arbitrary order, which have been termed the *variational consistency conditions*, and methods with domain integration and test spaces that are compatible in the form of (140) have been termed *variationally consistent integration* (VCI) (Chen *et al.,* 2013).

Remark 1.

1. To arrive at the n integration constraints in (140), nth pleteness in the trial functions has been used. The integration constraint states that the numerical integration of the domain and boundary integrals for Galerkin approximation of a PDE with differential operator L has to be consistent with the test functions $\widehat{\Psi}_I$ in the form of (140) for an nth plete numerical method to achieve the n exactness in the Galerkin approximation (passing the n patch test).
2. For $n = 1$, (140) is the integration constraint for linear solutions (135), which reduces to a divergence condition for a second order differential operator L such as in elasticity or Poisson's equation. Further, stabilized conforming nodal integration introduced in Chen *et al.* (2001) meets the constraint for $n = 1$.
3. In general, the constraint for constant exactness is automatically satisfied when the trial functions possess the partition of unity property.
4. The integration constraints in (140) act on the test functions $\widehat{\Psi}_I$. It is therefore possible, for a given set of nth plete trial functions, to construct test functions, different from the trial functions, to meet the integration constraints.

For Poisson's equation, the integration constraints are obtained as

$$a\left\langle \widehat{\Psi}_I, x_1^i x_2^j x_3^k\right\rangle_\Omega = -\left\langle \widehat{\Psi}_I, \nabla^2 x_1^i x_2^j x_3^k\right\rangle_\Omega + \left\langle \widehat{\Psi}_I, \boldsymbol{\nabla} x_1^i x_2^j x_3^k \cdot \mathbf{n}\right\rangle_{\partial\Omega} \forall I, \quad 0 \le i+j+k \le n \tag{141}$$

When $i+j+k=1$, the linear constraints (135) are recovered. The additional integration constraints are obtained by examining the cases of $i+j+k>1$.

For elasticity, the integration constraints can be obtained as:

$$\int_\Omega \hat{\boldsymbol{\nabla}}\, \widehat{\Psi}_I \cdot \boldsymbol{\nabla}^s x_1^i x_2^j x_3^k \mathrm{d}\Omega = -\int_\Omega \hat{\widehat{\Psi}}_I \boldsymbol{\nabla} \cdot \boldsymbol{\nabla}^s x_1^i x_2^j x_3^k \mathrm{d}\Omega + \int_{\partial\Omega} \hat{\widehat{\Psi}}_I \boldsymbol{\nabla}^s x_1^i x_2^j x_3^k \cdot \mathbf{n} \mathrm{d}\Gamma \quad \forall I, \quad 0 \le i+j+k \le n \tag{142}$$

Letting $i+j+k=1$, the linear constraints (135) are again recovered, while the higher order constraints can be obtained by setting $i+j+k>1$.

In order to satisfy n exactness, completeness of the trial functions must be satisfied, and the integration constraints (140) must be satisfied for the test functions. Completeness of the trial space can be met using the RK shape functions given in (36). Here the procedure introduced in Chen *et al.* (2013) to select a set of test functions to meet the integration constraints is presented.

Let the approximations of trial and test functions be expressed as:

$$u^h = \sum_{I=1}^{Np} \Psi_I u_I$$
$$v^h = \sum_{I=1}^{Np} \widehat{\Psi}_I v_I \tag{143}$$

where Ψ_I is the trial function approximation with nth pleteness, and the test functions are constructed as (Chen *et al.,* 2013):

$$\widehat{\Psi}_I = \Psi_I + \sum_{0\le|\alpha|\le n} \xi_{\alpha I} \widehat{\Psi}_I^{\alpha} \tag{144}$$

where $\{\Psi_I, \widehat{\Psi}_I^{\alpha}\}_{0\le|\alpha|\le n}$ are linearly independent, $\alpha \equiv (p,q,r)$, and $|\alpha| \equiv p+q+r$. Inserting the test functions into the integration constraint (140) yields a system of equations

$$\sum_{0\le|\alpha|\le n}^{n} A_{ijk\alpha}\xi_{\alpha I} = r_{ijkI}, \quad 0 \le i+j+k \le n \tag{145}$$

where

$$A_{ijk\alpha} = a\left\langle \widehat{\Psi}_I^{\alpha}, x_1^i x_2^j x_3^k \right\rangle_{\Omega} + \left\langle \widehat{\Psi}_I^{\alpha}, Lx_1^i x_2^j x_3^k \right\rangle_{\Omega} - \left\langle \widehat{\Psi}_I^{\alpha}, Bx_1^i x_2^j x_3^k \right\rangle_{\partial\Omega}$$
$$r_{ijkI} = -\left(a\left\langle \Psi_I, x_1^i x_2^j x_3^k \right\rangle_{\Omega} + \left\langle \Psi_I, Lx_1^i x_2^j x_3^k \right\rangle_{\Omega} - \left\langle \Psi_I, Bx_1^i x_2^j x_3^k \right\rangle_{\partial\Omega}\right) \tag{146}$$

The unknown coefficients $\xi_{\alpha I}$ are straightforwardly obtained from (145).

Remark 2.

1. The method resulting from the chosen integration method with the test function formed using (144)–(146) is variationally consistent.
2. The type of numerical integration is unspecified, and the framework allows construction of test functions consistent with any of the types of numerical integration.
3. The correction is driven by the residual of the constraints; for a method such as stabilized conforming nodal integration that is first order variationally consistent, no correction is needed for the first-order scheme.
4. In Chen *et al.* (2013) it was shown that using VCI, much lower order quadrature could be used to obtain optimal convergence than would otherwise be required.

To achieve computational efficiency, assumed strains can be introduced in order to satisfy (140). The test and trial functions are approximated by the shape functions with desired order of completeness, while direct and assumed gradients are then introduced for the trial and test functions, respectively, as follows:

$$u_{,i}^h = \sum_{I=1}^{Np} \Psi_{I,i} u_I$$
$$v_{,i}^h = \sum_{I=1}^{Np} \left(\Psi_{I,i} + \sum_{0\le|\alpha|\le n} \xi_{\alpha Ii} \widehat{\Psi}_{Ii}^{\alpha}\right) v_I \tag{147}$$

where $(\cdot)_{,i} \equiv \partial(\cdot)/\partial x_i$. The coefficients $\xi_{\alpha Ii}$ are again obtained by substitution of the approximation functions into the integration constraints.

Consider RKPM with linear basis for solving the problem (133), using several methods with and without VCI corrections (with corrected methods denoted with the prefix "VC-"): GI with varying orders of quadrature, DNI, SCNI, and also the variationally inconsistent, non-conforming version of SCNI, stabilized non-conforming nodal integration (SNNI) (Guan *et al.,* 2009, 2011). It can be seen in Figure 14 that optimal convergence can be achieved with 2×2 VC-GI, while in contrast 5×5 is necessary for variationally inconsistent GI. It can also be seen that variationally inconsistent nodal integration DNI and SNNI can be corrected to achieve near optimal and optimal convergence, respectively. The lack of optimal convergence in DNI is likely due to the numerical instability in the method, which can be remedied by procedures given in the next subsection.

6.4 Stabilization of nodal integration

The instability in direct nodal integration is due to the fact that for discretizations with spacing h, oscillating modes of wavelength $2h$ are admitted in the solution with little or no energy due to gradients being sampled only at the nodes (Chen *et al.,* 2001; Beissel and Belytschko, 1996; Belytschko *et al.,* 2000). Least-squares stabilization (Bonet and Kulasegaram, 2000; Beissel and Belytschko, 1996) and Taylor series expansions (Nagashima, 1999; Liu *et al.,* 2007) alleviate the instability by including second-order derivatives that are non-zero at nodes, and stress points (Randles and Libersky, 2000; Dyka *et al.,* 1997) provide sampling points at locations other than the nodes themselves.

Stabilized conforming nodal integration, where derivatives are not directly evaluated at nodes, circumvents the zero-energy instability (rank instability) without the use of any derivatives or additional sampling points. However, low-energy oscillatory modes exist in SCNI when the surface area to volume ratio is sufficiently small, or when the discretization is sufficiently fine (Puso *et al.,* 2008). Short-wavelength modes associated with only a small amount of energy from the boundary may become excited.

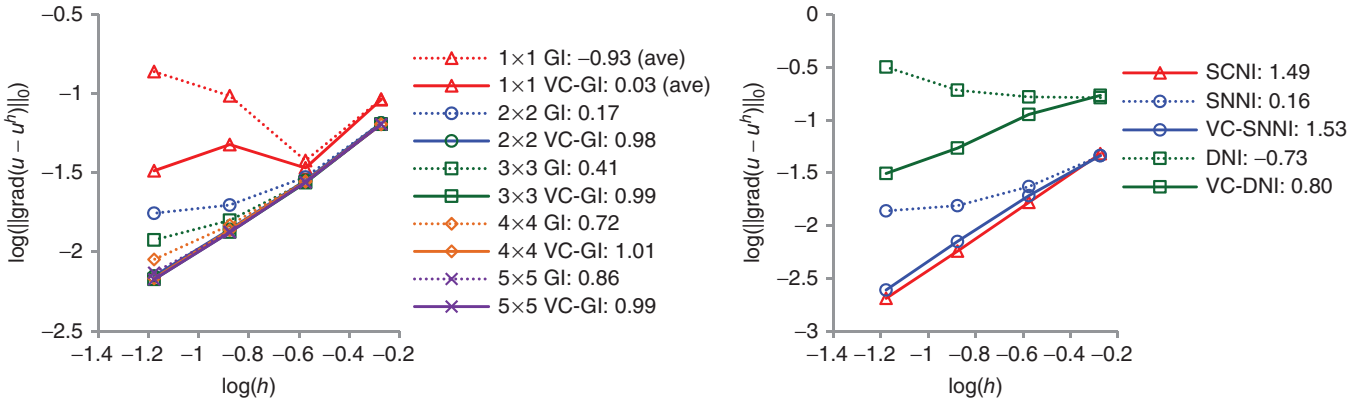

Figure 14. Convergence of various domain integration methods with and without VCI. (Reproduced with permission from Chen *et al.*, 2013. © John Wiley & Sons, 2013.)

With limited boundary influence of the discretization at hand, that is, when the surface to volume ratio is small, or for sufficiently fine discretizations, the instability in several nodal integration methods can be examined in a unified manner as follows.

Consider the calculation of a gradient in a one-dimensional Poisson equation by nodal integration. For an interior node (with no influence from the boundary), consider m nodes covering the nodal location x_L on each side of the node, giving a total of $2m+1$ nodes covering the location. A gradient is computed at this node as

$$u^h_{,x}(x_L) = \Psi_{L-m,x}(x_L)u_{L-m} + \cdots + \Psi_{L,x}(x_L)u_L + \cdots + \Psi_{L+m,x}(x_L)u_{L+m} \tag{148}$$

When sufficiently smooth (at least C^1) symmetric kernels are employed, the term $\Psi_{L,x}(x_L)$ can be shown to be zero when computed directly, and also when using averaging and smoothing operations when computing gradients. The remaining terms, using the uniformity and symmetry of the discretization, are

$$u^h_{,x}(x_L) = 2\Psi_{L-m,x}(x_L)(u_{L-m} - u_{L+m}) + 2\Psi_{L-m+1,x}(x_L)(u_{L-m+1} - u_{L+m-1}) + \cdots + 2\Psi_{L-1,x}(x_L)(u_{L-1} - u_{L+1}) \tag{149}$$

For modes of alternating displacement of unity at each node $u_{L-p} = u_{L+p}$ for any integer p, the gradient is identically zero, which is the essential difficulty of under-sampling using only nodes.

Consider the discretization shown in Figure 15(a) with SCNI employed for numerical integration. Eigenvalue analysis of the stiffness matrix for 2D elasticity reveals that the lowest non-zero energy modes are oscillatory, as seen in Figure 15(b).

The stabilization of these low-energy modes in SCNI can be accomplished by including gradient averaging with subdivisions of the smoothing cells (Puso *et al.,* 2008). Gradients evaluated directly at the centroid of (or smoothed over) *NS* subcells are employed in the stabilization in Puso *et al.* (2007, 2008); Chen *et al.* (2007), in order to provide additional coercivity and avoid under-sampling of the saw-tooth modes. Let S_L denote the set of stabilization points associated with point $\mathbf{x}_L$. The form of stabilization proposed in (Puso *et al.,* 2008) is based on maintaining satisfaction of the linear patch test in SCNI:

$$a\left\langle v^h, u^h\right\rangle = \sum_{L=1}^{Np}\left\{\tilde{\nabla}v^h(\mathbf{x}_L)\cdot\tilde{\nabla}u^h(\mathbf{x}_L)W_L + \sum_{L=1}^{NP}\sum_{K\in S_L} c\left[\left(\tilde{\nabla}v^h(\mathbf{x}_L) - \nabla v^h(\mathbf{x}_L^K)\right)\cdot\left(\tilde{\nabla}u^h(\mathbf{x}_L) - \nabla u^h(\mathbf{x}_L^K)\right)W_L^K\right]\right\} \tag{150}$$

where $\tilde{\nabla}u^h(\mathbf{x}_L)$ is the smoothed gradient at node L, $\nabla v^h(\mathbf{x}_L^K)$ is the direct (or alternatively, smoothed) gradient evaluated at the centroid $\mathbf{x}_L^K$ of the K^{th} subcell, c is a stabilization parameter ranging from zero to unity, and W_L^K is the cell weight associated to the K^{th} point in the set S_L. The first term in (150) is stabilized conforming nodal integration, while the second term stabilizes the solution. The distribution of stabilization points in relation to node L is depicted in Figure 16. SCNI with the additional stabilization in (150) has been termed modified stabilized conforming nodal integration (MSCNI).

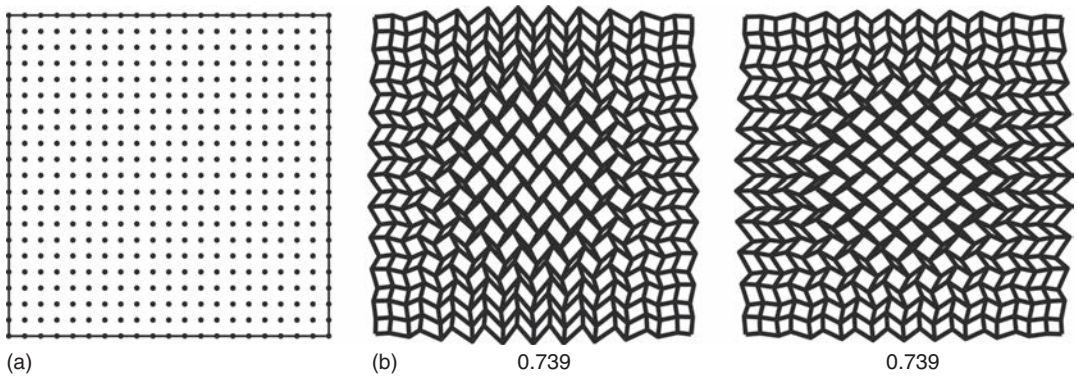

Figure 15. (a) Discretization, (b) lowest energy modes and eigenvalues of SCNI (two modes) (Hillman *et al.,* 2014). (Reproduced from M. Hillman, J.-S. Chen, S.-W. Chi, Stabilized and variationally consistent nodal integration for meshfree modeling of impact problems, *Comp. Part. Mech.* **1** (2014) 245–256. With permission of Springer.)

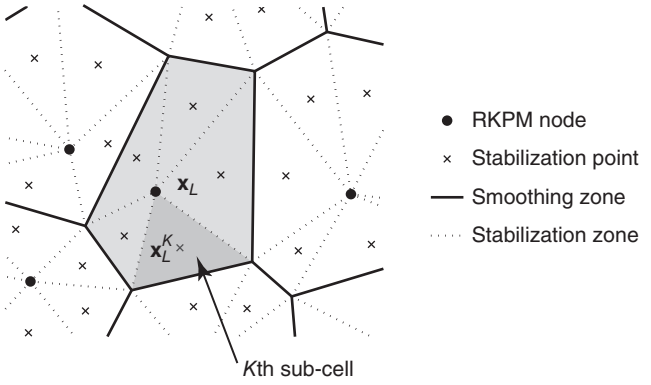

Figure 16. Scheme for the additional stabilization in MSCNI.

An eigenvalue analysis is performed on the stiffness matrices associated with the discretization in Figure 15(a) using the additional stabilization (150) with $c = 0.1$. The lowest energy mode is now a stable mode of deformation, which matches fully integrated linear FEM, as seen in Figure 17(a,b). The associated eigenvalues also match the one obtained by FEM. Figure 17(c) demonstrates that the additional stabilization does not degrade the convergence rate of SCNI as it maintains optimal convergence when solving Poisson's equation (133).

As an alternative to additional sampling points, which could become expensive in certain situations, a Taylor-series-type stabilization for RKPM with nodal integration can be obtained by following the procedures for unified stabilization in finite elements (Liu *et al.,* 1985) in Cartesian coordinates:

$$a\langle v^h, u^h\rangle = \sum_{L=1}^{NP} \{\nabla v^h(\mathbf{x}_L)\cdot\nabla u^h(\mathbf{x}_L)W_L + \nabla v^h_{,x}(\mathbf{x}_L) \cdot \nabla u^h_{,x}(\mathbf{x}_L)M_{Lx} + \nabla v^h_{,y}(\mathbf{x}_L)\cdot\nabla u^h_{,y}(\mathbf{x}_L)M_{Ly}\} \quad (151)$$

where

$$M_{Lx} = \int_{\Omega_L} (x - x_L)^2 \mathrm{d}\Omega,$$
$$M_{Ly} = \int_{\Omega_L} (y - y_L)^2 \mathrm{d}\Omega \quad (152)$$

To avoid the expense of evaluating high-order derivatives, derivative approximations can be directly constructed by employing implicit gradients (Chi *et al.,* 2013; Chen *et al.*, 2004):

$$\nabla u^h_{,x}(\mathbf{x}_L) \simeq \nabla \overline{u}^h_x(\mathbf{x}_L) = \sum_{I=1}^{NP} \nabla \overline{\Psi}^{10}_I(\mathbf{x}_L) u_I$$
$$\nabla u^h_{,y}(\mathbf{x}_L) \simeq \nabla \overline{u}^h_y(\mathbf{x}_L) = \sum_{I=1}^{NP} \nabla \overline{\Psi}^{01}_I(\mathbf{x}_L) u_I \quad (153)$$

where $\overline{\Psi}^{10}_I$ and $\overline{\Psi}^{01}_I$ are two-dimensional versions of the implicit gradients in (46). The resulting stabilization (151) with (153) is

$$a\langle v^h, u^h\rangle = \sum_{L=1}^{NP} \{\nabla v^h(\mathbf{x}_L)\cdot\nabla u^h(\mathbf{x}_L)W_L + \nabla \overline{v}^h_x(\mathbf{x}_L) \cdot \nabla \overline{u}^h_x(\mathbf{x}_L)M_{Lx} + \nabla \overline{v}^h_y(\mathbf{x}_L)\cdot\nabla \overline{u}^h_y(\mathbf{x}_L)M_{Ly}\} \quad (154)$$

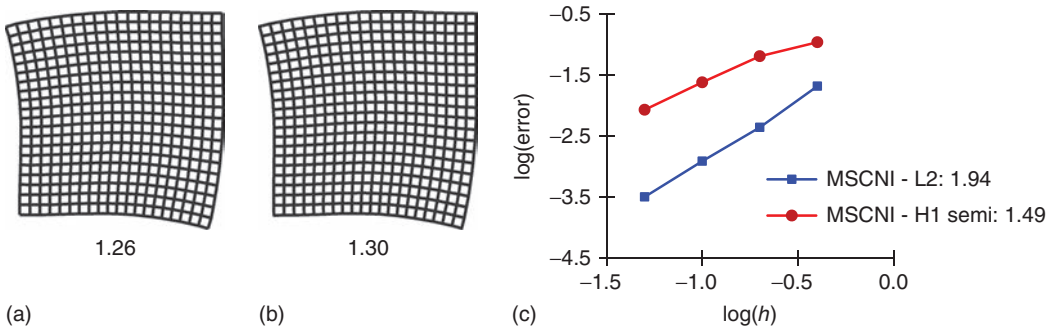

Figure 17. Lowest energy modes and eigenvalues of (a) modified SCNI (M-SCNI) and (b) fully integrated FEM (Hillman *et al.,* 2014); (c) convergence of M-SCNI in the Poisson's equation (133). ((a,b) Reproduced from M. Hillman, J.-S. Chen, S.-W. Chi, Stabilized and variationally consistent nodal integration for meshfree modeling of impact problems, *Comp. Part. Mech.* **1** (2014) 245–256. With permission of Springer.)

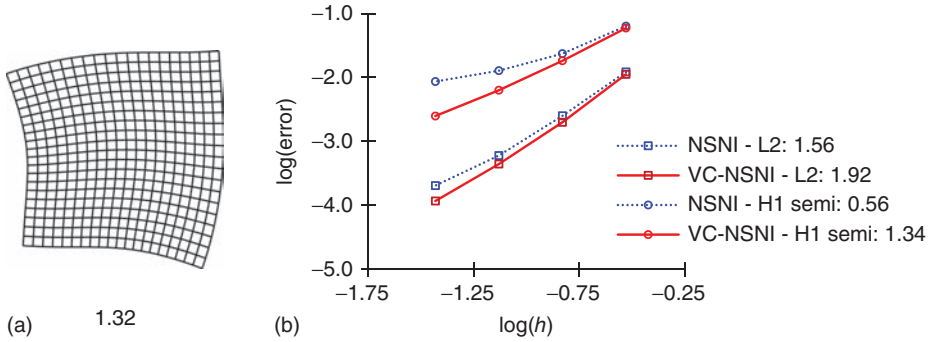

Figure 18. (a) Lowest energy mode of naturally stabilized nodal integration with associated eigenvalue (Hillman and Chen, 2016). (Reproduced with permission from Hillman and Chen (2016). © John Wiley & Sons, 2016.) (b) convergence of naturally stabilized nodal integration in convergence in Poisson's equation (133).

The additional two terms of the stabilization are positive for non-zero gradients and thus provide coercivity (Hillman and Chen, 2016). The constants associated with the additional terms occur naturally, and no tuning of any parameters is required. Stabilization with (154) is termed *naturally stabilized nodal integration* (*NSNI*) (Hillman and Chen, 2016).

One can observe that the construction of $\overline{\Psi}_I^{ij}$ by (46), necessary for (154), has the same complexity as the original RK approximation (36), and the resulting computational cost of the stabilization is similar to direct nodal integration, offering a stabilization with significant efficiency.

NSNI by itself is not variationally consistent and does not attain optimal convergence (Hillman and Chen, 2016). However, the method is well suited for the VCI technique and can be formulated to attain optimal convergence, with the resulting method termed VC-NSNI; see (Hillman and Chen, 2016) for details. Figure 18(a) shows the fourth eigenvalue mode of the previously employed RK discretization for eigenvalue analysis using VC-NSNI, which shows very good agreement with the mode shape of FEM in Figure 17(b), with the corresponding eigenvalue also in agreement with the value of 1.30 for fully integrated FEM. Figure 18(b) demonstrates that the method can attain optimal convergence under the VCI framework.

7 SOLVING PDES BY THE COLLOCATION METHOD

7.1 Introduction of collocation method

An alternative approach to circumvent domain integration issues in meshfree methods is by collocation of strong forms, such as the finite point method (Oñate *et al.,* 1996), the RBCMs (Kansa, 1990a,b), and the RKCM (Aluru, 2000; Hu *et al.,* 2011). Consider the application of strong form collocation to a boundary value problem as follows.

Let the approximation of $\mathbf{u}$ be expressed a s

$$\mathbf{u}^h(\mathbf{x}) = \sum_{I=1}^{N_S} g_I(\mathbf{x})\mathbf{u}_I \tag{155}$$

where N_S is the number of source points of set $Z = [\mathbf{x}_1, \mathbf{x}_2, \cdots \mathbf{x}_{N_S} | \mathbf{x}_I \in \overline{\Omega}]$ in the terminology of collocation methods, g_I is the shape function associated with $\mathbf{x}_I$, and $\mathbf{u}_I$ is the corresponding coefficient. Introducing the approximation $\mathbf{u}^h(\mathbf{x})$ and enforcing the residuals to be zero at N_C collocation points $\{\boldsymbol{\xi}_J\}_{J=1}^{N_C} \in \overline{\Omega} \equiv \Omega \cup \partial\Omega$, we have

$$\begin{aligned}
\mathbf{L}\mathbf{u}^h(\boldsymbol{\xi}_J) &= \mathbf{f}(\boldsymbol{\xi}_J) \quad \forall \boldsymbol{\xi}_J \in \Omega, \\
\mathbf{B}_h\mathbf{u}^h(\boldsymbol{\xi}_J) &= \mathbf{h}(\boldsymbol{\xi}_J) \quad \forall \boldsymbol{\xi}_J \in \partial\Omega_h, \\
\mathbf{B}_g\mathbf{u}^h(\boldsymbol{\xi}_J) &= \mathbf{g}(\boldsymbol{\xi}_J) \quad \forall \boldsymbol{\xi}_J \in \partial\Omega_g,
\end{aligned} \tag{156}$$

where $\mathbf{L}$, $\mathbf{B}_{h,}$ and $\mathbf{B}_g$ are the differential operators associated with the domain equations, Neumann boundary, and Dirichlet boundary, respectively. The operators for two model problems, Poisson's equation and elasticity, are given in Table 2 in two dimensions.

If $N_c = N_s$, the approach is termed as the direct collocation method (Hu *et al.,* 2007). When $N_c > N_s$, (158) leads to an overdetermined system and its solution can be obtained using a least-squares method. The solution from an overdetermined system usually offers better accuracy and is less sensitive to the nodal distribution; however, to achieve optimal accuracy, the least-squares system needs to be properly weighted for domain and boundary equations, which is referred to as the weighted collocation method. The details are discussed in Section 7.2.

The collocation in equation (156) is equivalent to the weighted residual of the boundary value problem as seeking $\mathbf{u}^h \in H^2$ such that $\forall\, \mathbf{w}, \mathbf{w}_h, \mathbf{w}_g \in L^2$:

$$\begin{aligned}
&\int_\Omega \mathbf{w}(\mathbf{x}) \cdot (\mathbf{L}\mathbf{u}^h(\mathbf{x}) - \mathbf{f}(\mathbf{x}))\mathrm{d}\Omega, \\
&\quad + \int_{\partial\Omega_h} \mathbf{w}_h(\mathbf{x}) \cdot (\mathbf{B}_g\mathbf{u}^h(\mathbf{x}) - \mathbf{h}(\mathbf{x}))\mathrm{d}\Gamma \\
&\quad + \int_{\partial\Omega_g} \mathbf{w}_g(\mathbf{x}) \cdot (\mathbf{B}_g\mathbf{u}^h(\mathbf{x}) - \mathbf{g}(\mathbf{x}))d\Gamma = 0
\end{aligned} \tag{157}$$

The weighted residual (157) leads to (156) when $\mathbf{w} = \mathbf{w}_h = \mathbf{w}_g = \sum_{J=1}^{N_C} \delta(\mathbf{x} - \boldsymbol{\xi}_J)\overline{\mathbf{w}}_J$ where $\delta(\cdot)$ is the multidimensional Dirac Delta function and $\overline{\mathbf{w}}_J$ is the corresponding arbitrary coefficient. Note that in this approach the admissible approximation $\mathbf{u}^h$ is required to be in H^2, which is difficult for the conventional FEM approximation to achieve. However, for the RK approximations discussed in Section 2, the regularity requirement can be readily met.

In matrix form, (156) can be rewritten as:

$$\begin{aligned}
\sum_{I\in Z} \mathbf{L}g_I(\boldsymbol{\xi}_J)\mathbf{u}_I &= \mathbf{f}(\boldsymbol{\xi}_J) \;\; \forall \boldsymbol{\xi}_J \in \Omega, \\
\sum_{I\in Z} \mathbf{B}_h g_I(\boldsymbol{\xi}_J)\mathbf{u}_I &= \mathbf{h}(\boldsymbol{\xi}_J) \;\; \forall \boldsymbol{\xi}_J \in \partial\Omega_h, \\
\sum_{I\in Z} \mathbf{B}_g g_I(\boldsymbol{\xi}_J)\mathbf{u}_I &= \mathbf{g}(\boldsymbol{\xi}_J) \;\; \forall \boldsymbol{\xi}_J \in \partial\Omega_g
\end{aligned} \tag{158}$$

Although the employment of a C^1 continuous kernel, such as the quadratic B-spline kernel, in the RK approximation satisfies the regularity requirements of strong form collocation, higher order continuous kernels offer better numerical stability, especially when the point density is high. A quintic B-spline is often adopted in RKCM:

$$\phi_a(z) = \begin{cases}
\dfrac{11}{20} - \dfrac{9}{2}z^2 + \dfrac{81}{4}z^4 - \dfrac{81}{4}z^5 \\
\qquad \text{for } 0 \le z \le \dfrac{1}{3} \\
\dfrac{17}{40} + \dfrac{15}{8}z - \dfrac{63}{4}z^2 + \dfrac{135}{4}z^3 - \dfrac{243}{8}z^4 + \dfrac{81}{8}z^5 \\
\qquad \text{for } \dfrac{1}{3} \le z \le \dfrac{2}{3} \\
\dfrac{81}{40} - \dfrac{81}{8}z + \dfrac{81}{4}z^2 - \dfrac{81}{4}z^4 + \dfrac{81}{8}z^4 - \dfrac{81}{40}z^5 \\
\qquad \text{for } \dfrac{2}{3} \le z \le 1 \\
0 \qquad \text{for } z > 1
\end{cases} \tag{159}$$

7.2 Weighted collocation method

The collocation equations can be recast in a matrix form as:

$$\mathbf{K}\mathbf{d} = \mathbf{f} \tag{160}$$

When $N_C > N_S$, the above equations lead to an overdetermined system, and a least-squares method can be applied for seeking the solution, equivalent to minimizing a weighted residual. The residual is defined as $e(\mathbf{d}) = 1/2(\mathbf{K}\mathbf{d} - \mathbf{f})^T\mathbf{W}(\mathbf{K}\mathbf{d} - \mathbf{f})$, where $\mathbf{W}$ is a symmetric weighting matrix. Minimizing $e(\mathbf{d})$ yields

$$\mathbf{K}^T\mathbf{W}\mathbf{K}\mathbf{d} = \mathbf{K}^T\mathbf{W}\mathbf{f} \tag{161}$$

It has been shown in Hu *et al.* (2007) that solving strong form collocation equations by a least-squares method is equivalent to minimizing a least-squares functional with

Table 2. Differential operators for Poisson's equation and elasticity in two dimensions.

Operator	Poisson's Equation	Elasticity Problem
$\mathbf{L}$	$\frac{\partial}{\partial x^2}+\frac{\partial}{\partial y^2}$	$\begin{bmatrix}(\lambda+2\mu)\frac{\partial^2}{\partial x^2}+\mu\frac{\partial^2}{\partial y^2} & (\lambda+\mu)\frac{\partial}{\partial x\partial y}\\ (\lambda+\mu)\frac{\partial}{\partial x\partial y} & \mu\frac{\partial^2}{\partial x^2}+(\lambda+2\mu)\frac{\partial^2}{\partial y^2}\end{bmatrix}$
$\mathbf{B}_h$	$n_x\frac{\partial}{\partial x}+n_y\frac{\partial}{\partial y}$	$\begin{bmatrix}(\lambda+2\mu)n_x\frac{\partial}{\partial x}+\mu n_y\frac{\partial}{\partial y} & \mu n_y\frac{\partial}{\partial x}+\lambda n_x\frac{\partial}{\partial y}\\ \lambda n_y\frac{\partial}{\partial x}+\mu n_x\frac{\partial}{\partial y} & \mu n_x\frac{\partial}{\partial x}+(\lambda+2\mu)n_y\frac{\partial}{\partial y}\end{bmatrix}$
$\mathbf{B}_g$	1	$\begin{bmatrix}1 & 0\\ 0 & 1\end{bmatrix}$

quadrature. It states to find $\mathbf{u}^h$ such that

$$E(\mathbf{u}^h)=\inf_{\mathbf{v}\in V} E(\mathbf{v}) \tag{162}$$

where V is an admissible finite dimensional space spanned by meshfree shape functions, and

$$\begin{aligned}E(\mathbf{v})=&\frac{1}{2}\hat{\int}_\Omega(\mathbf{L}\mathbf{v}-\mathbf{f})^2\mathrm{d}\Omega\\&+\frac{1}{2}\hat{\int}_{\partial\Omega_h}(\mathbf{B}_h\mathbf{v}-\mathbf{h})^2\mathrm{d}\Gamma+\frac{1}{2}\hat{\int}_{\partial\Omega_g}(\mathbf{B}_g\mathbf{v}-\mathbf{g})^2\mathrm{d}\Gamma\end{aligned} \tag{163}$$

Recall that $\hat{\int}$ denotes integration with quadrature. It has been shown in Hu *et al.* (2007) that the errors from the domain and boundary integrals in (163) are unbalanced. Therefore, a weighted least-squares functional can be introduced:

$$\begin{aligned}E(\mathbf{v})=&\frac{1}{2}\hat{\int}_\Omega(\mathbf{L}\mathbf{v}-\mathbf{f})^2\mathrm{d}\Omega+\frac{\alpha_h}{2}\hat{\int}_{\partial\Omega_h}(\mathbf{B}_h\mathbf{v}-\mathbf{h})^2\mathrm{d}\Gamma\\&+\frac{\alpha_g}{2}\hat{\int}_{\partial\Omega_g}(\mathbf{B}_g\mathbf{v}-\mathbf{g})^2\mathrm{d}\Gamma\end{aligned} \tag{164}$$

Here, the weights α_h and α_g are determined by considering error balancing of the weighted least-squares functional associated with the domain and boundary equations in Hu *et al.* (2007):

$$\sqrt{\alpha_h}\approx O(1),\quad \sqrt{\alpha_g}\approx O(\kappa N_S) \tag{165}$$

For Poisson's equation, $\kappa=1$; for elasticity, $\kappa=\max(\lambda,\mu)$, or more generally, the maximum coefficient involved in the differential operator and boundary operator for the problem at hand. For strong form collocation with mixed interpolations in nearly incompressible problems, the weights for collocation equations have been estimated (Chi *et al.*, 2014).

Minimizing (164) is equivalent to solving the following weighted collocation equations by a least squares method:

$$\begin{aligned}\sum_{I\in Z}\mathbf{L}g_I(\boldsymbol{\xi}_J)\mathbf{u}_I&=-\mathbf{b}(\boldsymbol{\xi}_J)&&\forall\boldsymbol{\xi}_J\in\Omega,\\ \sqrt{\alpha_h}\sum_{I\in Z}\mathbf{B}_h g_I(\boldsymbol{\xi}_J)\mathbf{u}_I&=\sqrt{\alpha_h}\mathbf{h}(\boldsymbol{\xi}_J)&&\forall\boldsymbol{\xi}_J\in\partial\Omega_h,\\ \sqrt{\alpha_g}\sum_{I\in Z}\mathbf{B}_g g_I(\boldsymbol{\xi}_J)\mathbf{u}_I&=\sqrt{\alpha_g}\mathbf{g}(\boldsymbol{\xi}_J)&&\forall\boldsymbol{\xi}_J\in\partial\Omega_g\end{aligned} \tag{166}$$

For a smooth function $u(\mathbf{x})$, when solving a PDE by collocation (166) with the RK approximation $u^h(\mathbf{x})$, there exists an algebraic convergence rate as shown by Hu *et al.* (2009):

$$\left\|u-u^h\right\|_E\le C\chi a^{p-1}|u|_{p+1,\Omega} \tag{166}$$

where C is a generic constant, χ is the overlapping parameter, a is the support measure, p is the order of complete monomials in RK shape functions, and

$$\|v\|_E\equiv\left(\|v\|^2_{1,\Omega}+\|Lv\|^2_{0,\Omega}+\left\|B_h v\right\|^2_{0,\partial\Omega_h}+\left\|B_g v\right\|^2_{0,\partial\Omega_g}\right)^{\frac{1}{2}} \tag{166}$$

Remark 3.

1. The collocation points in the strong form collocation method play a similar role as the quadrature points in the least-squares method. The strong form collocation method requires second-order differentiation

of the approximation functions for the solution of a second-order PDE. Higher order differentiation in the approximation function, typically, requires higher order quadrature rules for sufficient accuracy in the solution process. Therefore, the use of more collocation points N_c is necessary for solution accuracy (Hu *et al.,* 2007, 2009, 2011).

2. As shown in (166), the solution using RKCM does not converge when $p = 1$ is used for solving a second-order PDE. $p \geq 2$ is mandatory for convergence.

7.3 Localized radial basis collocation method (L-RBCM)

RBFs have been popularly used for solving PDEs with collocation methods since Kansa's seminal work (Kansa, 1990a,b). RBFs are functions dependent only on the Euclidean distance from the *source point* of a RBF; therefore, they are very easy to construct. Hardy (1971) first investigated RBFs for interpolation problems, and Franke and Schaback (1998) showed good performance in scattered data interpolation using multiquatric and thin-plate spline radial basis functions. Since then, the advances in applying RBFs to various problems have progressed constantly. A few commonly used RBFs are given in Table 3, where $r_I = \|\mathbf{x} - \mathbf{x}_I\|$ with $\|\cdot\|$ the Euclidean norm, $\mathbf{x}_I$ is the source point of the RBF, and the constant c is called the *shape parameter* of the RBF.

The works of Madych (1992), Wu and Schaback (1993), and Yoon (2001) show that there exists an exponential convergence rate in RBFs. However, the RBF-based method suffers from large condition numbers owing to its "non-local" approximation. The RK functions, on the other hand, provide polynomial reproducibility and locality, and the corresponding discrete systems are relatively well conditioned (Hu *et al.*, 2011). An approach has been proposed to combine the advantages of RBFs and RK functions to yield a local approximation that is better conditioned than the RBFs, while at the same time offers a higher rate of convergence than that of RK in (36):

$$u^h(\mathbf{x}) = \sum_{I=1}^{N} \left[\Psi_I(\mathbf{x}) \left(a_I + \sum_{J=1}^{M} g_I^J(\mathbf{x}) d_I^J \right) \right] \tag{167}$$

where $\Psi_I(\mathbf{x})$ is the RK function (36) with compact support, and g_I is the RBF. Application of the approximation in (167) to the weighted strong form collocation as described in Section 7.2 is termed the localized radial basis collocation method (L-RBCM).

The above approximation utilizes the compactly supported partition of unity to "patch" the global RBFs together. Error analysis shows that if the error of the RK approximation is sufficiently small, the proposed method maintains the exponential convergence of RBFs, while significantly improving the condition of the discrete system, and yields a banded matrix (Chen *et al.*, 2008) as discussed below.

1. Using the partition of unity properties of the RK localizing function, there exists the following error bound (Chen *et al.*, 2008):

$$||u - u_I^h||_{0,\Omega} \leq \beta C \eta_0^{c/\delta} ||u||_t \tag{168}$$

   where β is the maximum cover number for the RK localizing function, $0 < \eta_0 < 1$, δ is the maximum nodal distance, and $\|\cdot\|_t$ is induced from Fourier transforms of RBFs.
2. The enhanced stability in the L-RBCM can be demonstrated by a perturbation analysis of the strong form collocation equations in (158) or in the matrix form (160).

The work in Chen *et al.* (2008) obtained the following estimation of the condition number of L-RBCM:

$$Cond(\mathbf{K}) \approx O(a^{-3d/2}) \tag{169}$$

where d is the spatial dimension. In two-dimensional elasticity, we have the following comparison of condition numbers using RBCM with pure RBFs, RKPM with pure RK in (36), and L-RBCM with localized RBFs in (167):

Table 3. Commonly used radial basis functions.

Multiquadrics (MQ)	$g_I(\mathbf{x}) = (r_I^2 + c^2)^{n-\frac{3}{2}}$
Gaussian	$g_I(\mathbf{x}) = \begin{cases} \exp\left(-\frac{r_I^2}{c^2}\right) \\ (r_I^2 + c^2)^{n-\frac{3}{2}} \exp\left(-\frac{r_I^2}{a^2}\right) \end{cases}$
Thin plate splines	$g_I(\mathbf{x}) = \begin{cases} r_I^{2n} \ln r_I \\ r_I^{2n-1} \end{cases}$
Logarithmic	$g_I(\mathbf{x}) = r_I^n \ln r_I$

$$\begin{aligned} \text{RBCM} &: \mathit{Cond}(\mathbf{K}) \approx O(h^{-8}), \\ \text{RKPM} &: \mathit{Cond}(\mathbf{K}) \approx O(h^{-2}), \\ \text{L-RBCM} &: \mathit{Cond}(\mathbf{K}) \approx O(h^{-3}) \end{aligned} \tag{170}$$

The L-RBCM approach offers a significant improvement on stability over RBCM. Although the discrete system of L-RBCM is slightly less well conditioned than that of RKPM, it offers a higher convergence rate similar to that in RBCM.

7.4 Implicit gradient reproducing kernel collocation method

The development of strong form collocation methods circumvents the domain integration issue in the Galerkin type formulation. Nevertheless, increased computational complexity due to the need for higher order derivatives of the RK approximation functions compromises the effectiveness of the RKCM. The implicit G-RKCM (Chi *et al.,* 2013) is intended for addressing such issue in RKCM while achieving optimal convergence by introducing a gradient RK approximation (Chen *et al.,* 2004).

To illustrate, consider a general boundary value problem in two dimensions with split differential operations as follows:

$$\begin{aligned} \mathbf{L}^1 u_x^h + \mathbf{L}^2 u_y^h &= \mathbf{f} \quad \text{in } \Omega \\ \mathbf{B}_h^1 u_x^h + \mathbf{B}_h^2 u_y^h &= \mathbf{h} \quad \text{on } \partial\Omega_h \\ \mathbf{B}_g \mathbf{u}^h &= \mathbf{g} \quad \text{on } \partial\Omega_g \end{aligned} \tag{171}$$

The explicit forms of the operators and vectors for Poisson's equation and elasticity in two dimension are given in Table 4.

The approximations of $\mathbf{u}$, $\mathbf{u}_{,x}$, and $\mathbf{u}_{,y}$ are given as

$$\begin{aligned} \mathbf{u}_{,x} \approx \mathbf{w}_x &= \sum_{I=1}^{N_S} \overline{\Psi}_I^{10}(\mathbf{x})\mathbf{d}_I, \\ \mathbf{u}_{,y} \approx \mathbf{w}_y &= \sum_{I=1}^{N_S} \overline{\Psi}_I^{01}(\mathbf{x})\mathbf{d}_I \end{aligned} \tag{172}$$

where $\overline{\Psi}_I^{10}$ and $\overline{\Psi}_I^{01}$ are the (two-dimensional) implicit gradient RK shape functions in (46).

Consequently, the second-order derivatives of $\mathbf{u}$ are obtained by taking direct derivatives of $\mathbf{w}_x$ and $\mathbf{w}_y$, that is,

Table 4. Explicit forms of operators for Poisson's equation and elasticity in two dimensions.

Operator	Poisson's equation	Elasticity problem
$\mathbf{L}^1$	$\dfrac{\partial}{\partial x}$	$\begin{bmatrix} (\lambda+2\mu)\dfrac{\partial}{\partial x} & \mu\dfrac{\partial}{\partial y} \\ \lambda\dfrac{\partial}{\partial y} & \mu\dfrac{\partial}{\partial x} \end{bmatrix}$
$\mathbf{L}^2$	$\dfrac{\partial}{\partial y}$	$\begin{bmatrix} \mu\dfrac{\partial}{\partial y} & \lambda\dfrac{\partial}{\partial x} \\ \mu\dfrac{\partial}{\partial x} & (\lambda+2\mu)\dfrac{\partial}{\partial y} \end{bmatrix}$
$\mathbf{B}_h^1$	n_x	$\begin{bmatrix} (\lambda+2\mu)n_x & \mu n_y \\ \lambda n_y & \mu n_x \end{bmatrix}$
$\mathbf{B}_h^2$	n_y	$\begin{bmatrix} \mu n_y & \lambda n_x \\ \mu n_x & (\lambda+2\mu)n_y \end{bmatrix}$
$\mathbf{B}_g$	1	$\begin{bmatrix} 1 & 0 \\ 0 & 1 \end{bmatrix}$

λ and μ are Lamé constants; n_x and n_y are the components of the unit outward normal.

$$\begin{aligned} \mathbf{u}_{,xx} \approx \mathbf{w}_{x,x} &= \sum_{I=1}^{N_s} \overline{\Psi}_{I,x}^{10}(\mathbf{x})\mathbf{d}_I, \\ \mathbf{u}_{,yy} \approx \mathbf{w}_{y,y} &= \sum_{I=1}^{N_s} \overline{\Psi}_{I,y}^{01}(\mathbf{x})\mathbf{d}_I \end{aligned} \tag{173}$$

The weighted collocation equations with gradient approximations given in (172) and (173) are

$$\underbrace{\begin{pmatrix} \mathbf{A}^1 + \mathbf{A}^2 \\ \sqrt{\alpha_h}(\mathbf{A}^3 + \mathbf{A}^4) \\ \sqrt{\alpha_g}\mathbf{A}^5 \end{pmatrix}}_{\mathbf{A}} \mathbf{d} = \underbrace{\begin{pmatrix} \mathbf{b}^1 \\ \sqrt{\alpha_h}\mathbf{b}^2 \\ \sqrt{\alpha_g}\mathbf{b}^3 \end{pmatrix}}_{\mathbf{b}} \tag{174}$$

The submatrices in matrix $\mathbf{A}$ for Poisson's equation and elasticity are summarized in Table 5. For a balance of errors between the domain and boundary equations, the following weights for optimal solutions have been estimated (Chi *et al.,* 2013):

$$\sqrt{\alpha_h} \approx O(1), \quad \sqrt{\alpha_g} \approx O(\kappa a^{q-p-1}) \tag{175}$$

where for Poisson's equation, $\kappa = 1$; for elasticity, $\kappa = \max(\lambda, \mu)$.

Table 5. Submatrices in discrete equations for Poisson's equation and elasticity.

Submatrix	Poisson's equation	Elasticity problem
$\mathbf{A}_{IJ}^1$	$[\overline{\Psi}_{J,x}^{10}(\mathbf{p}_I)]$	$\begin{bmatrix} (\lambda+2\mu)\overline{\Psi}_{J,x}^{10}(\mathbf{p}_I) & \mu\overline{\Psi}_{J,y}^{10}(\mathbf{p}_I) \\ \lambda\overline{\Psi}_{J,y}^{10}(\mathbf{p}_I) & \mu\overline{\Psi}_{J,x}^{10}(\mathbf{p}_I) \end{bmatrix}$
$\mathbf{A}_{IJ}^2$	$[\overline{\Psi}_{J,y}^{01}(\mathbf{p}_I)]$	$\begin{bmatrix} \mu\overline{\Psi}_{J,y}^{01}(\mathbf{p}_I) & \lambda\overline{\Psi}_{J,x}^{01}(\mathbf{p}_I) \\ \mu\overline{\Psi}_{J,x}^{01}(\mathbf{p}_I) & (\lambda+2\mu)\overline{\Psi}_{J,y}^{01}(\mathbf{p}_I) \end{bmatrix}$
$\mathbf{A}_{IJ}^3$	$[\overline{\Psi}_J^{10}(\mathbf{q}_I)n_x]$	$\begin{bmatrix} (\lambda+2\mu)\overline{\Psi}_J^{10}(\mathbf{q}_I)n_1 & \mu\overline{\Psi}_J^{10}(\mathbf{q}_I)n_2 \\ \lambda\overline{\Psi}_J^{10}(\mathbf{q}_I)n_2 & \mu\overline{\Psi}_J^{10}(\mathbf{q}_I)n_1 \end{bmatrix}$
$\mathbf{A}_{IJ}^4$	$[\overline{\Psi}_J^{01}(\mathbf{q}_I)n_y]$	$\begin{bmatrix} \mu\overline{\Psi}_J^{01}(\mathbf{q}_I)n_2 & \lambda\overline{\Psi}_J^{01}(\mathbf{q}_I)n_1 \\ \mu\overline{\Psi}_J^{01}(\mathbf{q}_I)n_1 & (\lambda+2\mu)\overline{\Psi}_J^{01}(\mathbf{q}_I)n_2 \end{bmatrix}$
$\mathbf{A}_{IJ}^5$	$[\Psi_J(\mathbf{r}_I)]$	$\begin{bmatrix} \Psi_J(\mathbf{r}_I) & 0 \\ 0 & \Psi_J(\mathbf{r}_I) \end{bmatrix}$

$\mathbf{p}_I$, $\mathbf{q}_I$, and $\mathbf{r}_I$ are the vectors of collocation points in Ω, on $\partial\Omega_h$, and on $\partial\Omega_g$ respectively.

The error estimate of G-RKCM is given (Chi *et al.,* 2013):

$$\left\|u-u^h, u_{,x}-u_{,x}^h, u_{,y}-u_{,y}^h\right\|_E \leq a^{q-1}(C_{11}|u|_{q+1,\Omega}+C_{12}|u|_{p+1,\Omega}) \tag{176}$$

where

$$\left\|v, w_x, w_y\right\|_E = \left\{\left\|w_{x,x}+w_{y,y}\right\|_{0,\Omega}^2+\alpha_h\left\|w_n\right\|_{0,\partial\Omega_h}^2+\alpha_g\|v\|_{0,\partial\Omega_g}^2\right\}^{1/2} \tag{177}$$

Here a is a support measure, and p and q are the polynomial degrees in the approximation of $\mathbf{u}$ and the approximation of $\mathbf{u}_{,x}$ and $\mathbf{u}_{,y}$, respectively.

Remark 4.

1. The results in (176) indicate that the convergence of this method is only dependent on the polynomial degree q in the approximation of $\mathbf{u}_{,x}$ and $\mathbf{u}_{,y}$, and is independent of the polynomial degree p in the approximation of $\boldsymbol{u}$. Further, $q \geq 2$ is needed for convergence.
2. In comparison to RKCM, the order of differentiation for G-RKCM is reduced owing to the introduction of implicit gradient approximations. As such, G-RKCM allows the use of $N_C = N_S$ for sufficient accuracy; see (Chi *et al.,* 2013) for details.

8 REPRODUCING KERNEL PARTICLE METHOD FOR LARGE DEFORMATION PROBLEMS

8.1 Lagrangian reproducing kernel approximation and discretization

The RK approximation is constructed on the basis of a set of points without mesh and hence releases the strong dependence of the approximation accuracy on mesh quality. It is, therefore, well suited for application on extreme deformation problems. To illustrate, let $\mathbf{X}$ be the material coordinates for a body initially occupying the domain Ω_X with the boundary Γ_X and let $\mathbf{x} = \boldsymbol{\varphi}(\mathbf{X}, t)$ with $\boldsymbol{\varphi}$ a mapping function be the position of the material point $\mathbf{X}$ in the deformed configuration Ω_x with the boundary Γ_x at time t. Under this Lagrangian formulation, it is assumed that the Jacobian of deformation gradient, $\det(F_{ij})$, is neither zero nor infinite, where $F_{ij} = \mathrm{d}x_i/\mathrm{d}X_j$.

The variational equation of motion with reference to the current configuration is

$$\int_{\Omega_x}\delta u_i\rho\ddot{u}_i\mathrm{d}\Omega+\int_{\Omega_x}\delta u_{i,j}\sigma_{ij}\mathrm{d}\Omega=\int_{\Omega_x}\delta u_i b_i\mathrm{d}\Omega+\int_{\Gamma_x^h}\delta u_i h_i\mathrm{d}\Gamma \tag{178}$$

where u_i is the displacement, ρ is the density of the material, σ_{ij} is the Cauchy stress, b_i is the body force, and h_i is the prescribed traction on the natural boundary Γ_x^h. In the Lagrangian formulation (Chen *et al.,* 1996, 1997, 1998; Wu *et al.,* 2001), the Lagrangian RK shape functions $\Psi_I^{\mathbf{X}}(\mathbf{X})$ are constructed with similar RK procedures in (33)–(38) using the material coordinates in the reference configuration to yield

$$\Psi_I^{\mathbf{X}}(\mathbf{x}) = \mathbf{H}^T(\mathbf{0})\mathbf{M}^{-1}(\mathbf{X})\mathbf{H}(\mathbf{X}-\mathbf{X}_I)\phi_a(\mathbf{X}-\mathbf{X}_I) \tag{179}$$

where

$$\mathbf{M}(\mathbf{X}) = \sum_{I=1}^{NP}\mathbf{H}(\mathbf{X}-\mathbf{X}_I)\mathbf{H}^T(\mathbf{X}-\mathbf{X}_I)\phi_a(\mathbf{X}-\mathbf{X}_I) \tag{180}$$

The discrete reproducing conditions are imposed in the reference configuration

$$\sum_{I=1}^{NP}\Psi_I^{\mathbf{X}}(\mathbf{X})\mathbf{X}_I^{\alpha} = \mathbf{X}^{\alpha}, \qquad |\alpha| \leq n \tag{181}$$

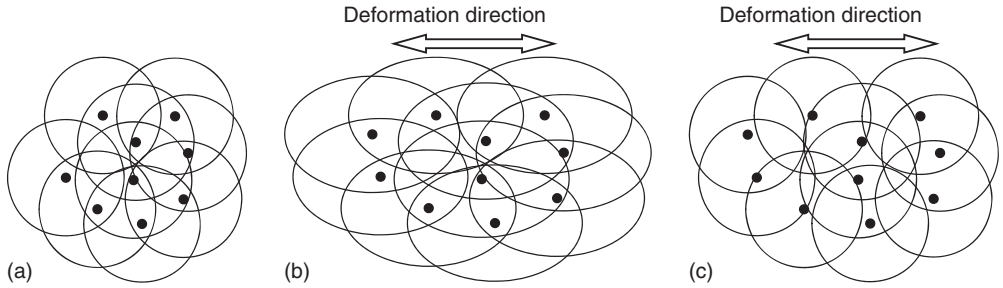

Figure 19. Comparison of Lagrangian and semi-Lagrangian RK shape functions: (a) undeformed configuration, (b) Lagrangian RK in the deformed configuration, and (c) semi-Lagrangian RK in the deformed configuration.

The Lagrangian RK function has a deformation-dependent support size when mapped to the current configuration, as shown in Figure 19.

For path-dependent materials, the discretization of (178) by the Lagrangian RK approximation requires the spatial derivatives of $\Psi_I^{\mathbf{X}}(\mathbf{X})$ as follows (Chen *et al.,* 1996, 1997, 1998; Wu *et al.*, 2001):

$$\frac{\partial \Psi_I^{\mathbf{X}}(\mathbf{X})}{\partial x_i} = \frac{\partial \Psi_I^{\mathbf{X}}(\mathbf{X})}{\partial X_j} F_{ji}^{-1} \tag{182}$$

The deformation gradient $\mathbf{F}$ is first computed by taking the material spatial derivatives of $\Psi_I^{\mathbf{X}}(\mathbf{X})$, and $\mathbf{F}^{-1}$ is obtained directly by the inversion of $\mathbf{F}$. The Lagrangian formulation breaks down when the inverse of $\mathbf{F}$ is not available. This may occur, for example, when extreme deformation leads to a non-positive definite $\mathbf{F}$ or when material separation takes place. Thus, a semi-Lagrangian RK formulation has been introduced (Guan *et al.*, 2009, 2011). It is discussed in the following section to address this issue in modeling extreme deformation problems.

8.2 Semi-Lagrangian reproducing kernel approximation and discretization

In the semi-Lagrangian RK formulation (Guan *et al.*, 2009, 2011), the nodal point $\mathbf{x}_I$ associated with the RK shape functions $\Psi_I(\mathbf{x})$ follows the motion of material point, that is, $\mathbf{x}_I = \boldsymbol{\varphi}(\mathbf{X}_I, t)$, whereas the support radius in the kernel function is defined independent of the material deformation as shown in Figure 19.

The semi-Lagrangian RK shape function $\Psi_I^{SL}(\mathbf{x})$ is then formulated in the current configuration as

$$\Psi_I^{SL}(\mathbf{x}) = C(\mathbf{x}; \mathbf{x} - \boldsymbol{\varphi}(\mathbf{X}_I, t))\phi_a(\mathbf{x} - \boldsymbol{\varphi}(\mathbf{X}_I t)) \tag{183}$$

The correction function $C(\mathbf{x}; \mathbf{x} - \boldsymbol{\varphi}(\mathbf{X}_I, t)) = \mathbf{H}(\mathbf{x} - \boldsymbol{\varphi}(\mathbf{X}_I, t))\mathbf{b}(\mathbf{x})$ (cf. (34)) is computed based on the material point in the current configuration, $\mathbf{x}(\mathbf{X}, t)$. Similar to the discussion in Section 2, the coefficient vector $\mathbf{b}(\mathbf{x})$ can be determined by imposing the following discrete reproducing condition

$$\sum_{I=1}^{NP} \Psi_I^{SL}(\mathbf{x})\mathbf{x}_I^{\alpha} = \mathbf{x}^{\alpha}, \qquad |\alpha| \le n \tag{184}$$

Substituting the coefficient vector $\mathbf{b}(\mathbf{x})$ into (183) yields the semi-Lagrangian reproducing kernel (semi-Lagrangian RK) shape function:

$$\Psi_I^{SL}(\mathbf{x}) = \mathbf{H}^T(\mathbf{0})\mathbf{M}^{-1}(\mathbf{x})\mathbf{H}(\mathbf{x} - \boldsymbol{\varphi}(\mathbf{X}_I t))\phi_a(\mathbf{x} - \boldsymbol{\varphi}(\mathbf{X}_I t)) \tag{185}$$

where

$$\mathbf{M}(\mathbf{x}) = \sum_{I=1}^{NP} \mathbf{H}(\mathbf{x} - \boldsymbol{\varphi}(\mathbf{X}_I, t))\mathbf{H}^T(\mathbf{x} - \boldsymbol{\varphi}(\mathbf{X}_I t))\phi_a(\mathbf{x} - \boldsymbol{\varphi}(\mathbf{X}_I, t)) \tag{186}$$

Note that the $\mathbf{x}$ coordinate in Ψ_I and $\mathbf{M}$ is also a function of time. Let the velocity v_i be the primary variable in (178) and be approximated by the semi-Lagrangian RK shape functions:

$$v_i^h(\mathbf{x}, t) = \sum_{I=1}^{NP} \Psi_I^{SL}(\mathbf{x}) v_{Ii}(t) \tag{187}$$

The corresponding semi-Lagrangian approximation of acceleration is given by

$$\ddot{u}_i^h(\mathbf{x}, t) = \dot{v}_i^h(\mathbf{x}, t) = \sum_{I=1}^{NP} (\Psi_I^{SL}(\mathbf{x})\dot{v}_{Ii}(t) + \breve{\Psi}_I^{SL}(\mathbf{x}) v_{Ii}(t)) \tag{188}$$

Here $\breve{\Psi}_I^{SL}$ is the correction due to the time-dependent change of the semi-Lagrangian kernel $\dot{\phi}_a(\mathbf{x} - \mathbf{x}_I)$

$$\breve{\Psi}_I^{SL}(\mathbf{x}) = C(\mathbf{x}; \mathbf{x} - \boldsymbol{\varphi}(\mathbf{X}_I, t))\dot{\phi}_a(\mathbf{x} - \boldsymbol{\varphi}(\mathbf{X}_I, t)) \tag{189}$$

where $(\dot{\cdot})$ denotes the material time derivative and

$$\dot{\phi}_a(\mathbf{x} - \boldsymbol{\varphi}(\mathbf{X}_I, t)) = \dot{\phi}_a\left(\frac{\|\mathbf{x} - \boldsymbol{\varphi}(\mathbf{X}_I, t)\|}{a}\right) = \phi'_a \frac{\mathbf{q} \cdot (\mathbf{v} - \mathbf{v}_I)}{a} \tag{190}$$

where

$$\mathbf{q} = (\mathbf{x} - \boldsymbol{\varphi}(\mathbf{X}_I, t))/\|\mathbf{x} - \boldsymbol{\varphi}(\mathbf{X}_I, t)\| \tag{191}$$

and $\|\cdot\|$ designates the length of a vector. Note that the correction function in (188) is used to ensure the reproducing condition of the time derivative of the semi-Lagrangian kernel $\dot{\phi}_a(\mathbf{x} - \boldsymbol{\varphi}(\mathbf{X}_I t))$ and thus the time rate change of C is not considered.

Substituting (188) into (178) yields the following semi-discrete equation:

$$\mathbf{M}\dot{\mathbf{v}} + \mathbf{N}\mathbf{v} = \mathbf{f}^{ext} - \mathbf{f}^{\text{int}} \tag{192}$$

where

$$\mathbf{M}_{IJ} = \int_{\Omega_x} \rho \Psi_I^{SL}(\mathbf{x}) \Psi_J^{SL}(\mathbf{x}) \mathbf{I} \mathrm{d}\Omega \tag{193}$$

$$\mathbf{N}_{IJ} = \int_{\Omega_x} \rho \Psi_I^{SL}(\mathbf{x}) \overset{\smile SL}{\Psi_J}(\mathbf{x}) \mathbf{I} \mathrm{d}\Omega \tag{194}$$

$$\mathbf{f}_I^{ext} = \int_{\Omega_x} \Psi_I^{SL} \mathbf{b} d\Omega + \int_{\Gamma_x} \Psi_I^{SL} \mathbf{h} \mathrm{d}\Gamma \tag{195}$$

$$\mathbf{f}_I^{\text{int}} = \int_{\Omega_x} \mathbf{B}_I^T \boldsymbol{\Sigma} \mathrm{d}\Omega \tag{196}$$

Here, $\mathbf{I}$ denotes the identity matrix, $\mathbf{B}_I$ is the gradient matrix of $u_{(i,j)}$ associated with node I, and Σ is the stress vector associated with the Cauchy stress σ_{ij}. The temporal stability condition for the semi-Lagrangian RK formulation can be found in Guan *et al.* (2009, 2011).

Remark 5. If a nodal integration scheme, such as direct nodal integration, stabilized conforming nodal integration, and stabilized non-conforming nodal integration, as discussed in Section 6, is employed in Equations (192)–(196), the diagonal terms of $\mathbf{N}$ vanish and the off-diagonal terms of $\mathbf{N}$ have relatively negligible influence over (192). As such, the convective effect, $\mathbf{N}\mathbf{v}$ in (192), can be omitted in the semi-discrete equations of motion.

8.3 Smooth contact algorithm

One of the most unique properties of the RK approximation is its ease to construct smooth approximation. More specifically, the order of continuity is entirely independent of the order of monomial bases in the RK approximation. This unique property makes the RK approximation ideal for discretization of the continuum-based contact formulation that requires C^2 continuity in the approximation of geometry and displacement field. The RKPM smoothed contact formulation (Wang *et al.,* 2014) is particularly effective in the Newton iteration of sliding contact.

Curves represented by RK approximations with a cubic B-spline kernel function and various kernel support sizes are shown in Figure 20. As illustrated in this figure, the RK approximation can be constructed similarly to the piecewise linear approximation when needed, by using a support size close to the distance to the adjacent particle. As shown in Figure 20, increasing the normalized support size provides smoothing at kinks. An approximation using the Gaussian function with linear basis is shown in Figure 21. Figure 22 shows that the contact curve is well approximated by RK shape functions constructed using a cubic B-spline kernel function with quadratic basis and with sufficiently large normalized support ($a/h \geq 2.0$). Note that very coarse discretization is used in this curve representation.

In contact problems, linearization of the penalized variational equation that accounts for impenetration and stick–slip conditions requires up to third-order derivatives of the contact surface function. To ensure a continuous contact force vector and to obtain accurate contact stiffness matrices, a C^2 contact surface representation and the displacement approximation are required. This can be achieved by the RK shape functions with at least C^2 continuity in kernel function, such as the cubic B-spline function. The RKPM discretization for the continuum-based contact formulation has been proposed in Wang *et al.* (2014). A deep drawing of a sheet metal modeled by RKPM continuum-based contact formulation is shown in Figure 23. This problem involves a large sliding contact, and the modeling with C^0 contact surface representation fails to converge as reported (Wang *et al.,* 2014).

8.4 Kernel contact algorithm

In extreme deformation problems with material separation, contact surfaces are unknown and are part of the solution. In consequence, the conventional contact algorithms, in which all possible contact surfaces are defined *a priori*, are ineffective in modeling such problems. A KC algorithm to approximate the contact condition without relying on the predefined contact surfaces at the pre-processing stage has been proposed (Chi *et al.,* 2015) to address this difficult issue. The idea of KC emanates from the inherent property of the semi-Lagrangian RK shape functions, where the overlap between the kernel supports associated with particles from different bodies naturally serves as the impenetration condition; see Figure 24. By requiring the partition of

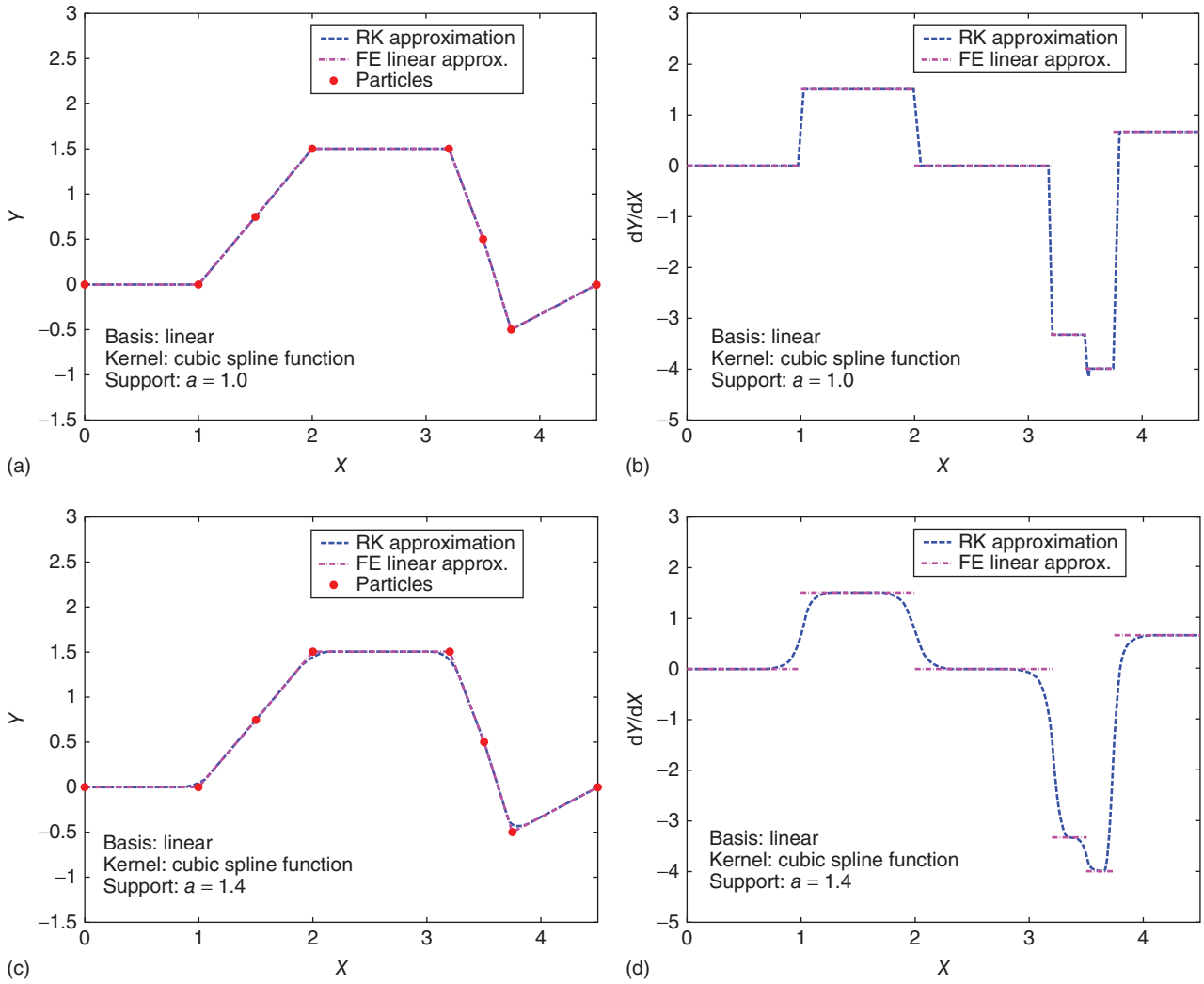

Figure 20. RK approximation: Cubic B-spline with linear basis: (a) The approximated curves with $a = 1.0$, (b) the slope of the curves with $a = 1.0$, (c) the approximated curves with $a = 1.4$, (d) the slope of the curves with $a = 1.4$. (Reproduced with permission from Wang *et al.*, 2014. © Springer, 2014.)

unity condition at all particle locations of different contacting bodies, the overlap between the semi-Lagrangian RK shape functions induces internal forces between particles, ensuring the impenetrability between different bodies. A layer of the friction-like elastoplastic material, as shown in Figure 24c, has been introduced in the "contact processing zone" to mimic the friction law (Chi *et al.,* 2015).

8.4.1 A friction-like plasticity model

In the KC, a friction-like material is introduced between contacting bodies, Ω_c as shown in Figure 24(c), to mimic the frictional contact conditions. Based on the analogy between the Coulomb's friction law and elastoplasticity flow rule, the variational contact equation leads to the constitutive equation governing the stress–strain relationship of the friction-like material such that the Coulomb's friction is recovered (Chi *et al.,* 2015):

$$\boldsymbol{\sigma}_c \cdot \mathbf{n} = t_N \mathbf{n} + \mathbf{t}_T \tag{197}$$

where σ_c are the Cauchy stress in Ω^c, $\mathbf{n}$ is the unit outward normal of the contact surface Γ^c, t_N is the normal component of the contact traction, and $\mathbf{t}_T$ is the tangential contact traction. Equation (197) indicates that the stresses in the friction-like material are in balance with t_N and $\mathbf{t}_T$ on Γ^c.

Therefore, an elasto-perfectly-plastic material, in which the stress σ_c in Ω^c obeys (197), can be introduced in the contact processing zone to mimic the Coulomb's friction law. To obtain σ_c, consider the following yield function and the

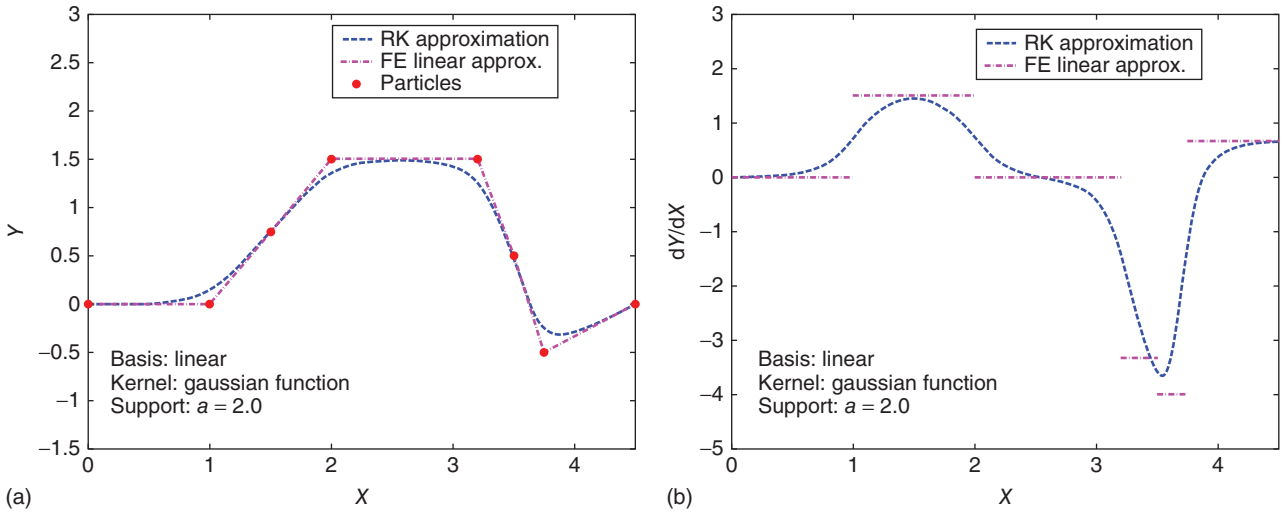

Figure 21. RK approximation: Gaussian function with linear basis: (a) The approximated curves with $a = 1.0$, (b) the slope of the curves with $a = 1.0$. (Reproduced with permission from Wang *et al.*, 2014. © Springer, 2014.)

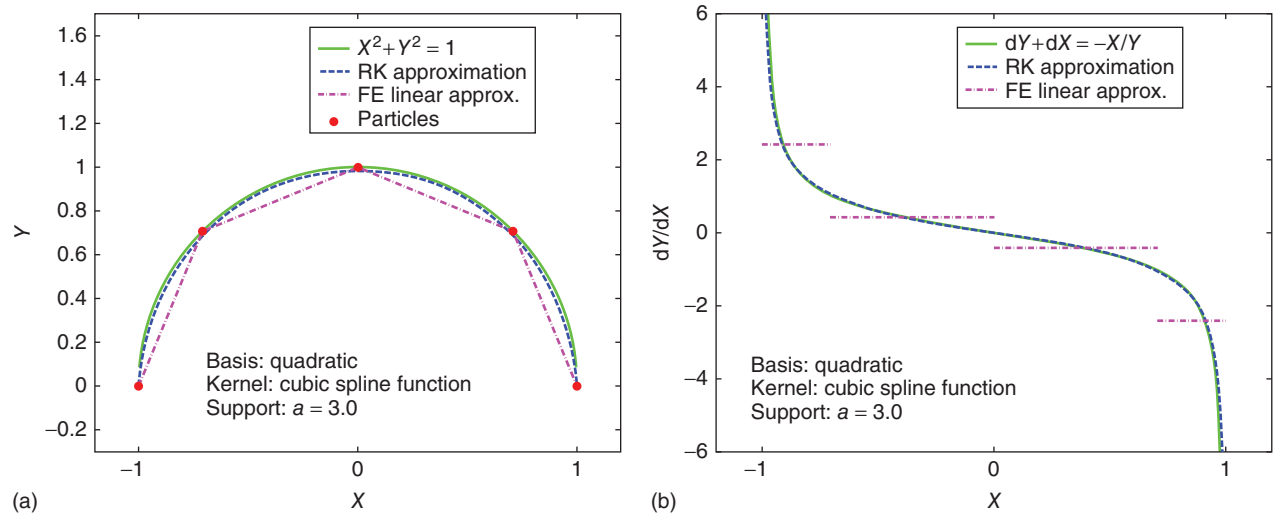

Figure 22. RK approximation: Cubic B-spline with quadratic basis: (a) The approximated curves with $a = 1.0$, (b) the slope of the curves with $a = 1.0$. (Reproduced with permission from Wang *et al.*, 2014. © Springer, 2014.)

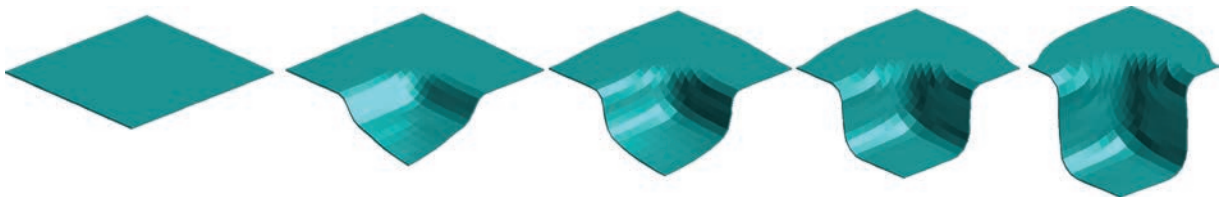

Figure 23. Progressive deformation of deep drawing.

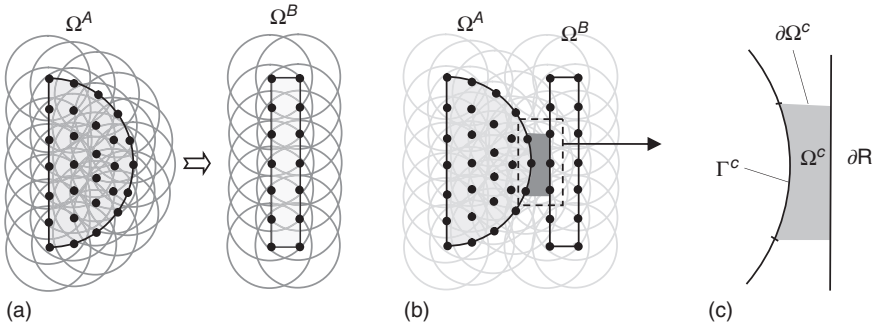

Figure 24. Natural kernel contact algorithm by kernel interaction between contacting bodies.

associated Karush–Kuhn–Tucker conditions based on local coordinates where 1-direction is aligned with the contact surface normal **n**.

$$f(\boldsymbol{\tau}) = \|\boldsymbol{\tau}\| + \mu\hat{\sigma}_{11} \le 0 \tag{198}$$

$$\dot{\mathbf{e}} = \gamma \frac{\partial f}{\partial \boldsymbol{\tau}} \tag{199}$$

$$\gamma \ge 0 \tag{200}$$

$$\gamma f = 0 \tag{201}$$

where $\boldsymbol{\tau} = \left[\hat{\sigma}_{12}\ \hat{\sigma}_{13}\right]$, $\hat{\sigma}_{11} \le 0$ is the normal contact stress, $\dot{\mathbf{e}}$ is the tangential strain rate, and $\hat{\boldsymbol{\sigma}} = \mathbf{L}\boldsymbol{\sigma}\mathbf{L}^T$ is the Cauchy stress tensor rotated onto the local coordinates, 2- and 3-directions are aligned with two mutually orthogonal unit vectors, **p** and **q**, and $\mathbf{L} = [\mathbf{n},\ \mathbf{p},\ \mathbf{q}]^T$. It is also assumed that the normal contact stress $\hat{\sigma}_{11}$ is known in (198). The yield stress $\mu|\hat{\sigma}_{11}|$ mimics the friction stress induced by the normal stress $\hat{\sigma}_{11}$, and the slip condition is represented by the yield condition in the plasticity model:

$$\begin{aligned} &f < 0, \quad \text{stick condition (elastic)} \\ &f = 0,\ \|\boldsymbol{\tau}\| = -\mu\hat{\sigma}_{11} \quad \text{slip condition (plastic)} \end{aligned} \tag{202}$$

This approach can be implemented by a predictor–corrector algorithm, in which the stresses calculated based on the overlapping supports of the contacting bodies are obtained in the predictor step, and in the corrector step the tangential stresses are corrected according to Equations (198)–(201) with $\hat{\sigma}_{11}$ fixed. To enhance the iteration convergence of the two-step approach, we introduce the radial return algorithm where the trial is non-slip (elastic trial) and the violation of yield function (interpenetration) is corrected by the return mapping algorithm. Following the radial return mapping, the corrected contact stresses $\hat{\boldsymbol{\sigma}}_c$ in the local coordinate induced by the friction-like elastoplasticity model can be obtained as

$$\hat{\boldsymbol{\sigma}}_c = \hat{\boldsymbol{\sigma}}^{\text{trial}} + \lambda \begin{bmatrix} 0 & \hat{\sigma}_{12}^{\text{trial}} & \hat{\sigma}_{13}^{\text{trial}} \\ \hat{\sigma}_{12}^{\text{trial}} & 0 & 0 \\ \hat{\sigma}_{13}^{\text{trial}} & 0 & 0 \end{bmatrix} \equiv \hat{\boldsymbol{\sigma}}^{\text{trial}} + \lambda\hat{\boldsymbol{\xi}} \tag{203}$$

where $\hat{\boldsymbol{\sigma}}^{\text{trial}}$ is the Cauchy stress in the local coordinate calculated by standard stress calculation through particle interaction without considering the artificial friction-like elastoplasticity material and $\lambda = 0$ if $f(\boldsymbol{\tau}^{\text{trial}}) < 0$ and

$$\lambda = \frac{\mu\left|\hat{\sigma}_{11}^{\text{trial}}\right| - \left\|\boldsymbol{\tau}^{\text{trial}}\right\|}{\left\|\boldsymbol{\tau}^{\text{trial}}\right\|} \quad \text{if} \quad f(\boldsymbol{\tau}^{\text{trial}}) \ge 0 \tag{204}$$

Finally, the corrected contact stresses in the global coordinates can then be obtained by the inverse transformation:

$$\boldsymbol{\sigma}_c = \mathbf{L}^T\hat{\boldsymbol{\sigma}}_c\mathbf{L} \equiv \boldsymbol{\sigma}^{\text{trial}} + \lambda\boldsymbol{\xi} \tag{205}$$

where

$$\boldsymbol{\xi} = (\mathbf{n} \otimes \boldsymbol{\sigma}^{\text{trial}} \cdot \mathbf{n} + \mathbf{n} \cdot \boldsymbol{\sigma}^{\text{trial}} \otimes \mathbf{n}) - 2t_N\mathbf{n} \otimes \mathbf{n} \tag{206}$$

Here, the orthogonality of **L** is applied to derive the above relationship. Equation (205) can then be directly used in the calculation of the contact forces described in the next section.

8.4.2 Semi-Lagrangian RK discretization and natural kernel contact algorithms

This section describes the semi-Lagrangian-RK discretization and the contact force calculation in the proposed KC algorithms. Consider continuum bodies Ω^A and Ω^B (Figure 24) discretized by a group of points $G^A = \{\mathbf{x}_I | \mathbf{x}_I \in \Omega^A\}$ and $G^B = \{\mathbf{x}_I | \mathbf{x}_I \in \Omega^B\}$, respectively, with each point at $\mathbf{x}_I$ associated with a nodal volume V_I and a kernel function $\phi_{a_I}(\mathbf{x} - \mathbf{x}_I)$ with the support of radius a independent of material deformation. When the two contacting bodies Ω^A and Ω^B approach each other and the

semi-Lagrangian-RK shape functions form a partition of unity (Chi *et al.*, 2015), the interaction between the RK points from different bodies (Figure 24) induces stresses:

$$\boldsymbol{\sigma}(\mathbf{x}) = \sum_{I \in N^A \cup N^B} \mathbf{D}(\mathbf{x}) \overline{\mathbf{B}}_I(\mathbf{x}) \mathbf{d}_I \tag{207}$$

where $N^A = \{I | \mathbf{x}_I \in G^A\}$, $N^B = \{I | \mathbf{x}_I \in G^B\}$, $\mathbf{D}$ is the material response tensor of contacting bodies, and $\overline{\mathbf{B}}_I$ is the smoothed gradient matrix of the shape functions constructed by SNNI (equation (136) with non-conforming nodal domains). The contact stresses between contacting bodies are obtained by (207) when $\mathbf{n} \cdot \boldsymbol{\sigma} \cdot \mathbf{n} \leq 0$ in Ω^c. With the nodal integration schemes described in Section 6, the internal force acting on a point I can then be obtained by

$$\mathbf{f}_I = \sum_{J \in N_I^C} \overline{\mathbf{B}}_I^T(\mathbf{x}_J) \boldsymbol{\sigma}(\mathbf{x}_J) V_J \tag{208}$$

where $N_I^C = \{J | J \in N^A \cup N^B,\ \phi_{a_I}(\mathbf{x}_J - \mathbf{x}_I) \neq 0,\ \mathbf{r}_{IJ} \cdot \boldsymbol{\sigma}(\mathbf{x}_J) \cdot \mathbf{r}_{IJ} < 0,\ \mathbf{r}_{IJ} = (\mathbf{x}_I - \mathbf{x}_J)/||\mathbf{x}_I - \mathbf{x}_J||\}$ is the set that contains the neighbor points under the support of point I, while

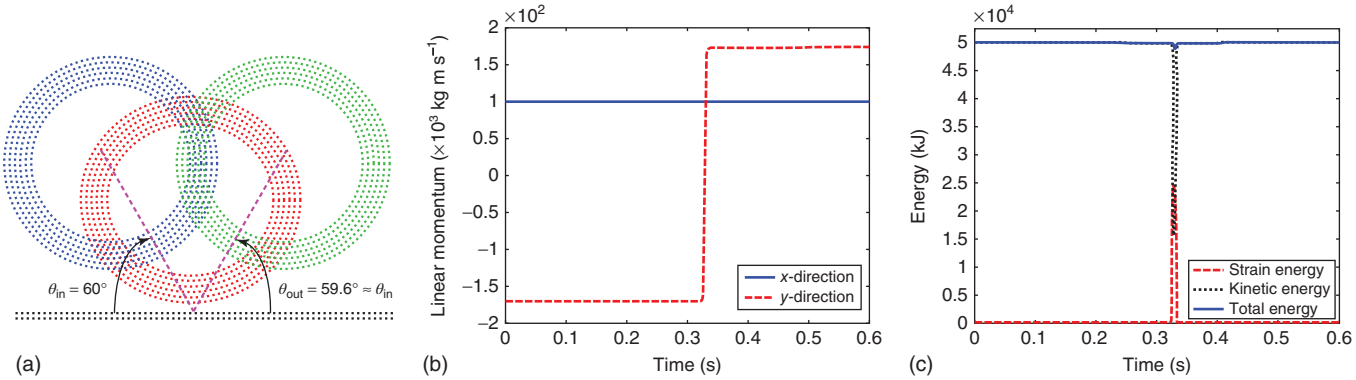

Figure 25. Elastic ring impact: (a) Incident and reflection angles, (b) linear momentum history, and (c) energy history. (Reproduced with permission from Chi *et al.*, 2015. © John Wiley & Sons, 2015.)

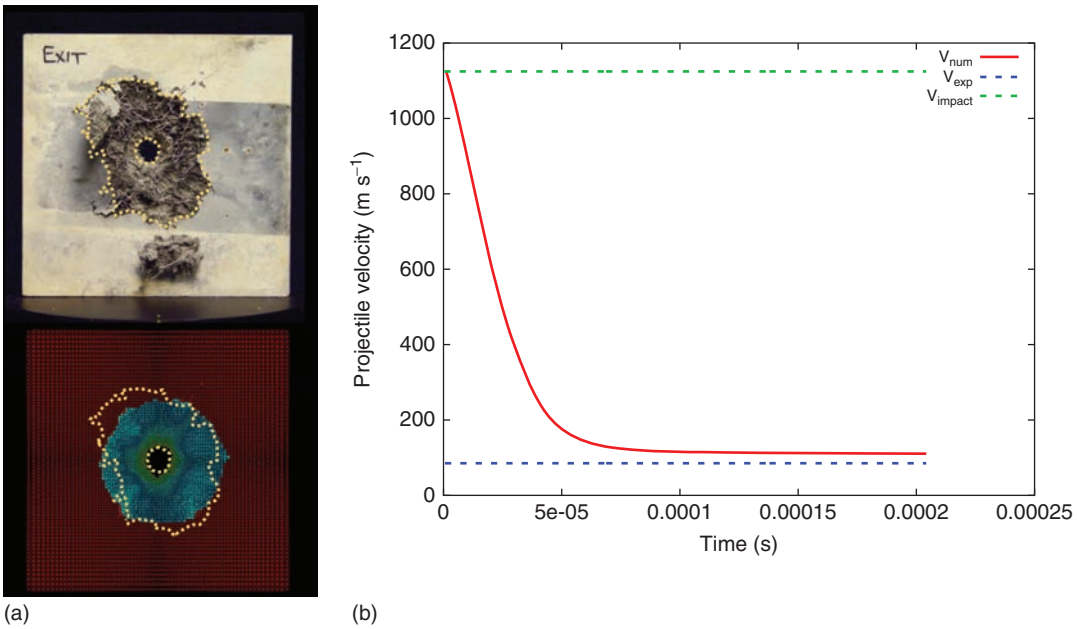

Figure 26. Penetration of a concrete panel: (a) Crater shape: top: experimental (Daniel and Danielson, 2010); bottom: numerical. (Reproduced from Recent ERDC Developments in Computationally Modeling Concrete Under High Rate Events, ERDC report, 2010.) (b) velocity of projectile: impact (dashed, green), experimental exit (dashed, blue), and numerical history (red, solid).

the contact stress between those points and point I is in compression. The pairwise interactions due to overlapping kernel functions naturally prevent the interpenetration between different bodies. An artificial layer of material with the friction-like dissipating mechanism in the form of plasticity in the previous section is introduced. With the consideration of the frictional contact effect, the summation of the interactive forces associated with point I is corrected as

$$\mathbf{f}_I = \sum_{J \in N_I^C} \overline{\mathbf{B}}_I^T(\mathbf{x}_J)\boldsymbol{\sigma}_c(\mathbf{x}_J)V_J = \sum_{J \in N_I^C} (\mathbf{f}_{IJ} + \mathbf{g}_{IJ}) \tag{209}$$

where $\mathbf{f}_{IJ} = \overline{\mathbf{B}}_I^T(\mathbf{x}_J)\boldsymbol{\sigma}^{\text{trial}}(\mathbf{x}_J)V_J$, and $\mathbf{g}_{IJ} = \overline{\mathbf{B}}_I^T(\mathbf{x}_J)\lambda\boldsymbol{\xi}(\mathbf{x}_J)V_J$.

One remaining issue to implement the KC algorithm in the semi-Lagrangian formulation is to determine the contact surface and surface normal from a purely point-based discretization. A level set based method, where the level set function was chosen as the interpolant of material ID using semi-Lagrangian RK, was introduced to obtain the contact surface and surface normal under the KC contact framework (refer to Chi *et al.* (2015) for details).

A dynamic impact of an elastic ring on a rigid surface is modeled by the KC algorithm with frictionless condition (Chi *et al.,* 2015). The comparison of the incident and reflection angles, the linear momentum, and total energy histories shown in Figure 25 demonstrate the accuracy and effectiveness of the RKPM KC algorithm.

KC is particularly effective for impact problems involving material separation where evolutionary contact surfaces are part of the solution. Semi-Lagrangian RKPM is also well suited for this class of problems since damage and fragmentation are naturally captured without treatments such as erosion that are necessary in the finite element method. Consider the penetration of a nominally 2-inch. thick CorTuf concrete (Williams *et al.,* 2009) panel by a 4340 steel fragment simulating projectile modeled using the semi-Lagrangian formulation with KC (Chi *et al.,* 2015) and the nodal integration NSNI (Hillman and Chen, 2016) described in Section 6. Further details of the experiment can be found in Daniel and Danielson (2010). The simulation results are shown in Figure 23, where it is seen that agreement is achieved with the experimental hole and crater dimensions as well as the experimental exit velocity (Figure 26).

9 RELATED CHAPTERS

(*See also* **Adaptive Wavelet Techniques in Numerical Simulation**, **Meshfree Methods**, **Particle Methods in Computational Fluid Dynamics**)

REFERENCES

Aluru NR. A point collocation method based on reproducing kernel approximations. *Int. J. Numer. Methods Eng.* 2000; **47**:1083–1121. doi: 10.1002/(SICI)1097-0207(20000228)47:6<1083::AID-NME816>3.0.CO;2-N

Atluri SN, Kim HG and Cho JY. Critical assessment of the truly meshless local Petrov–Galerkin (MLPG), and local boundary integral equation (LBIE) methods. *Comput. Mech.* 1999; **24**:348–372. doi: 10.1007/s004660050457

Atluri SN and Zhu TL. A new meshless local Petrov–Galerkin (MLPG) approach in computational mechanics. *Comput. Mech.* 1998; **22**:117–127. doi: 10.1007/s004660050346

Babuška I, Banerjee U and Osborn JE. Meshless and generalized finite element methods: a survey of some major results. *Lect. Notes Comput. Sci. Eng.* 2003; **26**:1–20.

Babuška I, Banerjee U, Osborn JE and Li Q. Quadrature for meshless methods. *Int. J. Numer. Methods Eng.* 2008; **76**:1434–1470.

Babuška I, Banerjee U, Osborn JE and Zhang Q. Effect of numerical integration on meshless methods. *Comput. Methods Appl. Mech. Eng.* 2009; **198**:2886–2897. doi: 10.1016/j.cma.2009.04.008

Beissel SR and Belytschko T. Nodal integration of the element-free Galerkin method. *Comput. Methods Appl. Mech. Eng.* 1996; **139**:49–74. doi: 10.1016/S0045-7825(96)01079-1

Belytschko T, Guo Y, Liu WK and Xiao SP. A unifieded stability analysis of meshless particle methods. *Int. J. Numer. Methods Eng.* 2000; **48**:1359–1400. doi: 10.1002/1097-0207(20000730)48:9<1359::AID-NME829>3.0.CO;2-U

Belytschko T, Krongauz Y, Organ D, Fleming M and Krysl P. Meshless methods: An overview and recent developments. *Comput. Methods Appl. Mech. Eng.* 1996; **139**:3–47. doi: 10.1016/S0045-7825(96)01078-X

Belytschko T, Lu YY and Gu L. Element-free Galerkin methods. *Int. J. Numer. Methods Eng.* 1994; **37**:229–256. doi: 10.1002/nme.1620370205

Bessa MA, Foster JT, Belytschko T and Liu WK. A meshfree unification: reproducing kernel peridynamics. *Comput. Mech.* 2014; **53**:1251–1264. doi: 10.1007/s00466-013-0969-x

Bonet J and Kulasegaram S. Correction and stabilization of smooth particle hydrodynamics methods with applications in metal forming simulations. *Int. J. Numer. Methods Eng.* 2000; **47**:1189–1214. doi: 10.1002/(SICI)1097-0207(20000228)47:6<1189::AID-NME830>3.0.CO;2-I

Chen JS *Meshfree Methods for Linear and Nonlinear Mechanics*. University of California: San Diego, 2015

Chen JS and Belytschko T. Meshless and meshfree methods. In *Encycl. Appl. Comput. Math*, Engquist B (ed). Springer-Verlag: Berlin, Heidelberg, 2015; 886–894.

Chen J-S, Han W, You Y and Meng X. A reproducing kernel method with nodal interpolation property. *Int. J. Numer. Methods Eng.* 2003; **56**:935–960. doi: 10.1002/nme.592

Chen JS, Hillman M and Rüter M. An arbitrary order variationally consistent integration for Galerkin meshfree methods. *Int. J. Numer. Methods Eng.* 2013; **95**:387–418. doi: 10.1002/nme.4512

Chen J-S, Hu W and Hu H-Y. Reproducing kernel enhanced local radial basis collocation method. *Int. J. Numer. Methods Eng.* 2008; **75**:600–627.

Chen J-S, Hu W, Puso MA, Wu Y and Zhang X. Strain smoothing for stabilization and regularization of galerkin mesh-free methods. *Lect. Notes Comput. Sci. Eng.* 2007; **57**:57–75. doi: 10.1007/978-3-540-46222-4_4

Chen J-S, Pan C, Roque CMOL and Wang H-P. A Lagrangian reproducing kernel particle method for metal forming analysis. *Comput. Mech.* 1998; **22**:289–307. doi: 10.1007/s004660050361

Chen J-S, Pan C and Wu C-T. Large deformation analysis of rubber based on a reproducing kernel particle method. *Comput. Mech.* 1997; **19**:211–227. doi: 10.1007/s004660050170

Chen J-S, Pan C, Wu C-T and Liu WK. Reproducing kernel particle methods for large deformation analysis of non-linear structures. *Comput. Methods Appl. Mech. Eng.* 1996; **139**:195–227. doi: 10.1016/S0045-7825(96)01083-3

Chen J-S and Wang H-P. New boundary condition treatments in meshfree computation of contact problems. *Comput. Methods Appl. Mech. Eng.* 2000; **187**:441–468. doi: 10.1016/S0045-7825(00)80004-3

Chen J-S and Wang D. A constrained reproducing kernel particle formulation for shear deformable shell in Cartesian coordinates. *Int. J. Numer. Methods Eng.* 2006; **68**:151–172. doi: 10.1002/nme.1701

Chen J-S, Wang L, Hu H-Y and Chi S-W. Subdomain radial basis collocation method for heterogeneous media. *Int. J. Numer. Methods Eng.* 2009; **80**:163–190.

Chen J-S, Wang H-P, Yoon S and You Y. Some recent improvements in meshfree methods for incompressible finite elasticity boundary value problems with contact. *Comput. Mech.* 2000; **25**:137–156. doi: 10.1007/s004660050465

Chen J-S, Wu C-T and Yoon S. A stabilized conforming nodal integration for Galerkin mesh-free methods. *Int. J. Numer. Meth. Eng.* 2001; **207**:435–466. doi: 10.1002/1097-0207(20010120)50

Chen J-S, Yoon S and Wu C-T. Non-linear version of stabilized conforming nodal integration for Galerkin mesh-free methods. *Int. J. Numer. Methods Eng.* 2002; **53**:2587–2615. doi: 10.1002/nme.338

Chen J-S, Zhang X and Belytschko T. An implicit gradient model by a reproducing kernel strain regularization in strain localization problems. *Comput. Methods Appl. Mech. Eng.* 2004; **193**:2827–2844. doi: 10.1016/j.cma.2003.12.057

Chi S-W, Chen J-S and Hu H-Y. A weighted collocation on the strong form with mixed radial basis approximations for incompressible linear elasticity. *Comput. Mech.* 2014; **53**:309–324.

Chi S-W, Chen J-S, Hu H-Y and Yang JP. A gradient reproducing kernel collocation method for boundary value problems. *Int. J. Numer. Methods Eng.* 2013; **93**:1381–1402.

Chi S-W, Lee C-H, Chen J-S and Guan P-C. A level set enhanced natural kernel contact algorithm for impact and penetration modeling. *Int. J. Numer. Methods Eng.* 2015; **102**:839–866.

Craiem D and Magin RL. Fractional order models of viscoelasticity as an alternative in the analysis of red blood cell (RBC) membrane mechanics. *Phys. Biol.* 2010; **7**:13001.

Daniel JO and Danielson KT. Recent ERDC developments in computationally modeling concrete under high rate events, ERDC Report, 2010.

Dolbow J and Belytschko T. Numerical integration of the Galerkin weak form in meshfree methods. *Comput. Mech.* 1999; **23**:219–230. doi: 10.1007/s004660050403

Duan Q, Li X, Zhang H and Belytschko T. Second-order accurate derivatives and integration schemes for meshfree methods. *Int. J. Numer. Methods Eng.* 2012; **92**:399–424.

Dyka CT and Ingel RP. An approach for tension instability in smoothed particle hydrodynamics (SPH). *Comput. Struct.* 1995; **57**:573–580. doi: 10.1016/0045-7949(95)00059-P.

Dyka CT, Randles PW and Ingel RP. Stress points for tension instability in SPH. *Int. J. Numer. Methods Eng.* 1997; **40**:2325–2341. doi: 10.1002/(SICI)1097-0207(19970715)40:13<2325::AID-NME161>3.0.CO;2–8

Fernández-Méndez S and Huerta A. Imposing essential boundary conditions in mesh-free methods. *Comput. Methods Appl. Mech. Eng.* 2004; **193**:1257–1275.

Franke C and Schaback R. Solving partial differential equations by collocation using radial basis functions. *Appl. Math. Comput.* 1998; **93**:73–82. doi: 10.1016/S0096-3003(97)10104-7

Fries T-P and Belytschko T. Convergence and stabilization of stress-point integration in mesh-free and particle methods. *Int. J. Numer. Methods Eng.* 2008; **74**:1067–1087.

Gingold RA and Monaghan JJ. Smoothed particle hydrodynamics: theory and application to non-spherical stars. *Mon. Not. R. Astron. Soc.* 1977; **181**:375–389.

Gosz J and Liu WK. Admissible approximations for essential boundary conditions in the reproducing kernel particle method. *Comput. Mech.* 1996; **19**:120–135.

Griebel M and Schweitzer MA. A particle-partition of unity method–part II: efficient cover construction and reliable integration. *SIAM J. Sci. Comput.* 2002; **23**:1655–1682. doi: 10.1137/S1064827501391588

Griebel M and Schweitzer MA. A particle-partition of unity method part V: boundary conditions. *Geom. Anal. Nonlinear Partial* 2003:1–25. doi: 10.1007/978-3-540-46222-4_8

Guan P-C, Chen J-S, Wu Y, Teng H, Gaidos J, Hofstetter K and Alsaleh M. Semi-Lagrangian reproducing kernel formulation and application to modeling earth moving operations. *Mech. Mater.* 2009; **41**:670–683. doi: 10.1016/j.mechmat.2009.01.030

Guan P-C, Chi SW, Chen J-S, Slawson TR and Roth MJ. Semi-Lagrangian reproducing kernel particle method for fragment-impact problems. *Int. J. Impact Eng.* 2011; **38**:1033–1047. doi: 10.1016/j.ijimpeng.2011.08.001

Günther FC and Liu WK. Implementation of boundary conditions for meshless methods. *Comput. Methods Appl. Mech. Eng.* 1998; **163**:205–230. doi: 10.1016/S0045-7825(98)00014-0

Han W and Meng X. Error analysis of the reproducing kernel particle method. *Comput. Methods Appl. Mech. Eng.* 2001; **190**:6157–6181. doi: 10.1016/S0045-7825(01)00214-6

Hardy RL. Multiquadric equations of topography and other irregular surfaces. *J. Geophys. Res.* 1971; **76**:1905. doi: 10.1029/JB076i008p01905

Hardy RL. Theory and applications of the multiquadric-biharmonic method 20 years of discovery 1968–1988. *Comput. Math. Appl.* 1990; **19**:163–208.

Hillman M and Chen J-S. An accelerated, convergent, and stable nodal integration in Galerkin meshfree methods for linear and nonlinear mechanics. *Int. J. Numer. Methods Eng.* 2016; **107**(7):603–630.

Hillman M, Chen J-S and Chi S-W. Stabilized and variationally consistent nodal integration for meshfree modeling of impact problems. *Comput. Part. Mech.* 2014; **1**:245–256. doi: 10.1007/s40571-014-0024-5

Hu H-Y, Chen J-S and Hu W. Weighted radial basis collocation method for boundary value problems. *Int. J. Numer. Methods Eng.* 2007; **69**:2736–2757.

Hu H-Y, Chen J-S and Hu W. Error analysis of collocation method based on reproducing kernel approximation. *Numer. Methods Partial Differ. Equ.* 2011; **27**:554–580.

Hu H-Y, Lai C-K and Chen J-S. A study on convergence and complexity of reproducing kernel collocation method. *Interact. Multiscale Mech.* 2009; **2**:295–319. doi: 10.12989/imm.2009.2.3.295

Hu H-Y and Li Z-C. Collocation methods for Poisson's equation. *Comput. Methods Appl. Mech. Eng.* 2006; **195**:4139–4160. doi: 10.1016/j.cma.2005.07.019

Hughes TJR, Brooks A, *et al.*. A theoretical framework for Petrov–Galerkin methods with discontinuous weighting functions: application to the streamline-upwind procedure. *Finite Elem. Fluids* 1982; **4**:47.

Kaljevic I and Saigal S. An improved element free Galerkin formulation. *Int. J. Numer. Methods Eng.* 1997; **40**:2953–2974. doi: 10.1002/(SICI)1097-0207(19970830)40:16<2953::AID-NME201>3.0.CO;2-S

Kansa EJ. Multiquadrics – a scattered data approximation scheme with applications to computational fluid-dynamics – I surface approximations and partial derivative estimates. *Comput. Math. Appl.* 1990a; **19**:127–145.

Kansa EJ. Multiquadrics – a scattered data approximation scheme with applications to computational fluid-dynamics – II solutions to parabolic, hyperbolic and elliptic partial differential equations. *Comput. Math. Appl.* 1990b; **19**:147–161.

Krongauz Y and Belytschko T. Enforcement of essential boundary conditions in meshless approximations using finite elements. *Comput. Methods Appl. Mech. Eng.* 1996; **131**:133–145. doi: 10.1016/0045-7825(95)00954-X

Krongauz Y and Belytschko T. Consistent pseudo-derivatives in meshless methods. *Comput. Methods Appl. Mech. Eng.* 1997; **146**:371–386. doi: 10.1016/S0045-7825(96)01234-0

Li S and Liu WK. Synchronized reproducing kernel interpolant via multiple wavelet expansion. *Comput. Mech.* 1998; **21**:28–47. doi: 10.1007/s004660050281

Li S and Liu WK. Reproducing kernel hierarchical partition of unity, part I - formulation and theory. *Int. J. Numer. Methods Eng.* 1999a; **288**:251–288. doi: 10.1002/(SICI)1097-0207(19990530)45:3<251::AID-NME583>3.0.CO;2-I

Li S and Liu WK. Reproducing kernel hierarchical partition of unity, Part II – applications. *Int. J. Numer. Methods Eng.* 1999b; **45**:289–317. doi: 10.1002/(SICI)1097-0207(19990530)45:3<251::AID-NME583>3.0.CO;2-I

Lian Y, Ying Y, Tang S, Lin S and Wagner G. A Petrov–Galerkin finite element method for the fractional advection–diffusion equation. *Comput. Methods Appl. Mech. Eng*. 2016; **309**:388–410.

Liu WK and Chen Y. Wavelet and multiple scale reproducing kernel methods. *Int. J. Numer. Methods Fluids* 1995; **2**:901–931.

Liu WK, Chen Y, Chang CT and Belytschko T. Advances in multiple scale kernel particle methods. *Comput. Mech.* 1996a; **18**:73–111. doi: 10.1007/BF00350529

Liu WK, Chen Y, Uras RA and Chang CT. Generalized multiple scale reproducing kernel particle methods. *Comput. Methods Appl. Mech. Eng.* 1996b; **139**:91–157. doi: 10.1016/S0045-7825(96)01081-X

Liu WK, Hao W, Chen Y, Jun S and Gosz J. Multiresolution reproducing kernel particle methods. *Comput. Mech.* 1997a; **20**:295–309.

Liu WK, Jun S, Li S, Adee J and Belytschko T. Reproducing kernel particle methods for structural dynamics. *Int. J. Numer. Methods Eng.* 1995a; **38**:1655–1679.

Liu WK, Jun S, Sihling DT, Chen YJ and Hao W. Multiresolution reproducing kernel particle method for computational fluid dynamics. *Int. J. Numer. Methods Fluids* 1997b; **24**:1391–1415. doi: 10.1002/(SICI)1097-0363(199706)24:12<1391::AID-FLD566>3.0.CO;2–2

Liu WK, Jun S and Zhang YF. Reproducing kernel particle methods. *Int. J. Numer. Methods Fluids* 1995b; **20**:1081–1106. doi: 10.1002/fld.1650200824

Liu WK, Li S and Belytschko T. Moving least-square reproducing kernel methods (I) methodology and convergence. *Comput. Methods Appl. Mech. Eng.* 1997c; **143**:113–154. doi: 10.1016/S0045-7825(96)01132-2

Liu WK and Oberste-Brandenburg C. Reproducing kernel and wavelet particle methods. In *Aerosp. Struct. Nonlinear Dyn. Syst. Response*, AD, vol. **33**, Cusumano JP, Pierre C and Wu JT (eds). ASME: New York, 1993; 39–56.

Liu WK, Ong JS-J and Uras RA. Finite element stabilization matrices-a unification approach. *Comput. Methods Appl. Mech. Eng.* 1985; **53**:13–46.

Liu G-R, Zhang GY, Wang YY, Zhong ZH, Li GY and Han X. A nodal integration technique for meshfree radial point interpolation method (NI-RPIM). *Int. J. Solids Struct.* 2007; **44**:3840–3860. doi: 10.1016/j.ijsolstr.2006.10.025

Loverro A. "Fractional calculus: history, definitions and applications for the engineer." Rapport technique, Univeristy of Notre Dame: Department of Aerospace and Mechanical Engineering (2004.

Lu YY, Belytschko T and Gu L. A new implementation of the element free Galerkin method. *Comput. Methods Appl. Mech. Eng.* 1994; **113**:397–414. doi: 10.1016/0045-7825(94)90056-6

Lu H, Cheng HS, Cao J and Liu WK. Adaptive enrichment meshfree simulation and experiment on buckling and post-buckling analysis in sheet metal forming. *Comput. Methods Appl. Mech. Eng.* 2005; **194**:2569–2590.

Lucy LB. A numerical approach to the testing of the fission hypothesis. *Astron. J.* 1977; **82**:1013–1024.

Madych WR. Miscellaneous error bounds for multiquadric and related interpolators. *Comput. Math. with Appl.* 1992; **24**:121–138. doi: 10.1016/0898-1221(92)90175-H

Monaghan JJ. Why particle methods work. *SIAM J. Sci. Stat. Comput.* 1982; **3**:422–433.

Nagashima T. Node-by-node meshless approach and its applications to structural analyses. *Int. J. Numer. Methods Eng.* 1999; **46**:341–385.

Nitsche J. Über ein Variationsprinzip zur Lösung von Dirichlet-Problemen bei Verwendung von Teilräumen, die keinen Randbedingungen unterworfen sind. *Abhandlungen Aus Dem Math. Semin. Der Univ. Hambg.* 1971; **36**:9–15.

Oñate E, Idelsohn SR, Zienkiewicz OC and Taylor RL. A finite point method in computational mechanics. Applications to convective transport and fluid flow. *Int. J. Numer. Methods Eng.* 1996; **39**:3839–3866. doi: 10.1002/(SICI)1097-0207(19961130)39:22<3839::AID-NME27>3.0.CO;2-R

Podlubny I. *Fractional Differential Equations: An Introduction to Fractional Derivatives, Fractional Differential Equations, to Methods of their Solution and Some of their Applications*. Academic Press: San Diego, 1998

Puso MA, Chen J-S, Zywicz E and Elmer W. Meshfree and finite element nodal integration methods. *Int. J. Numer. Methods Eng.* 2008; **74**:416–446.

Puso MA, Zywicz E and Chen J-S. A new stabilized nodal integration approach. *Lect. Notes Comput. Sci. Eng.* 2007; **57**:207–217. doi: 10.1007/978-3-540-46222-4_12

Rabczuk T, Belytschko T and Xiao SP. Stable particle methods based on Lagrangian kernels. *Comput. Methods Appl. Mech. Eng.* 2004; **193**:1035–1063. doi: 10.1016/j.cma.2003.12.005

Randles PW and Libersky LD. Normalized SPH with stress points. *Int. J. Numer. Meth. Eng.* 2000; **48**:1445–1462. doi: 10.1002/1097-0207(20000810)48:10<1445::AID-NME831>3.0.CO;2–9

Rossikhin YA and Shitikova MV. Application of fractional calculus for dynamic problems of solid mechanics: novel trends and recent results. *Appl. Mech. Rev.* 2010; **63**:10801.

Roth MJ, Chen J-S, Slawson TR and Danielson KT. Stable and flux-conserved meshfree formulation to model shocks. *Comput. Mech.* 2016; **57**:773–792.

Rüter M, Hillman M and Chen J-S. Corrected stabilized non-conforming nodal integration in meshfree methods. *Lect. Notes Comput. Sci. Eng.* 2013; **89**:75–92. doi: 10.1007/978-3-642-32979-1_5

Sherburn JA, Roth MJ, Chen J-S and Hillman M. Meshfree modeling of concrete slab perforation using a reproducing kernel particle impact and penetration formulation. *Int. J. Impact Eng.* 2015; **86**:96–110. doi: 10.1016/j.ijimpeng.2015.07.009

Silling SA. Reformulation of elasticity theory for discontinuities and long-range forces. *J. Mech. Phys. Solids.* 2000; **48**:175–209. doi: 10.1016/S0022-5096(99)00029-0

Silling SA, Epton MA, Weckner O, Xu J and Askari E. Peridynamic states and constitutive modeling. *J. Elast.* 2007; **88**:151–184. doi: 10.1007/s10659-007-9125-1

Sze KY, Chen J-S, Sheng N and Liu XH. Stabilized conforming nodal integration: Exactness and variational justification. *Finite Elem. Anal. Des.* 2004; **41**:147–171. doi: 10.1016/j.finel.2004.05.003

Wagner GJ and Liu WK. Application of essential boundary conditions in mesh-free methods: a corrected collocation method. *Int. J. Numer. Methods Eng.* 2000; **47**:1367–1379. doi: 10.1002/(SICI)1097-0207(20000320)47:8<1367::AID-NME822>3.0.CO;2-Y

Wang D and Chen J-S. Locking-free stabilized conforming nodal integration for meshfree Mindlin-Reissner plate formulation. *Comput. Methods Appl. Mech. Eng.* 2004; **193**:1065–1083. doi: 10.1016/j.cma.2003.12.006

Wang D and Chen J-S. A Hermite reproducing kernel approximation for thin-plate analysis with sub-domain stabilized conforming integration. *Int. J. Numer. Methods Eng.* 2008; **74**:368–390.

Wang L, Chen J-S and Hu H-Y. Subdomain radial basis collocation method for fracture mechanics. *Int. J. Numer. Methods Eng.* 2010; **83**:851–876.

Wang H-P, Wu C-T and Chen J-S. A reproducing kernel smooth contact formulation for metal forming simulations. *Comput. Mech.* 2014; **54**:151–169. doi: 10.1007/s00466-014-1015-3

West BJ. Colloquium: fractional calculus view of complexity: a tutorial. *Rev. Mod. Phys.* 2014; **86**:1169.

Williams EM, Graham SS, Reed PA, *et al.*, Laboratory characterization of Cor-Tuf concrete with and without steel fibers, DTIC Document, 2009.

Wu C-T, Chen J-S, Chi L and Huck F. Lagrangian meshfree formulation for analysis of geotechnical materials. *J. Eng. Mech.* 2001; **127**:440–449.

Wu C-T, Koishi M and Hu W. A displacement smoothing induced strain gradient stabilization for the meshfree Galerkin nodal integration method. *Comput. Mech.* 2015; **56**:19–37. doi: 10.1007/s00466-015-1153-2

Wu Z and Schaback R. Local error estimates for radial basis function interpolation of scattered data. *IMA J. Numer. Anal.* 1993; **13**:13–27.

Yoon J. Spectral approximation orders of radial basis function interpolation on the Sobolev space. *SIAM J. Math. Anal.* 2001; **33**:946–958.

Zhu TL and Atluri SN. A modified collocation method and a penalty formulation for enforcing the essential boundary conditions in the element free Galerkin method. *Comput. Mech.* 1998; **21**:211–222. doi: 10.1007/s004660050296